CATALYTIC WET OXIDATION OF WASTEWATER USING NANOCATALYST

Ph.D. THESIS

by

ANUSHREE

DEPARTMENT OF PAPER TECHNOLOGY
INDIAN INSTITUTE OF TECHNOLOGY ROORKEE
ROORKEE-247 667 (INDIA)
MAY, 2016

CATALYTIC WET OXIDATION OF WASTEWATER USING NANOCATALYST

A THESIS

Submitted in partial fulfilment of the requirements for the award of the degree of

DOCTOR OF PHILOSOPHY

in

CHEMISTRY

by

ANUSHREE

DEPARTMENT OF PAPER TECHNOLOGY
INDIAN INSTITUTE OF TECHNOLOGY ROORKEE
ROORKEE-247 667 (INDIA)
MAY, 2016

INDIAN INSTITUTE OF TECHNOLOGY ROORKEE
ROORKEE

CANDIDATE'S DECLARATION

I hereby certify that the work which is being presented in the thesis entitled **"CATALYTIC WET OXIDATION OF WASTEWATER USING NANOCATALYST"** in partial fulfilment of the requirements and for the award of the Degree of Doctor of Philosophy and submitted in the Department of Paper technology, Indian Institute of Technology Roorkee, Roorkee, is an authentic record of my own work carried out during a period from December, 2010 to May, 2016, under the supervision of Dr. Satish Kumar, Professor and Dr. Chhaya Sharma, Associate Professor, Department of Paper Technology, Indian Institute of Technology Roorkee, Roorkee.

The matter presented in the thesis has not been submitted by me for the award of any other degree of this or any other Institute.

(ANUSHREE)

This is to certify that the above statement made by the candidate is correct to the best of our knowledge.

(Chhaya Sharma)
Supervisor

(Satish Kumar)
Supervisor

Date:

This thesis is dedicated to

MY BELOVED PARENTS

ABSTRACT

Catalytic wet air oxidation (CWAO) using heterogeneous catalyst is a promising advanced oxidation process (AOP) for the treatment of complex industrial wastewaters. The drastic operating conditions during CWAO are disadvantageous as maintaining the process at extreme conditions is not favourable. Catalysis research to develop the economical, active and stable catalyst is a key factor in the development of CWAO at mild operating conditions.

CeO_2 containing materials attracted a lot of interest due to their wide range of applications. Oxygen storage capacity (OSC) of ceria is the most important property which makes it an excellent catalytic material. Despite of its widespread applications, pure CeO_2 has poor thermal stability and it sinters at high temperature, leading to its deactivation. In recent years, a lot of efforts are devoted in designing the CeO_2-based mixed oxide systems, with enhanced thermal stability. The mixed oxides of ceria with transition metals have attracted great attention in various heterogeneous catalytic applications. The redox properties of ceria based mixed oxides are dependent on particle size, lattice defects and chemical nonstoichiometry. The high specific surface area and porosity can be attained by tuning the particle size in nanometer scale.

The aim of this work was to study the activity of Ce-Fe, Ce-Cu, Ce-Co, Ce-Zn and Ce-Ni mixed oxide nanoparticles in CWAO of industrial wastewater. A facile co-precipitation method was adopted for the preparation of mixed oxides. The physicochemical properties of prepared samples were studied by various characterization techniques, i.e, X-ray diffraction (XRD), Fourier transform infrared spectroscopy (FT-IR), X-ray photoelectron spectroscopy (XPS), Raman spectroscopy (RS), N_2-adsorption/desorption, Field emission scanning electron microscopy (FE-SEM), Transmission electron microscopy (TEM) and Energy-dispersive X-ray spectroscopy (EDX).

XRD indicated the successful preparation of nanosized mixed oxides with high lattice defects. FT-IR confirmed the interaction between metal oxides in mixed phases. XPS and Raman studies revealed the oxygen storage capacity of mixed oxides due to high oxygen vacancies and Ce^{3+} content. FE-SEM and TEM micrographs indicated the decrease in particle size with increasing transition metal oxide content. High surface area and porosity of catalysts was assured by N_2-adsorption/desorption analysis. Thus characterization results indicated the suitability of these nanocatalysts for the oxidation application.

The prepared mixed oxides were used in CWAO of paper industry wastewater at atmospheric pressure. The efficiency of catalysts was quantified in terms of Chemical oxygen demand (COD), Total organic carbon (TOC), Biological oxygen demand (BOD), Color, Adsorbable organic halides (AOX) and Chlorophenolics (CHPs) removal. The optimized process variables i.e., initial *pH* of wastewater, catalyst dose, treatment time and treatment temperatures were found to be *pH* 4, 1 gL^{-1}, 2 h and 90°C, respectively. These process variables were optimized for Ce-Fe mixed oxides, and same conditions were utilized for the removal study over other mixed oxides. The catalyst was recovered from the treated wastewater and supernatant was analyzed for the leaching of metal ions.

Fe-Ce mixed oxides were found to be most efficient with 74% COD, 82% color, 72% TOC, 68% AOX and 71% CHPs reduction. Co-Ce and Cu-Ce mixed oxides presented comparable removal efficiency in terms of COD, Color, TOC and AOX removal. In term of CHPs, higher removal was observed over Cu-Ce mixed oxide. Zn-Ce and Ni-Ce mixed oxides, exhibited comparable removal of COD, color and AOX. In terms of TOC and CHPs removal, higher efficiency was attained for Zn-Ce mixed oxides. The removal efficiency of mixed oxides was found to follow the order of Fe-Ce > Co-Ce ≈ Cu-Ce > Zn-Ce > Ni-Ce. The leaching study indicated that the mixed oxides are stable catalysts.

The efficiency of mixed oxides was in good agreement with their structural and textural properties. High removal efficiency of Fe-Ce mixed oxide was related to its high specific surface area, uniform pores and high oxygen storage capacity (Ce^{3+} content). The efficiency of Co-Ce and Cu-Ce mixed oxides was also in accordance with their characterization results. The low efficiency of Zn-Ce mixed oxides may be attributed to the presence of single oxidation state of Zn (i.e., 2+). While others exhibit the multiple oxidation states, like Fe (3+, 2+), Co (3+, 2+), Cu (2+, 1+) which can increase the oxidation property of catalyst.

ACKNOWLEDGEMENT

It is a pleasant aspect to express my deep sense of gratitude to all who have helped me along way through the doctoral studies and memorable stay at I.I.T. Roorkee. There are, of course, few words to properly thank all of them.

My foremost thanks goes to my supervisors **Prof. Satish Kumar** and **Dr. Chhaya Sharma**. I am deeply indebted to them for their mentoring, able guidance, stimulating suggestions, and inspiring thoughts which have been of tremendous help to me throughout my doctoral studies. I cannot forget their kind help and cooperation in bringing me to this position. Their teachings and advice were indispensable for whatever I have been able to do today. I feel highly privileged to have worked under them during the course of this work. I sincerely appreciate their pronounced individualities, humanistic and warm personal approach, which has given me strength to carry out this research work smoothly. I humbly acknowledge a lifetime's gratitude to them.

I am also grateful to my SRC members, Prof. I.D. Mall (external member) and Dr. U.K. Ghosh (internal member) for valuable suggestions at every stage of the work. I also have deep sense of gratitude to Prof. Y. S. Negi (HOD), Dr. A. K. Singh, Dr. Vivek Kumar, Dr. Sujay Chattopadhyay, Dr. S.C. Sharma and Dr. A.K. Jindal for providing me all the necessary facilities required for the accomplishment of this work. **My special thanks to Dr. Paritosh Mohanty** (Department of Chemistry), Dr. Yogesh Kumar Sharma (Department of Physics), Prof. K. D. Verma (HOD, Dept. of Physics, S.V. (PG) College, Aligarh) and Prof. Deo Prakash (S.M.V.D.University) for their continuous inspiration, timely encouragement, and valuable suggestions.

I would like to thank the technical staff of Department of Chemistry, Department of Chemical Engineering, Institute Instrumentation Center, I.I.T. Roorkee, ACMS I.I.T. Kanpur, Mr. Rakesh Kumar, Mr. Krishan Kumar, Mr. Ratnesh Sinha, Mr. Anurag, academic, accounts, and technical staff of the IITR, SRE Campus for their help at the various stages of the research work.

My heartfelt thanks to my dearest seniors Dr. Parveen Kumar, Dr. Ashutosh Kumar Choudhary, Dr. Rajni Sharma, and beloved juniors, Mr. Vivek Kumar Gaurav, Mr. Dushyant Panwar, Miss. Parminder Kaur, Miss. Swati Sood and Miss. Neelam Choudhary, for their ever-

willing help and support in personal and professional front. I would also like to thank my friends and colleagues, Dr. Luxmi Rani, Dr. Anuj Kumar, Dr. Kodandaram Peesapati, Mrs. Pooja Sharma, Mrs. Deepa Oberoi, Mrs. Monika Choudhary, Mrs. Shilpa Kulkarni, Mrs. Prerna Chaturvedi, Mr. Amit Kumar, Mr. Asit Sahoo, Mr. Jai Bhagwan, Mr. Prabhat Vashistha, Mr. Amrish Adhana, Mr. Raeesh Muhammad, Mr. Vivek Sharma, Mr. Sauraj Singh, Mr. Anil Kumar, Mr. Ruchir Priyadarshi, Mr. Sandeep and all the juniors for their encouragement at every moment and keeping me always happy.

Where would I be without my family? My father Mr. Bhopal Singh in the first place, is the person who established what is good in my character, showing me the joy of intellectual pursuit and ethical consideration ever since I was a child. My Mother Mrs. Kusum Rani deserves special mention for her inseparable prayers and support. I also express gratitude to my brothers, Mr. Awaneesh Kumar, Akshit Jatrana, Bhabhi, Mrs. Neeshu Jatrana, for their love, moral support, and encouragement.

Last but not the least, my heartiest thanks goes to my dearest and close friends, Reshu tyagi, Reetu Siwach, Nivedita, Kavita, Manish Malik, Rahul Panwar and Yogendra Kumar for their continuous love, care, encouragement, and moral support.

I also want to express my sincere thanks to all those who directly and indirectly helped me at various stages of the work, but I would not mention their names due to shortage of the space.

The financial support provided by Ministry of Human Resource Development (M.H.R.D.), Govt. of India is gratefully acknowledged.

Finally I am always thankful to the omnipresent, **GOD**, without whose elegance even this world does not exist.

IIT Roorkee

Date: **ANUSHREE**

LIST OF CONTENTS

LIST OF TABLES

LIST OF FIGURES

ABBREVIATIONS

AOPs	Advanced oxidation processes
AOX	Adsorbable organic halides
BE	Binding energy
BET	Brunauer- Emmett-teller
BI	Biodegradability Index
BOD	Biochemical oxygen demand
CC	Chlorocatechols
COD	Chemical oxygen demand
CP	Chlorophenols
CS	Chlorosyringols
CSA	Chlorosyringaldehydes
CV	Chlorovanilin
CWAO	Catalytic wet air oxidation
CWPO	Catalytic wet peroxide oxidation
DCHPs	Di-chlorophenolics
DFT	Density functional theory
DO	Dissolved oxygen
EDX	Energy dispersive x-ray
FE-SEM	Field emission scanning electron microscopy
FTIR	Fourier Transform-Infrared Spectroscopy
FWHM	Full width at half maximum
GC-MS	Gas chromatography-mass spectrometry
IC	Inorganic carbon
ICP-OES	Inductively coupled plasma optical emission spectroscopy

JCPDS	Joint committee on powder diffraction standards
m/z	Mass/charge
MCHPs	Mono- chlorophenolics
NIST	National institute of standards and technology
PCHPs	Penta-chlorophenolics
PSD	Pore size distribution
RS	Raman Spectroscopy
RT	Retention time
TC	Total carbon
TCHPs	Tri-chlorophenolics
TeCHPs	Tetra-chlorophenolics
TEM	Transmission Electron Microscopy
TOC	Total organic carbon
XPS	X-ray photoelectron spectroscopy
XRD	X-ray diffraction

PUBLICATIONS

Research papers (Published/submitted):

1. **Anushree**, Satish Kumar, Chhaya Sharma, Synthesis, characterization and catalytic wet air oxidation property of mesoporous $Ce_{1-x}Fe_xO_2$ mixed oxides, vol-155, page no. 223-231, 2015, *Materials Chemistry and Physics*. (Publisher-**Elsevier**, Impact factor**-2.259**)
2. **Anushree**, Satish Kumar, and Chhaya Sharma, NiO-CeO_2 nano-catalysts: Synthesis, characterization and application in catalytic wet air oxidation of wastewater, vol-5, page no. 419-428, 2015, *Materials Express*. (Publisher-**American Scientific**, Impact factor**-2.299**)
3. **Anushree**, Satish Kumar, and Chhaya Sharma, $Ce_{1-x}Co_xO_y$ nanocatalysts: synthesis, characterization and environmental application, vol-**6**, page no. 2101-2111, 2016, *Catalysis Science and Technology*. (Publisher-**Royal Society of Chemistry**, Impact factor**-5.426**)
4. **Anushree**, Chhaya Sharma and Satish Kumar, Morphology, structure and activity of ZnO-CeO_2 nanoparticles in mild CWAO of wastewater with identification of oxygen vacancies by Raman and XPS study. (Under Revision: **ACS Sustainable Chemistry & Engineering**)
5. **Anushree**, Chhaya Sharma, Satish Kumar, Characterization of Cu-CeO_2 nanocatalysts and their application to wet air oxidation of wastewater under mild conditions. (**Submitted**)

Papers presented in International Conferences:

1. **Anushree**, Chhaya Sharma, Satish Kumar, Catalytic oxidation of wastewater using porous Ceria-Zinc mixed oxide nanocatalyst, International Conference on Functional Materials, 5-7 February, 2014, IIT Kharagpur.
2. **Anushree**, Chhaya Sharma, Satish Kumar, $Ce_{0.4}Ni_{0.6}O_y$ nano-catalyst for removal of chloro-phenolics from wastewater, NanoSciTech 2014, 13-15 February, 2014, Panjab University.
3. **Anushree**, Chhaya Sharma, Satish Kumar, Ceria-Zinc nanocatalyst for removal of chlorophenolis from wastewater, International Conference on Emerging Materials and Applications, 5-6 April, 2014, IIT Roorkee.

Papers to be published through Conferences:

1. **Anushree**, Chhaya Sharma, Satish Kumar, NiO-CeO_2 nano-catalyst for the removal of priority organic pollutants from wastewater through catalytic wet air oxidation, Environmental Systems Science and Engineering, WASET, 2016 New York.

2. **Anushree**, Chhaya Sharma, Satish Kumar, Mn_3O_4-CeO_2 Nano-catalysts: Synthesis, Characterization and Application, 60^{th} DAE Solid State Physics Symposium (DAE-SSPS-2015), Noida, December 21-25, 2015.

Chapter 1

Introduction

1.1. Background and Motivation

Water is the most abundant resource in nature, and is essential to sustain all the livings. The global demand of water has been on a continuous rise and perpetual provision of clean water is a grand challenge of 21st century [1-4]. Huge amount of wastewaters are generated in several industries like, chemical, pharmaceutical, petrochemical, paper industry etc. Rapid pace of industrialization has put water environment on stake, by the discharge of wastewaters [5-7]. The industrial wastewaters are complex and highly variable mixture of numerous compounds [8,9]. The presence of hazardous and toxic pollutants in industrial wastewaters is well reported [10-12]. These pollutants are posing threatening effect to all living beings [13,14]. The increasing environmental concerns and more stringent regulations has awaken the industries to minimize the menacing effects of discharged wastewater [15,16]. This has lead to increased interest in wastewater treatment technologies.

Various methods have been adopted for the industrial wastewater treatment. Conventional treatment techniques applied for the removal of pollutants are physicochemical, thermal and biological methods. Sludge generation is the main drawback associated with the physicochemical techniques such as coagulation, precipitation and flocculation [17-19]. Incineration is very energy consuming and further leads to environmental issues due to emission of hazardous dioxins and furans [20]. Biological treatment is generally the widely employed secondary method for wastewater treatment. But, the presence of non-biodegradable, toxic and hazardous pollutants in wastewater limits its applicability, as they can inhibit the microbial activity [21-24].

Advanced oxidation processes (AOPs) emerged as more promising treatment methods. Various AOPs have been studied, including; ozonation, fenton oxidation and photocatalysis etc. [25-28]. Main drawbacks associated with AOPs is the use of high energy oxidants, like H_2O_2, ozone and/or photons, for the generation of $^{\cdot}OH$ radicals. Ozonation require ozone-off gas treatment and turbidity can absorb UV in photochemical treatments [29]. These limitations forced the researchers to develop an efficient technology able to work with mild oxidant.

1.2. Catalytic wet air oxidation (CWAO)

Catalytic wet air oxidation (CWAO) is an advancement of the wet air oxidation (WAO) process originally developed by Zimmermann [30,31]. CWAO received a considerable interest in the research field of wastewater treatment as it utilizes the mild oxidant, i.e., air or oxygen. It mineralize the organic contaminants present in wastewater into biodegradable intermediates or innocuous compounds like CO_2 and H_2O [32,33]. In CWAO the operating temperature is typically 190°C to 310°C and pressure is 0.5-5.5 MPa [34,35].

Although, CWAO has dominating space, but successful commercialization of this technology at large scale is still a problem due to extreme operating conditions, confronted with the need of special equipment resulting in high operational costs [36-38].

1.3. Heterogeneous catalysts for CWAO

In order to decrease the cost and to increase the rate of reaction, both homogeneous and heterogeneous catalysts have been tried in CWAO of industrial wastewaters. Initial studies on CWAO were mainly centered on homogeneous catalysts, but the need of posterior separation step limited its applicability. Now days, research in the field of CWAO is mainly centered on heterogeneous catalysts, due to their easy separation without secondary pollution [39,40]. Various noble metals, metal oxides and their combinations are being extensively studied as heterogeneous catalysts in CWAO [41-43].

1.3.1. Noble Metals

The noble metals (Pt, Pd, Ru, Rh, and Ir) have been conventionally utilized in CWAO. Noble metal catalysts are found to exhibit the higher activities than base metal catalysts towards the oxidation of organic pollutants [44-47]. Still, the practical application of noble metals is limited as they are quite expensive materials. Therefore, several transition metal oxides are being tested as a cheaper alternative.

1.3.2. Metal Oxides

Metal oxides are the most widely employed class of solid catalysts. Among these, oxides of Cu, Mn, Co, Ni, Fe, Bi and Ce are the most prospective species to compete with the noble metals [48-50]. The metal oxides are inexpensive, but their catalytic activity is relatively low, also the leaching of the active components is the main problem associated with these materials [51-53].

1.4. Reaction mechanism of heterogeneous CWAO

The Langmuir-Hinshelwood-Hougen-Watson (LHHW) adsorption model is the most accepted surface catalysis models for CWAO [54,55]. According to this model the reactants get absorbed on the catalyst surface, where the oxidation reaction takes place and products i.e. intermediates, CO_2 and H_2O gets desorbed by reoxidizing the catalyst's surface.

CWAO takes place through radical mechanism [55,56]. In initiation step, catalyst (denoted by M) forms the free radical by electron transfer as shown in Equation 1.1. During propagation, peroxy radicals ($ROO^{\bullet}$) are generated by the reaction between ($R^{\bullet}$) radical and oxygen (Equation 1.2-1.5). The free-radical reaction continues until free radicals ($R^{\bullet}$) and ($ROO^{\bullet}$) form stable compounds in termination step (Equation (1.6-1.7)).

$$RH + M^{(n+1)+} \rightarrow R^{\bullet} + M^{n+} + H^{+} \quad (1.1)$$

$$R^{\bullet} + O_2 \rightarrow ROO^{\bullet} \quad (1.2)$$

$$ROO^{\bullet} + RH \rightarrow ROOH + R^{\bullet} \quad (1.3)$$

$$ROOH + M^{n+} \rightarrow RO^{\bullet} + M^{(n+1)+} + HO^{-} \quad (1.4)$$

$$ROOH + M^{(n+1)+} \rightarrow ROO^{\bullet} + M^{n+} + H^{+} \quad (1.5)$$

$$R^{\bullet} + R^{\bullet} \rightarrow R - R \quad (1.6)$$

$$R^{\bullet} + ROO^{\bullet} \rightarrow ROOR \quad (1.7)$$

1.5. Literature review of heterogeneous CWAO

Several studies have been reported on CWAO of complex industrial wastewaters and model compounds. This review discusses about the type of wastewater, catalyst, operating conditions and treatment efficiencies from various studies.

1.5.1. CWAO of industrial wastewaters

Zhang et al. [57] investigated the Pd-Pt-Ce/Al_2O_3 catalyst for CWAO of pulp mill wastewater at 170°C and 1.5 MPa, where 99% color and 65% TOC were removed. There was no leaching of Pt and Ce, but Pd (0.14 mg l^{-1}) and Al (41.1 mg l^{-1}) leaching was detected. Pintar et al. [58] studied the CWAO of alkaline and acidic kraft bleaching plant effluents in presence of Ru/TiO_2 and Ru/ZrO_2 at 190°C, 5.5 MPa of air, and achieved 79% and 88% TOC removal, respectively. The rate of TOC decrease was related to the increase in specific surface area of oxides, additionally no leaching of Ru, Ti or Zr was detected. Goi et al. [59] attempted SiO_2-dopped CeO_2 (Si 6 wt.%) in CWAO of halogenated liquid wastes, i.e. pulp and paper bleaching liquor (BL), landfill leachate (LL) and heavily organic halogen polluted industrial wastewater (IW). The results indicated, up to 80% COD and 90% AOX abatement from BL at 187 °C (pressure 2-3.5 MPa). For IW, the COD and AOX removal was 50% at 227°C. For LL, the COD removal was 40%, while there was a slight increase in AOX during reaction at 227°C. Belkacemi et al. [60] studied 1% Pt/Al_2O_3, Cu(II)-exchanged NaY zeolite and Mn/Ce oxides for CWAO of alcohol-distillery wastewater. The catalysts were found to exhibit about 55-75% TOC removal in temperature ranges of 180 to 250^{o}C and pressure ranges from 0.5 to 2.5 MPa. Gomes et al. [61] tried the effectiveness of CWAO for olive oil mill wastewater over carbon supported Pt and Ir (1 wt.% Pt, 5 wt.% Ir) catalysts at 200 °C and 0.69 MPa of O_2. After 8 h treatment time complete TOC and color removal was achieved. Minh et al. [62] tested the Ru and Pt supported on TiO_2 and ZrO_2 in CWAO of different olive oil mill wastewaters at 190 °C and 7 MPa. For Italian effluent (MIB) 96% TOC abatement was obtained with 3%Ru/ZrO_2 catalyst, while 76% conversion was attained with 3%Pt/TiO_2. In CWAO of Tunisian effluent (KD100), low TOC abatement (77%) was obtained with 3%Pt/TiO_2, than 3%Ru/TiO_2 (87%) and 3%Ru/ZrO_2 (90%). Yang et al. [63] reported 96% COD removal efficiency of eggshell like Ru/TiO_2 catalysts during the CWAO of coke-plant wastewater at 250 °C and 4.8 MPa. Han et al. [64] studied the Ce-Cu (1:2) catalyst loaded on carrier γ-Al_2O_3/TiO_2 in CWAO of organic coking wastewater at 180°C and 1.2 MPa. The catalyst exhibited 95% COD removal with

copper ion leaching of 5.81 mg l^{-1}. Chen et al. [65] reported the CWAO of low-biodegradable coking wastewater (raw and NH_3-stripped) in presence of aminated activated carbon (AC) at 1 MPa. The untreated raw coking wastewater presented low biodegradability with BOD/COD of 0.29, while CWAO treatment at 150°C enhanced the ratio to 0.53. After treatment of NH_3-stripped coking wastewater at 160°C, the BOD/COD ratio of 0.78 was achieved. Rodriguez et al. [66] tested 3 wt.% Cu/CNFs (carbon nanofibers) in CWAO of washing textile wastewater at 140°C, 0.87 MPa. The catalyst achieved up to 97% color, 74% TOC and 43% toxicity reduction. Liu et al. [67] reported 96% phenol and 92% COD removal during the CWAO of resin effluent in presence of Ru supported (3 wt.%) on active carbon (AC)-ceramic sphere at 200 °C and 1.5 MPa. Hosseini et al. [68] studied the Ru/Ir oxide coated Ti monolith in CWAO of real pharmaceutical wastewater at 230 °C and 5 MPa. The catalyst achieved >95% COD and TOC removal during treatment.

1.5.2. CWAO of model compounds

Keav et al. [69] reported complete removal of phenol at 160˚C and 2 MPa over Pt/CeO_2 catalyst. Pintar et al. [70] reported 100% removal of phenol during CWAO at 130˚C and 1 MPa in presence of CuO(42 wt.%)-ZnO(47wt.%)-Al_2O_3(10%) catalyst. Hussain et al. [71] achieved the complete destruction of phenolic synthetic wastewater over potassium doped Mn-Ce-O mixed oxide at of 110 ^oC and 0.5 MPa. The catalyst presented very low leaching of Mn (0.6 mgL^{-1}), Ce (<0.1 mgL^{-1}), K (0.5 mgL^{-1}). Stüber et al. [72] reported almost complete removal of phenol during CWAO in the presence of activated carbon at 160˚C and 0.71 MPa. Ovejero et al. [73] investigated the CWAO of phenol over Platinum supported on multiwalled carbon nanotubes (MWCNTs), and reported 94% phenol and 80% TOC conversion at 2 MPa and 200˚C. Yang et al. [74] utilized the CeO_2-TiO_2 (1/1) mixed oxides during CWAO of phenol in batch as well as packed-bed reactor. In batch reactor 100% and 77% removal of COD and TOC was achieved at 150˚C and 3 MPa. In packed-bed reactor 91% COD and 80% TOC removal were achieved at 140˚C and 3.5 MPa. The leaching of Ce and Ti ions was found to be very low, i.e., < 0.2 and 0.04 mgL^{-1}, respectively. Rocha et al. [75] achieved upto 96% oxidation of phenol at 160˚C and 1 MPa over Pt/TiO_2-Ce catalyst. Yang et al. [76] reported complete removal of phenol at 155°C and 2.5 MPa over MWCNTs functionalized by O_3. Morales-Torres et al. [77] tested the Pt/ACs in the CWAO of aniline, and achieved complete removal at 200˚C and 5 MPa. The catalysts exhibited high stability with no Pt leaching. Levi et al. [78] reported the CWAO of aniline solution over nanocasted Mn-Ce-oxide. The mineralization of aniline, TOC and nitrogen at 140°C and 1MPa was 100% 80%

and 90%, respectively. The catalyst was stable even after six runs with <1 mgL^{-1} Ce and 13 mgL^{-1} Mn leaching. Hua et al. [79] investigated the CWAO of azo dye with $CuO/\gamma\text{-}Al_2O_3$ catalyst at 80˚C, and achieved 100%, 80%, 70%, removal of color, COD and TOC. Presence of Ce in catalysts was found to increase the oxygen storage capacity (OSC), and to prevent the deactivation of the catalyst. Yang et al. [80] studied the complete degradation of succinic acid over 0.5 wt% $Ru/Ce_{0.9}Zr_{0.1}O_2$ mixed oxide during CWAO at 190˚C and 5 MPa. There was no Ru or Zr leaching, while Ce leaching was 0.50 mgL^{-1}.

1.6. Catalyst selection criterion

In spite of extensive research in the field of CWAO, still there is the need of a cost-effective, active and stable catalyst for the treatment of industrial wastewater at mild reaction conditions. It is well documented that during CWAO high temperature enhances the reaction rate, while high pressure improves the oxygen solubility in water [81,82]. Therefore, the catalyst with high reactivity and high oxygen buffering can be a good option. Followings are the criteria for selecting a catalyst for CWAO:

(i) High surface area: Surface area of catalyst has a vital effect on the reaction rate. High surface area can be attained by decreasing the particles size up to nanometer scale.

(ii) Porosity: Presence of porous channels provides high access to active sites.

(iii) Oxygen storage capacity (OSC): Presence of oxygen vacancies has a decisive role as they increase the availability of oxygen during oxidation reaction.

(iv) Thermal stability: Stability of material is an important parameter which limits the leaching of active species during high temperature operation.

(v) Low cost: The catalyst material must be of low cost for the industrial application.

(vi) Facile catalyst preparation: The catalyst preparation procedure should not be much complicated, time-consuming and expensive.

Recently, Lafaye et al. [83] reported that nano-CeO_2 with high surface area is an excellent support, due to its high oxygen storage capacity (OSC). Therefore, CeO_2 based nanomaterials can be thought as a suitable candidate for the above addressed problem.

1.7. Cerium dioxide: structure and properties

Cerium is most abundant among the rare earth elements or lanthanides. Around 50% of the rare earth raw material contains cerium in its oxide form. Cerium dioxide (CeO_2, ceria) is the most stable oxide of cerium. It is most widely explored rare earth oxide [83,84], with important applications in the field of ceramics [85], gas sensors [86], fuel cell [87], solid state electrolyte [88], solar cell [89] and catalysis [90,91] etc. It crystallizes in the face-centered cubic (fcc) type structure where each cerium cation is bonded to eight oxygen anions and each oxygen atom is tetrahedrally coordinated by four cations [92]. The crystal structure of CeO_2 is graphically presented in **Figure 1.1**.

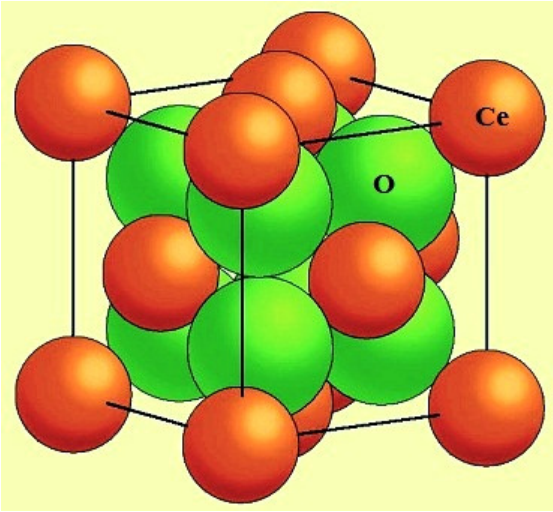

Fig.1.1. Crystal structure of CeO_2

CeO_2 gained much attention due to its unique ability of shifting between two ionic states i.e., ceric ion (Ce^{4+}) to cerous ion (Ce^{3+}) or vice versa. This reversible transformation leads to the formation of non-stoichiometric oxide, i.e. CeO_{2-x}. The oxygen storage capacity (OSC) of ceria depends on the reversible addition and removal of oxygen due to interchange of oxidation states (equation 1.8). Thus, it can respond to lack or excess of oxygen, either by loss/gain of oxygen to/from the surrounding [93-95].

$$-Ce^{4+} - O^{2-} - Ce^{4+} - \rightarrow -Ce^{3+} - \square - Ce^{3+} - + \tfrac{1}{2}O_2 \qquad (1.8)$$

The presence of oxygen vacancies is the intrinsic property for its potential applications. The density of oxygen vacancies is directly related to the Ce^{3+} fraction, which is quantified by the

$Ce^{3+}/(Ce^{3+}+Ce^{4+})$ ratio [96-98]. The defects in ceria are dynamic and may change spontaneously or due to some physical parameters like, temperature, electrical field, surface stresses and doping with other ions [99-102]. Ceria-based materials have been widely studied in environmental oxidation applications where the oxygen defects were found to promote the production of active radicals [103,104].

1.7.1. Mixed metal oxides of CeO_2

Although CeO_2 has widespread applications but, it suffers from the drawback of sintering at high temperature [105-106]. Therefore, much focus is given in developing its mixed metal oxides (MMOs). MMOs are the combination of two or more metallic oxides with more active sites, recyclability, high surface area and high thermal stability than the component oxides [107-109]. MMOs are the largest family of heterogeneous catalysts for industrial applications [110-113]. The MMOs of ceria can be prepared either by doping [114,115] or mixing [116-118] with other metal oxides. Among metal oxides, the transition metals have dominating space due to their low cost, abundance and easy regeneration. Over the past several years, ceria-transition metal MMOs have attracted researchers in the field of environmental catalysis. The Fenton degradation of phenolic wastewaters for toxicity removal and biodegradability enhancement was studied over Fe-Ce solid catalysts [119]. Fe^{III} supported on ceria was an effective catalyst in heterogeneous photo-oxidation of basic orange 2 [120]. The Mn-Co-Ce mixed oxides were selective catalysts during CO preferential oxidation reaction [121].

Ceria-transition metal MMOs are reported to exhibit high O_2-buffering capacity, which is attributed to the extended redox property of ceria-transition metal in comparison to pure CeO_2. The redox property of transition metal oxide plays a crucial role in increasing the O_2-buffering of MMOs and enables it to act as an oxygen reservoir. From the fundamental point of view, presence of more than one metal element in a common structure permits better alteration of local electronic properties [122-123]. The catalytic activity of CeO_2 based MMOs can also be enhanced markedly by decreasing the particle size, thereby increasing the coordinatively unsaturated Ce active sites [124].

1.8. Nanomaterials in wastewater treatment

The rapid growth of nanotechnology offer great opportunity to develop the next-generation catalyst for wastewater treatment [125-126]. The capability behind nanotechnology was first envisioned as a talk entitled "There's Plenty of Room at the Bottom" by physicist Richard Feynman at an American Physical Society meeting [127]. Nanomaterials have gained enormous interest as an alternative to the conventional materials [128-130]. They are excellent catalysts due to their high reactivity, specific surface areas and pore networks [131-134]. Their mobility in solution is remarkably high, which makes the scanning of whole volume possible in a very short time [135].

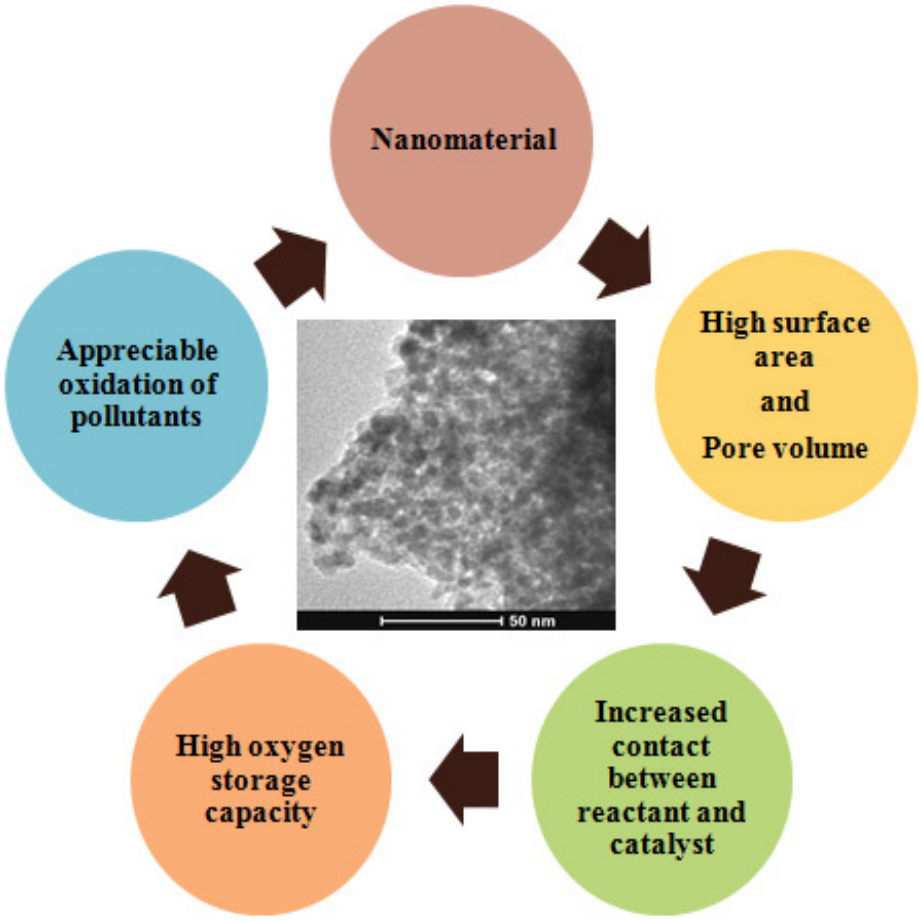

Fig.1.2. Role of Nanocatalyst in oxidation

Porous structure is an important feature of nanomaterials. The pores may exist between crystallites or between agglomerates. IUPAC has defined three types of pores, **Micropores** (with pore diameters < 2 nm), **Mesopores** (pore diameters 2 to 50 nm) and **Macropores** (pore diameters >50 nm). Out of these, mesopores of 5-20 nm are most significant as they can allow an even diffusion of reactants and products. The nanomaterials have been successfully applied in the fields of biochemical sensors [136], spintronics [137], catalysis [138-139] and energy [140], etc. A few nanomaterials have also been studied in CWAO of some model compounds at mild conditions [141,142]. The role of CeO_2 based nanomaterials in oxidation is graphically presented in **Figure 1.2**.

1.9. Problem statement

CWAO is a promising technique for industrial wastewater treatment. The drastic operating conditions during CWAO are disadvantageous as maintaining the process at extreme conditions is not favorable. Also the segregation of active species can take place during high temperature treatment. The catalyst able to exhibit good activity at mild conditions can be a good solution to this problem.

Ceria is widely studied rare earth metal for numerous applications. Oxygen storage capacity (OSC) of ceria is the key property which makes it an excellent catalytic material. The oxidation property of ceria is dependent on oxygen vacancies. One way to induce the oxygen vacancies is the formation of mixed oxide with lower valent elements. In the present study, the transition metal oxides i.e., Iron (Fe), Copper (Cu), Cobalt (Co), Zinc (Zn) and Nickel (Ni) were utilized for the formation of ceria-transition metal mixed oxides. CeO_2-based mixed oxide systems are reported to have high thermal stability. Additionally the tuning of particle size in nanometer scale results in increased specific surface area and porosity, providing a larger number of active sites.

The present work aims to evaluate the performance of Ce-Fe, Ce-Co, Ce-Cu, Ce-Zn, Ce-Ni mixed oxide nanoparticles for the removal of recalcitrant organic compounds in industrial wastewater through CWAO.

1.10. Objectives of the study

In view of the above, following objectives were formulated:

1. The primary objective was to prepare the nanosized ceria-transition metal mixed oxide, namely; Ce-Fe, Ce-Co, Ce-Cu, Ce-Zn, Ce-Ni, by co-precipitation method.

2. The intensive physicochemical characterization of the structural, microstructural and textural properties of catalysts by various spectroscopic and non-spectroscopic techniques, i.e., X-ray diffraction (XRD), N_2-adsorption-desorption, Fourier Transform Infrared Spectroscopy (FT-IR), Raman spectroscopy (RS), X-ray photoelectron spectroscopy (XPS), Scanning electron microscopy (FE-SEM), Transmission electron microscopy (TEM) and Energy dispersive X-ray spectrometer (EDX).

3. To study the activity of catalysts towards CWAO of wastewater, in terms of chemical oxygen demand (COD), biochemical oxygen demand (BOD), color, total organic carbon (TOC), biodegradability index (BI = BOD/COD), adsorbable organic halides (AOX) and chlorophenolics (CHPs).

4. To study the metal leaching and reusability of catalysts.

THESIS OUTLINE

On the basis of work being done, this thesis has been organized into nine chapters. A brief description of the work is presented as follows:

Chapter 1 throws light on the literature of heterogeneous catalysts for catalytic wet air oxidation (CWAO). The significance of cerium oxide is discussed with special emphasis on nanosized mixed metal oxides. This chapter gives an overview of the objectives of the research work presented in this thesis.

Chapter 2 presents the experimental procedures adopted for the synthesis and application of catalysts. It also deals with the background of various environmental parameters of wastewater. A detailed discussion of the techniques used for characterization of catalysts is also included.

Chapter 3 covers the results and discussion on the structural and textural characteristics of $Ce_{1-x}Fe_xO_2$ mixed oxides. The activity of $Ce_{1-x}Fe_xO_2$ catalysts in CWAO of wastewater along with the optimization of operating variables is discussed.

Chapter 4 describes the characterization results of $Ce_{1-x}Co_xO_y$ mixed oxides by various techniques. The chapter also presents the activity studies of $Ce_{1-x}Co_xO_y$ nanocatalysts in CWAO of wastewater.

Chapter 5 enlightens the characterization results of CuO-CeO_2 nanoparticles, followed by their application in the oxidation of organic pollutants present in wastewater by CWAO.

Chapter 6 presents the results and discussion on the structural and textural characteristics of NiO-CeO_2 catalysts. The application NiO-CeO_2 nanocatalyst for CWAO of wastewater is also explored.

Chapter 7 is focused on the discussion of characterization results of ZnO-CeO_2 nanoparticles, followed by their activity studies in CWAO of wastewater.

Chapter 8 compares the characteristics and activity of catalysts (Ce-Fe, Ce-Co, Ce-Cu, Ce-Zn, Ce-Ni), also a correlation between property and activity of catalysts is discussed.

Chapter 9 concludes this thesis with the main conclusions. Some recommendations and future work are also discussed, based on the conclusions drawn from the work presented.

REFERENCES

[1] Schwegler, E., Galli, G. and Gygi, F., 2000. Water under pressure. *Physical Review Letters*, *84*(11), p.2429.

[2] Warrick, L.F., 1953. Improving the Quality of Water Resources. *Industrial & Engineering Chemistry*, *45*(12), pp.2669-2672.

[3] Kundzewicz, Z.W. and Doell, P., 2009. Will groundwater ease freshwater stress under climate change?. *Hydrological Sciences Journal*, *54*(4), pp.665-675.

[4] Fetter, C.W., 2000. *Applied hydrogeology*. Prentice hall.

[5] Lamers, L.P., Tomassen, H.B. and Roelofs, J.G., 1998. Sulfate-induced eutrophication and phytotoxicity in freshwater wetlands. *Environmental Science & Technology*, *32*(2), pp.199-205.

[6] Wang, L.K., Hung, Y.T., Lo, H.H. and Yapijakis, C. eds., 2005. *Waste treatment in the process industries*. CRC Press.

[7] Chakraborty, S., Purkait, M.K., DasGupta, S., De, S. and Basu, J.K., 2003. Nanofiltration of textile plant effluent for color removal and reduction in COD.*Separation and purification Technology*, *31*(2), pp.141-151.

[8] Ríos, A., de Castro, M.D.L. and Valcárcel, M., 1984. New approach to the simultaneous determination of pollutants in waste waters by flow injection analysis. Part A. Anionic pollutants. *Analyst*, *109*(11), pp.1487-1492.

[9] Mwenesongole, E.M., Gautam, L., Hall, S.W., Waterhouse, J.W. and Cole, M.D., 2013. Simultaneous detection of controlled substances in waste water.*Analytical Methods*, *5*(13), pp.3248-3254.

[10] Stüber, F., Font, J., Eftaxias, A., Paradowska, M., Suarez, M.E., Fortuny, A., Bengoa, C. and Fabregat, A., 2005. Chemical wet oxidation for the abatement of refractory non-biodegradable organic wastewater pollutants.*Process Safety and Environmental Protection*, *83*(4), pp.371-380.

[11] Lee, I.S., Sim, W.J., Kim, C.W., Chang, Y.S. and Oh, J.E., 2011. Characteristic occurrence patterns of micropollutants and their removal efficiencies in industrial wastewater treatment plants. *Journal of Environmental Monitoring*, *13*(2), pp.391-397.

[12] Barrera-Díaz, C., Linares-Hernández, I., Roa-Morales, G., Bilyeu, B. and Balderas-Hernández, P., 2008. Removal of biorefractory compounds in industrial wastewater by chemical and electrochemical pretreatments.*Industrial & Engineering Chemistry Research*, *48*(3), pp.1253-1258.

[13] Dietrich, A.M., 2006. Aesthetic issues for drinking water. *Journal of water and health*, *4*(S1), pp.11-16.

[14] Armitage, J.M., Quinn, C.L. and Wania, F., 2011. Global climate change and contaminants-an overview of opportunities and priorities for modelling the potential implications for long-term human exposure to organic compounds in the Arctic. *Journal of Environmental Monitoring*, *13*(6), pp.1532-1546.

[15] Richardson, S.D. and Ternes, T.A., 2005. Water analysis: emerging contaminants and current issues. *Analytical Chemistry*, *77*(12), pp.3807-3838.

[16] Köhler, A., Hellweg, S., Escher, B.I. and Hungerbühler, K., 2006. Organic pollutant removal versus toxicity reduction in industrial wastewater treatment: The example of wastewater from fluorescent whitening agent production. *Environmental science & technology*, *40*(10), pp.3395-3401.

[17] Nemerow, N.L. and Dasgupta, A., 1991. Industrial and hazardous waste treatment.

[18] Yadav, A., Mukherji, S. and Garg, A., 2013. Removal of chemical oxygen demand and color from simulated textile wastewater using a combination of chemical/physicochemical processes. *Industrial & Engineering Chemistry Research*, *52*(30), pp.10063-10071.

[19] Ramdani, N., Hamou, A., Lousdad, A. and Al-Douri, Y., 2015. Physicochemical characterization of sewage sludge and green waste for agricultural utilization. *Environmental technology*, *36*(12), pp.1594-1604.

[20] Brna, T.G. and Kilgroe, J.D., 1990. Control of PCDD/PCDF emissions from municipal waste combustion systems. *Chemosphere*, *20*(10-12), pp.1875-1882.

[21] Willmott, N., Guthrie, J. and Nelson, G., 1998. The biotechnology approach to colour removal from textile effluent. *Journal of the Society of Dyers and Colourists*, *114*(2), pp.38-41.

[22] Rana, R.S., Singh, P., Kandari, V., Singh, R., Dobhal, R. and Gupta, S., 2014. A review on characterization and bioremediation of pharmaceutical industries' wastewater: an Indian perspective. *Applied Water Science*, pp.1-12.

[23] Clark, T. and Stephenson, T., 1998. Effects of chemical addition on aerobic biological treatment of municipal wastewater. *Environmental technology*,*19*(6), pp.579-590.

[24] Bajpai, P. and Bajpai, P.K., 1994. Biological colour removal of pulp and paper mill wastewaters. *Journal of Biotechnology*, *33*(3), pp.211-220.

[25] Ramachandran, G. and Kumarasamy, T., 2013. Degradation of Textile Dyeing Wastewater by a Modified Solar Photo-Fenton Process Using Steel Scrap/H_2O_2. *CLEAN–Soil, Air, Water*, *41*(3), pp.267-274.

[26] Cano Quiroz, A., Barrera-Díaz, C., Roa-Morales, G., Balderas Hernández, P., Romero, R. and Natividad, R., 2010. Wastewater ozonation catalyzed by iron. *Industrial & Engineering Chemistry Research*, *50*(5), pp.2488-2494.

[27] Canizares, P., Paz, R., Sáez, C. and Rodrigo, M.A., 2009. Costs of the electrochemical oxidation of wastewaters: a comparison with ozonation and Fenton oxidation processes. *Journal of Environmental Management*, *90*(1), pp.410-420.

[28] Laera, G., Cassano, D., Lopez, A., Pinto, A., Pollice, A., Ricco, G. and Mascolo, G., 2011. Removal of organics and degradation products from industrial wastewater by a membrane bioreactor integrated with ozone or UV/H_2O_2 treatment. *Environmental science & technology*, *46*(2), pp.1010-1018.

[29] Sharma, S.K., Bhunia, H. and Bajpai, P.K., 2012. Photocatalytic decolorization kinetics and adsorption isotherms of a mixture of two anionic azo dyes: Reactive Red 120 and Reactive Black 5. *Desalination and Water Treatment*, *44*(1-3), pp.261-268.

[30] Zimmermann, F.J. and Diddams, D.G., 1960. The Zimmermann process and its application in the pulp and paper industry. *Tappi*, *43*(8), pp.710-715.

[31] Luck, F., 1996. A review of industrial catalytic wet air oxidation processes.*Catalysis Today*, *27*(1), pp.195-202.

[32] Levec, J. and Pintar, A., 2007. Catalytic wet-air oxidation processes: a review. *Catalysis Today*, *124*(3), pp.172-184.

[33] Pirkanniemi, K. and Sillanpää, M., 2002. Heterogeneous water phase catalysis as an environmental application: a review. *Chemosphere*, *48*(10), pp.1047-1060.

[34] Shibaeva, L.V., 1969. Oxidation of Phenol with Molecular Oxygen in Aqueous Solutions I. The Kinetics of the Oxidation of Phenol with Oxygen.*Kinet. Catal.*, *10*, pp.832-836.

[35] Gomes, H.T., Figueiredo, J.L. and Faria, J.L., 2000. Catalytic wet air oxidation of low molecular weight carboxylic acids using a carbon supported platinum catalyst. *Applied Catalysis B: Environmental*, *27*(4), pp.L217-L223.

[36] Luck, F., 1999. Wet air oxidation: past, present and future. *Catalysis today*,*53*(1), pp.81-91.

[37] Álvarez, P.M., McLurgh, D. and Plucinski, P., 2002. Copper oxide mounted on activated carbon as catalyst for wet air oxidation of aqueous phenol. 2. Catalyst stability. *Industrial & engineering chemistry research*, *41*(9), pp.2153-2158.

[38] Levec, J., 1997. Wet oxidation processes for treating industrial wastewaters.*Chemical and biochemical engineering quarterly*, *11*(1), pp.47-58.

[39] Herrmann, J.M., 1999. Heterogeneous photocatalysis: fundamentals and applications to the removal of various types of aqueous pollutants. *Catalysis today*, *53*(1), pp.115-129.

[40] Sharma, Y.C., Singh, B. and Korstad, J., 2011. Latest developments on application of heterogenous basic catalysts for an efficient and eco friendly synthesis of biodiesel: a review. *Fuel*, *90*(4), pp.1309-1324.

[41] Matatov-Meytal, Y.I. and Sheintuch, M., 1998. Catalytic abatement of water pollutants. *Industrial & engineering chemistry research*, *37*(2), pp.309-326.

[42] Imamura, S., Nakamura, M., Kawabata, N., Yoshida, J. and Ishida, S., 1986. Wet oxidation of poly (ethylene glycol) catalyzed by manganese-cerium composite oxide. *Industrial & engineering chemistry product research and development*, *25*(1), pp.34-37.

[43] Kovenklioglu, S., Cao, Z., Shah, D., Farrauto, R.J. and Balko, E.N., 1992. Direct catalytic hydrodechlorination of toxic organics in wastewater. *AIChE journal*, *38*(7), pp.1003-1012.

[44] Cao, S., Chen, G., Hu, X. and Yue, P.L., 2003. Catalytic wet air oxidation of wastewater containing ammonia and phenol over activated carbon supported Pt catalysts. *Catalysis Today*, *88*(1), pp.37-47.

[45] Masende, Z.P.G., Kuster, B.F.M., Ptasinski, K.J., Janssen, F.J.J.G., Katima, J.H.Y. and Schouten, J.C., 2003. Platinum catalysed wet oxidation of phenol in a stirred slurry reactor: the role of oxygen and phenol loads on reaction pathways. *Catalysis today*, *79*, pp.357-370.

[46] Oliviero, L., Barbier, J., Duprez, D., Guerrero-Ruiz, A., Bachiller-Baeza, B. and Rodrıguez-Ramos, I., 2000. Catalytic wet air oxidation of phenol and acrylic acid over Ru/C and Ru–CeO_2/C catalysts. *Applied Catalysis B: Environmental*, *25*(4), pp.267-275.

[47] Garcia-Vidal, F.J., Martin-Moreno, L. and Pendry, J.B., 2005. Surfaces with holes in them: new plasmonic metamaterials. *Journal of optics A: Pure and applied optics*, *7*(2), p.S97.

[48] Dapeng, L.I. and Jiuhui, Q.U., 2009. The progress of catalytic technologies in water purification: A review. *Journal of Environmental Sciences*, *21*(6), pp.713-719.

[49] Kašpar, J., Fornasiero, P. and Graziani, M., 1999. Use of CeO_2-based oxides in the three-way catalysis. *Catalysis Today*, *50*(2), pp.285-298.

[50] Legube, B. and Leitner, N.K.V., 1999. Catalytic ozonation: a promising advanced oxidation technology for water treatment. *Catalysis Today*, *53*(1), pp.61-72.

[51] Hung, C.M., 2009. Activity of Cu-activated carbon fiber catalyst in wet oxidation of ammonia solution. *Journal of hazardous materials*, *166*(2), pp.1314-1320.

[52] Kim, K.H., Kim, J.R. and Ihm, S.K., 2009. Wet oxidation of phenol over transition metal oxide catalysts supported on $Ce_{0.65}Zr_{0.35}O_2$ prepared by continuous hydrothermal synthesis in supercritical water. *Journal of hazardous materials*, *167*(1), pp.1158-1162.

[53] Hočevar, S., Krašovec, U.O., Orel, B., Arico, A.S. and Kim, H., 2000. CWO of phenol on two differently prepared CuO–CeO_2 catalysts. *Applied Catalysis B: Environmental*, *28*(2), pp.113-125.

[54] Bhargava, S.K., Tardio, J., Prasad, J., Föger, K., Akolekar, D.B. and Grocott, S.C., 2006. Wet oxidation and catalytic wet oxidation. *Industrial & engineering chemistry research*, *45*(4), pp.1221-1258.

[55] Arena, F., Italiano, C., Raneri, A. and Saja, C., 2010. Mechanistic and kinetic insights into the wet air oxidation of phenol with oxygen (CWAO) by homogeneous and heterogeneous transition-metal catalysts. *Applied Catalysis B: Environmental*, *99*(1), pp.321-328.

[56] Debellefontaine, H., Chakchouk, M., Foussard, J.N., Tissot, D. and Striolo, P., 1996. Treatment of organic aqueous wastes: wet air oxidation and wet peroxide oxidation®. *Environmental pollution*, *92*(2), pp.155-164.

[57] Zhang, Q. and Chuang, K.T., 1999. Treatment of combined bleach plant effluents via wet oxidation over a Pd-Pt-Ce/alumina catalyst. *Environmental science & technology*, *33*(20), pp.3641-3644.

[58] Pintar, A., Besson, M. and Gallezot, P., 2001. Catalytic wet air oxidation of Kraft bleaching plant effluents in the presence of titania and zirconia supported ruthenium. *Applied Catalysis B: Environmental*, *30*(1), pp.123-139.

[59] Goi, D., De Leitenburg, C., Dolcetti, G. and Trovarelli, A., 2006. COD and AOX abatement in catalytic wet oxidation of halogenated liquid wastes using CeO_2 based catalysts. *Journal of alloys and compounds*, *408*, pp.1136-1140.

[60] Belkacemi, K., Larachi, F., Hamoudi, S. and Sayari, A., 2000. Catalytic wet oxidation of high-strength alcohol-distillery liquors. *Applied Catalysis A: General*, *199*(2), pp.199-209.

[61] Gomes, H.T., Figueiredo, J.L. and Faria, J.L., 2007. Catalytic wet air oxidation of olive mill wastewater. *Catalysis Today*, *124*(3), pp.254-259.

[62] Minh, D.P., Gallezot, P., Azabou, S., Sayadi, S. and Besson, M., 2008. Catalytic wet air oxidation of olive oil mill effluents: 4. Treatment and detoxification of real effluents. *Applied Catalysis B: Environmental*, *84*(3), pp.749-757.

[63] Yang, M., Sun, Y., Xu, A.H., Lu, X.Y., Du, H.Z., Sun, C.L. and Li, C., 2007. Catalytic wet air oxidation of coke-plant wastewater on ruthenium-based eggshell catalysts in a bubbling bed reactor. *Bulletin of environmental contamination and toxicology*, *79*(1), pp.66-70.

[64] Han, L., Zhu, J., Kang, J., Liang, Y. and Sun, Y., 2009. Catalytic wet air oxidation of high-strength organic coking wastewater. *Asia-Pacific Journal of Chemical Engineering*, *4*(5), pp.624-627.

[65] Chen, H., Yang, G., Feng, Y., Shi, C., Xu, S., Cao, W. and Zhang, X., 2012. Biodegradability enhancement of coking wastewater by catalytic wet air oxidation using aminated activated carbon as catalyst. *Chemical engineering journal*, *198*, pp.45-51.

[66] Rodríguez, A., Ovejero, G., Romero, M.D., Díaz, C., Barreiro, M. and García, J., 2008. Catalytic wet air oxidation of textile industrial wastewater using metal supported on carbon nanofibers. *The Journal of Supercritical Fluids*, *46*(2), pp.163-172.

[67] Liu, W.M., Hu, Y.Q. and Tu, S.T., 2010. Active carbon–ceramic sphere as support of ruthenium catalysts for catalytic wet air oxidation (CWAO) of resin effluent. *Journal of hazardous materials*, *179*(1), pp.545-551.

[68] Hosseini, A.M., Tungler, A., Schay, Z., Szabó, S., Kristóf, J., Széles, É. and Szentmiklósi, L., 2012. Comparison of precious metal oxide/titanium monolith catalysts in wet oxidation of wastewaters. *Applied Catalysis B: Environmental*, *127*, pp.99-104.

[69] Keav, S., Martin, A., Barbier, J. and Duprez, D., 2010. Deactivation and reactivation of noble metal catalysts tested in the Catalytic Wet Air Oxidation of phenol. *Catalysis Today*, *151*(1), pp.143-147.

[70] Pintar, A. and Levec, J., 1992. Catalytic oxidation of organics in aqueous solutions: I. Kinetics of phenol oxidation. *Journal of catalysis*, *135*(2), pp.345-357.

[71] Hussain, S.T., Sayari, A. and Larachi, F., 2001. Novel K-doped Mn-Ce-O wet oxidation catalysts with enhanced stability. *Journal of Catalysis*, *201*(1), pp.153-157.

[72] Stüber, F., Polaert, I., Delmas, H., Font, J., Fortuny, A. and Fabregat, A., 2001. Catalytic wet air oxidation of phenol using active carbon: performance of discontinuous and continuous reactors. *Journal of Chemical Technology and Biotechnology*, *76*(7), pp.743-751.

[73] Ovejero, G., Sotelo, J.L., Rodriguez, A., Diaz, C., Sanz, R. and Garcia, J., 2007. Platinum catalyst on multiwalled carbon nanotubes for the catalytic wet air oxidation of phenol. *Industrial & Engineering Chemistry Research*,*46*(20), pp.6449-6455.

[74] Yang, S., Zhu, W., Wang, J. and Chen, Z., 2008. Catalytic wet air oxidation of phenol over CeO_2-TiO_2 catalyst in the batch reactor and the packed-bed reactor. *Journal of hazardous materials*, *153*(3), pp.1248-1253.

[75] Rocha, M.L., Del Ángel, G., Torres-Torres, G., Cervantes, A., Vázquez, A., Arrieta, A. and Beltramini, J.N., 2015. Effect of the Pt oxidation state and Ce^{3+}/Ce^{4+} ratio on the Pt/TiO_2-CeO_2 catalysts in the phenol degradation by catalytic wet air oxidation (CWAO). *Catalysis Today*, *250*, pp.145-154.

[76] Yang, S., Sun, Y., Yang, H. and Wan, J., 2015. Catalytic wet air oxidation of phenol, nitrobenzene and aniline over the multi-walled carbon nanotubes (MWCNTs) as catalysts. *Frontiers of Environmental Science & Engineering*,*9*(3), pp.436-443.

[77] Morales-Torres, S., Silva, A.M., Maldonado-Hódar, F.J., Machado, B.F., Pérez-Cadenas, A.F., Faria, J.L., Figueiredo, J.L. and Carrasco-Marín, F., 2011. Pt-catalysts supported on activated carbons for catalytic wet air oxidation of aniline: activity and stability. *Applied Catalysis B: Environmental*, *105*(1), pp.86-94.

[78] Levi, R., Milman, M., Landau, M.V., Brenner, A. and Herskowitz, M., 2008. Catalytic wet air oxidation of aniline with nanocasted Mn-Ce-oxide catalyst.*Environmental science & technology*, *42*(14), pp.5165-5170.

[79] Hua, L., Ma, H. and Zhang, L., 2013. Degradation process analysis of the azo dyes by catalytic wet air oxidation with catalyst CuO/γ-Al_2O_3.*Chemosphere*, *90*(2), pp.143-149.

[80] Yang, S., Besson, M. and Descorme, C., 2015. Catalytic wet air oxidation of succinic acid over Ru and Pt catalysts supported on $Ce_xZr_{1-x}O_2$ mixed oxides. *Applied Catalysis B: Environmental*, *165*, pp.1-9.

[81] Fortuny, A., Bengoa, C., Font, J., Castells, F. and Fabregat, A., 1999. Water pollution abatement by catalytic wet air oxidation in a trickle bed reactor.*Catalysis Today*, *53*(1), pp.107-114.

[82] Lei, L., Hu, X. and Yue, P.L., 1998. Improved wet oxidation for the treatment of dyeing wastewater concentrate from membrane separation process. *Water research*, *32*(9), pp.2753-2759.

[83] Lafaye, G., Barbier, J. and Duprez, D., 2015. Impact of cerium-based support oxides in catalytic wet air oxidation: Conflicting role of redox and acid–base properties. *Catalysis Today*, *253*, pp.89-98.

[84] Hamedani, N.F., Mahjoub, A.R. and Mortazavi, Y., 2012. CeO_2 doped ZnO flower-like nanostructure sensor selective to ethanol in presence of CO and CH_4. *Sensors and Actuators B: Chemical*, *169*, pp.67-73.

[85] Singh, K., Acharya, S.A. and Bhoga, S.S., 2006. Nanosized ceria-based ceramics: a comparative study. *Ionics*, *12*(4-5), pp.295-301.

[86] Jasinski, P., Suzuki, T. and Anderson, H.U., 2003. Nanocrystalline undoped ceria oxygen sensor. *Sensors and Actuators B: Chemical*, *95*(1), pp.73-77.

[87] Steele, B.C. and Heinzel, A., 2001. Materials for fuel-cell technologies.*Nature*, *414*(6861), pp.345-352.

[88] Wang, G., Bai, J., Wang, Y., Ren, Z. and Bai, J., 2011. Prepartion and electrochemical performance of a cerium oxide-graphene nanocomposite as the anode material of a lithium ion battery. *Scripta Materialia*, *65*(4), pp.339-342.

[89] Corma, A., Atienzar, P., Garcia, H. and Chane-Ching, J.Y., 2004. Hierarchically mesostructured doped CeO_2 with potential for solar cell use.*Nature materials*, *3*(6), pp.394-397.

[90] Fu, Q., Weber, A. and Flytzani-Stephanopoulos, M., 2001. Nanostructured Au-CeO_2 catalysts for low-temperature water–gas shift. *Catalysis Letters*,*77*(1-3), pp.87-95.

[91] Guzman, J., Carrettin, S. and Corma, A., 2005. Spectroscopic evidence for the supply of reactive oxygen during CO oxidation catalyzed by gold supported on nanocrystalline CeO_2. *Journal of the American Chemical Society*, *127*(10), pp.3286-3287.

[92] Tan, J.P.Y., Tan, H.R., Boothroyd, C., Foo, Y.L., He, C.B. and Lin, M., 2011. Three-dimensional structure of CeO_2 nanocrystals. *The Journal of Physical Chemistry C*, *115*(9), pp.3544-3551.

[93] Gupta, A., Waghmare, U.V. and Hegde, M.S., 2010. Correlation of oxygen storage capacity and structural distortion in transition-metal-, noble-metal-, and rare-earth-ion-substituted CeO_2 from first principles calculation.*Chemistry of Materials*, *22*(18), pp.5184-5198.

[94] Yen, H., Seo, Y., Guillet-Nicolas, R., Kaliaguine, S. and Kleitz, F., 2011. One-step-impregnation hard templating synthesis of high-surface-area nanostructured mixed metal oxides ($NiFe_2O_4$, $CuFe_2O_4$ and Cu/CeO_2).*Chemical Communications*, *47*(37), pp.10473-10475.

[95] Sun, C. and Xue, D., 2013. Size-dependent oxygen storage ability of nano-sized ceria. *Physical Chemistry Chemical Physics*, *15*(34), pp.14414-14419.

[96] Montini, T., Melchionna, M., Monai, M. and Fornasiero, P., 2016. Fundamentals and Catalytic Applications of CeO_2-Based Materials.*Chemical Reviews*.

[97] Lawrence, N.J., Brewer, J.R., Wang, L., Wu, T.S., Wells-Kingsbury, J., Ihrig, M.M., Wang, G., Soo, Y.L., Mei, W.N. and Cheung, C.L., 2011. Defect engineering in cubic cerium oxide nanostructures for catalytic oxidation. *Nano letters*, *11*(7), pp.2666-2671.

[98] Land, P.L., 1973. Defect equilibria for extended point defects, with application to nonstoichiometric ceria. *Journal of Physics and Chemistry of Solids*, *34*(11), pp.1839-1845.

[99] Paier, J., Penschke, C. and Sauer, J., 2013. Oxygen defects and surface chemistry of ceria: quantum chemical studies compared to experiment.*Chemical reviews*, *113*(6), pp.3949-3985.

[100] Gao, P., Kang, Z., Fu, W., Wang, W., Bai, X. and Wang, E., 2010. Electrically driven redox process in cerium oxides. *Journal of the American Chemical Society*, *132*(12), pp.4197-4201.

[101] Sheldon, B.W. and Shenoy, V.B., 2011. Space charge induced surface stresses: implications in ceria and other ionic solids. *Physical review letters*, *106*(21), p.216104.

[102] Herman, G.S., 1999. Characterization of surface defects on epitaxial CeO_2 (001) films. *Surface science*, *437*(1), pp.207-214.

[103] Sun, C., Li, H. and Chen, L., 2012. Nanostructured ceria-based materials: synthesis, properties, and applications. *Energy & Environmental Science*,*5*(9), pp.8475-8505.

[104] Trovarelli, A., 1996. Catalytic properties of ceria and CeO_2-containing materials. *Catalysis Reviews*, *38*(4), pp.439-520.

[105] Perrichon, V., Laachir, A., Abouarnadasse, S., Touret, O. and Blanchard, G., 1995. Thermal stability of a high surface area ceria under reducing atmosphere. *Applied Catalysis A: General*, *129*(1), pp.69-82.

[106] Terribile, D., Trovarelli, A., Llorca, J., de Leitenburg, C. and Dolcetti, G., 1998. The synthesis and characterization of mesoporous high-surface area ceria prepared using a hybrid organic/inorganic route. *Journal of catalysis*,*178*(1), pp.299-308.

[107] Biradar, A.V., Umbarkar, S.B. and Dongare, M.K., 2005. Transesterification of diethyl oxalate with phenol using MoO_3/SiO_2 catalyst. *Applied Catalysis A: General*, *285*(1), pp.190-195.

[108] Pengpanich, S., Meeyoo, V., Rirksomboon, T. and Bunyakiat, K., 2002. Catalytic oxidation of methane over CeO_2-ZrO_2 mixed oxide solid solution catalysts prepared via urea hydrolysis. *Applied Catalysis A: General*, *234*(1), pp.221-233.

[109] Morales, M.R., Barbero, B.P. and Cadús, L.E., 2006. Total oxidation of ethanol and propane over Mn-Cu mixed oxide catalysts. *Applied Catalysis B: Environmental*, *67*(3), pp.229-236.

[110] Machida, M., Uto, M., Kurogi, D. and Kijima, T., 2000. MnO_x-CeO_2 Binary Oxides for Catalytic NO_x Sorption at Low Temperatures. Sorptive Removal of NO_x. *Chemistry of materials*, *12*(10), pp.3158-3164.

[111] Yang, G., Tsubaki, N., Shamoto, J., Yoneyama, Y. and Zhang, Y., 2010. Confinement effect and synergistic function of H-ZSM-5/Cu-ZnO-Al_2O_3 capsule catalyst for one-step controlled synthesis. *Journal of the American Chemical Society*, *132*(23), pp.8129-8136.

[112] Roginskaya, Y.E., Morozova, O.V., Lubnin, E.N., Ulitina, Y.E., Lopukhova, G.V. and Trasatti, S., 1997. Characterization of Bulk and Surface Composition of $Co_xNi_{1-x}O_y$ Mixed Oxides for Electrocatalysis. *Langmuir*,*13*(17), pp.4621-4627.

[113] Garg, A., Mishra, I.M. and Chand, S., 2010. Oxidative Phenol Degradation Using Non-Noble Metal Based Catalysts. *CLEAN–Soil, Air, Water*, *38*(1), pp.27-34.

[114] Fan, Z., Chao, C.C., Hossein-Babaei, F. and Prinz, F.B., 2011. Improving solid oxide fuel cells with yttria-doped ceria interlayers by atomic layer deposition. *Journal of Materials Chemistry*, *21*(29), pp.10903-10906.

[115] Roy, S. and Hegde, M.S., 2008. Pd ion substituted CeO_2: A superior de-NO_x catalyst to Pt or Rh metal ion doped ceria. *Catalysis Communications*, *9*(5), pp.811-815.

[116] Bozo, C., Guilhaume, N. and Herrmann, J.M., 2001. Role of the ceria-zirconia support in the reactivity of platinum and palladium catalysts for methane total oxidation under lean conditions. *Journal of Catalysis*, *203*(2), pp.393-406.

[117] Bozo, C., Guilhaume, N., Garbowski, E. and Primet, M., 2000. Combustion of methane on CeO_2-ZrO_2 based catalysts. *Catalysis Today*, *59*(1), pp.33-45.

[118] Kaspar, J., Fornasiero, P., Balducci, G., Di Monte, R., Hickey, N. and Sergo, V., 2003. Effect of ZrO_2 content on textural and structural properties of CeO_2-ZrO_2 solid solutions made by citrate complexation route. *Inorganica Chimica Acta*, *349*, pp.217-226.

[119] Martins, R.C., Amaral-Silva, N. and Quinta-Ferreira, R.M., 2010. Ceria based solid catalysts for Fenton's depuration of phenolic wastewaters, biodegradability enhancement and toxicity removal. *Applied Catalysis B: Environmental*, *99*(1), pp.135-144.

[120] Martínez, S.S., Sanchez, J.V., Estrada, J.R.M. and Velásquez, R.F., 2011. Fe (III) supported on ceria as effective catalyst for the heterogeneous photo-oxidation of basic orange 2 in aqueous solution with sunlight. *Solar Energy Materials and Solar Cells*, *95*(8), pp.2010-2017.

[121] Gómez, L.E., Miró, E.E. and Boix, A.V., 2013. Spectroscopic characterization of Mn-Co-Ce mixed oxides, active catalysts for COPROX reaction. *International Journal of Hydrogen Energy*, *38*(14), pp.5645-5654.

[122] Gerken, J.B., Shaner, S.E., Massé, R.C., Porubsky, N.J. and Stahl, S.S., 2014. A survey of diverse earth abundant oxygen evolution electrocatalysts showing enhanced activity from Ni-Fe oxides containing a third metal. *Energy & Environmental Science*, *7*(7), pp.2376-2382.

[123] Allam, N.K., Deyab, N.M. and Ghany, N.A., 2013. Ternary Ti-Mo-Ni mixed oxide nanotube arrays as photoanode materials for efficient solar hydrogen production. *Physical Chemistry Chemical Physics*, *15*(29), pp.12274-12282.

[124] Hinokuma, S., Kogami, H., Yamashita, N., Katsuhara, Y., Ikeue, K. and Machida, M., 2014. Subnano-particle Ce catalyst prepared by pulsed arc-plasma process. *Catalysis Communications*, *54*, pp.81-85.

[125] Valiev, R., 2002. Materials science: nanomaterial advantage. *Nature*,*419*(6910), pp.887-889.

[126] Wilcoxon, J.P. and Abrams, B.L., 2006. Synthesis, structure and properties of metal nanoclusters. *Chemical Society Reviews*, *35*(11), pp.1162-1194.

[127] Feynman, R.P., 1960. There's plenty of room at the bottom. *Engineering and science*, *23*(5), pp.22-36.

[128] Ganguli, A.K., Ganguly, A. and Vaidya, S., 2010. Microemulsion-based synthesis of nanocrystalline materials. *Chemical Society Reviews*, *39*(2), pp.474-485.

[129] Chen, X. and Mao, S.S., 2007. Titanium dioxide nanomaterials: synthesis, properties, modifications, and applications. *Chemical reviews*, *107*(7), pp.2891-2959.

[130] Ganguli, A.K., Ahmad, T., Vaidya, S. and Ahmed, J., 2008. Microemulsion route to the synthesis of nanoparticles. *Pure and Applied Chemistry*, *80*(11), pp.2451-2477.

[131] Gellman, A.J. and Shukla, N., 2009. Nanocatalysis: More than speed.*Nature Materials*, *8*(2), pp.87-88.

[132] Khin, M.M., Nair, A.S., Babu, V.J., Murugan, R. and Ramakrishna, S., 2012. A review on nanomaterials for environmental remediation. *Energy & Environmental Science*, *5*(8), pp.8075-8109.

[133] Goel, C., Bhunia, H. and Bajpai, P.K., 2015. Synthesis of nitrogen doped mesoporous carbons for carbon dioxide capture. *RSC Advances*, *5*(58), pp.46568-46582.

[134] Sengupta, A., Kamble, P.D., Basu, J.K. and Sengupta, S., 2011. Kinetic study and optimization of oxidative desulfurization of benzothiophene using mesoporous titanium silicate-1 catalyst. *Industrial & Engineering Chemistry Research*, *51*(1), pp.147-157.

[135] Labille, J. and Brant, J., 2010. Stability of nanoparticles in water. *Nanomedicine*, *5*(6), pp.985-998.

[136] El-Ansary, A. and Faddah, L.M., 2010. Nanoparticles as biochemical sensors. *Nanotechnology, science and applications*, *3*, pp.65-76.

[137] Prakash, D., Amente, C., Dharamvir, K., Singh, B., Singh, R., Shaaban, E.R., Al-Douri, Y., Khenata, R., Darroudi, M. and Verma, K.D., 2016. Synthesis, Purification and Microstructural Characterization of Nickel Doped Carbon Nanotubes for spintronic applications. *Ceramics International*, 42(5), pp.5600-5606.

[138] Gawande, M.B., Branco, P.S. and Varma, R.S., 2013. Nano-magnetite (Fe_3O_4) as a support for recyclable catalysts in the development of sustainable methodologies. *Chemical Society Reviews*, *42*(8), pp.3371-3393.

[139] Polshettiwar, V. and Varma, R.S., 2010. Green chemistry by nano-catalysis. *Green Chemistry*, *12*(5), pp.743-754.

[140] Zhang, Q., Uchaker, E., Candelaria, S.L. and Cao, G., 2013. Nanomaterials for energy conversion and storage. *Chemical Society Reviews*, *42*(7), pp.3127-3171.

[141] Zhang, Y., Li, D., Chen, Y., Wang, X. and Wang, S., 2009. Catalytic wet air oxidation of dye pollutants by polyoxomolybdate nanotubes under room condition. *Applied Catalysis B: Environmental*, *86*(3), pp.182-189.

[142] Qian, J., Wang, K., Guan, Q., Li, H., Xu, H., Liu, Q., Liu, W. and Qiu, B., 2014. Enhanced wet hydrogen peroxide catalytic oxidation performances based on CuS nanocrystals/reduced graphene oxide composites. *Applied Surface Science*, *288*, pp.633-640.

Chapter 2

Material and Methods

2.1. Reagents and chemicals

The chemicals used for catalyst preparation i.e., $Fe(NO_3)_3.9(H_2O)$, $Cu(NO_3)_2.3H_2O$, $Co(NO_3)_2.6H_2O$, $Zn(NO_3)_2.6H_2O$, $Ni(NO_3)_2.6H_2O$, $Ce(NO_3)_3.6H_2O$ and NaOH were of analytical grade. The standard compounds of chlorophenols (CP) were supplied by Aldrich, (Milwaukee, WI, USA). Chlorovanillin (CV), Chloroguaiacols (CG), Chlorocatechols (CC), chlorosyringaldehyde (CSA), chlorosyringol (CS) were purchased from Helix Biotech (Richmond, BC, Canada). The solvents like acetone and *n*-hexane were of HPLC grade, ethanol and diethyl ether were of LR grade. Acetic anhydride (analytical-grade) was used after double distillation. The stock solutions of chlorophenolics were prepared in acetone:water (10:90) solution.

2.2. Wastewater sample

The wastewater sample was procured from after primary clarifier outlet of a paper industry, located in India (**Figure 2.1**). 1M H_2SO_4 solution was used to adjust the *pH* of wastewater.

2.2.1 Paper industry wastewater

Paper industry wastewater is highly polluted due to high COD (chemical oxygen demand), color, BOD (biological oxygen demand), TOC (total organic carbon), AOX (adsorbable organic halides) and CHPs (chlorophenolics) [1-3]. Approximately 700 inorganic and organic compounds have been detected in paper industry wastewater, which includes; chlorinated compounds, fatty acids, tannins, stilbenes, resin acids, lignin and its derivatives, sulfur and its compounds etc. [4,5]. Bleach plant alone accounts for 60-70% of BOD and 80-90% of color loads [6]. The dark brown color of wastewater is due to lignin and its derivatives formed during beaching [7,8].

The chlorinated compounds present in paper industry wastewater are toxic in nature. Approximately, 200 chlorinated organic compounds are reported to be present in paper industry wastewater, which are collectively estimated as AOX [4,9]. These chlorinated compounds are chloro-hydrocarbons, chloro-phenolics, chloro-resins and fatty acids, chloro-furans and dioxins,

chloroform, chlorate etc. [10,11]. Some of the compounds listed above have been classified as priority pollutants by EPA, US [12]. The toxic effects of these compounds are well reported on the daphnia, planktons and fish [13-15].

Fig. 2.1. Paper industry wastewater sample before treatment

2.3. Catalyst Synthesis

The metal oxide nanoparticles were synthesized by co-precipitation method in the following steps [16-18]:

1. Metal nitrate solutions (1M stock solution) were mixed according to the required ratios.
2. Solution was stirred for 15 min for homogeneous mixing.
3. To this solution, drop-wise addition of 0.5 M NaOH was done at 70 °C, till the *pH* value of 10 was attained.
4. After 2 h ageing, the obtained precipitates were thoroughly washed with ethanol and deionized water mixture (1:1).
5. The precipitate was dried overnight at 110 °C to obtain the hydroxide precursor.
6. Hydroxide precursor was calcined at 400 °C for 3 h, in presence of air.

2.4. Catalyst Characterization techniques

2.4.1. X-ray diffraction (XRD)

The crystal structure, phase composition, crystallite size, lattice parameters and structural imperfections of catalysts were studied from XRD analysis. The XRD analysis was performed on Bruker AXS D8 diffractometer (**Figure 2.2**) equipped with CuKα radiation (λ= 0.154 nm). The diffractograms were collected in the 2θ range 20-80°, at a scanning rate of 2° min^{-1}.

XRD is based on the unique diffraction pattern of each crystalline phase [19-21]. The obtained diffraction patterns were matched with the standard JCPDS files, published by American society for testing materials. The crystallite size was determined by the Scherrer equation:

$$D_{hkl} = \frac{0.9\lambda}{\beta_{hkl}}\cos\theta \qquad (2.1)$$

Where, D_{hkl} is crystallite size, λ is wavelength of Cu Kα radiation, β_{hkl} is full width at half maximum (FWHM) and θ is Bragg diffraction angle

Lattice parameter (a) of cubic unit cell was calculated from the equation:

$$a = d\,(h^2 + k^2 + l^2)^{1/2} \qquad (2.2)$$

Where; a is lattice constant, d is distance between two lattice planes and h, k, l are Miller indices

2.4.2. Fourier Transform-Infrared Spectroscopy (FT-IR)

FT-IR was employed as an additional tool for the identification of inorganic species [22,23]. The Infrared induced vibrations were recorded on a Perkin Elmer C91158 spectrometer at a scan speed of 4 cm^{-1} (**Figure 2.3**). The samples for FT-IR were first evacuated and then prepared by KBr pellet procedure.

Fig. 2.2. X-ray diffractometer (Bruker AXS D8)

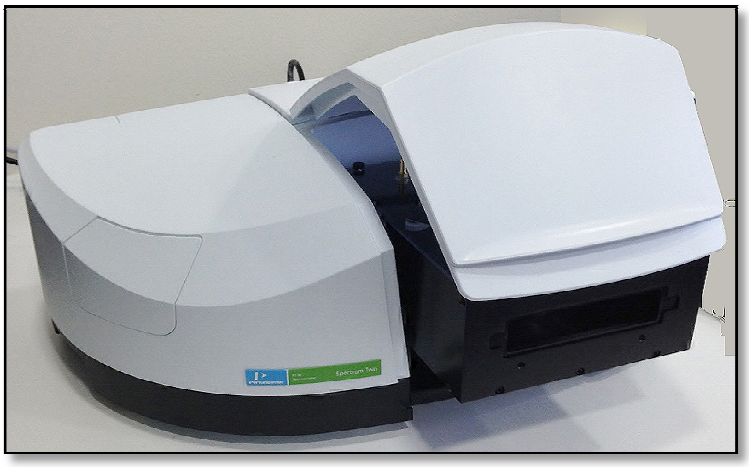

Fig. 2.3. Fourier Transform-Infrared Spectrometer (Perkin Elmer C91158)

2.4.3. Raman Spectroscopy (RS)

Raman spectroscopy was carried out to understand the structural changes in CeO_2 nanocrystals due to formation of mixed oxides and to characterize the oxygen vacancies, as it deals with the oxygen lattice vibrations [24,25]. The Raman analysis was performed on a Renishaw spectrometer (invia Raman Microscope, **Figure 2.4**), where samples were excited using the 514 nm line of Ar ion laser.

Fig. 2.4. Raman Microscope (Renishaw, invia Raman)

Fig. 2.5. X-ray photoelectron spectroscope (PHI 5000 Versa Probe II)

2.4.4. X-ray photoelectron spectroscopy (XPS)

XPS was utilized to identify the oxidation states of metals in catalyst [26-28]. The XPS spectra was recorded on a PHI 5000 Versa Probe II (**Figure 2.5**) using a monochromatized Al-Kα source (hν = 1486.6 eV). The binding energy (BE) scale was calibrated by applying the carbon 1s line (284.6 eV) as a reference charge.

2.4.5. N_2-adsorption/desorption

Gas sorption is a prominent method to study the specific surface area and porosity of material [29,30]. The adsorption isotherms were obtained by measuring the amount of adsorbed nitrogen as a function of relative pressures. Desorption isotherms were obtained by measuring the removed gas as the pressure is reduced. The shape of sorption isotherms assures the porous texture of catalyst. N_2 sorption was performed on a Quantachrome ASiQwin™ instrument (**Figure 2.6**) at liquid nitrogen temperature of -196°C. The sample was degassed under high vacuum at 120 °C for 12 h. Specific surface area was calculated by applying the Brunauer, Emmett and Teller (BET) theory to relative adsorbate pressures (p/p_o) data, and the pore size distribution (PSD) was obtained by Density functional theory (DFT). Both BET and DFT were included within the ASiQwin software. Total pore volume of samples was estimated from the volume of adsorbed nitrogen.

Fig. 2.6. Gas sorption analyzer (Quantachrome ASiQwin™)

2.4.6. Field emission scanning electron microscopy (FE-SEM)

The surface morphology of samples was studied by FE-SEM technique [31]. FE-SEM study was carried out using a Quanta 200F microscope (**Figure 2.7**) with an accelerating voltage of 20 kV. Prior to analysis, samples were subjected to gold sputtering at argon pressure of 10^{-2} mbar for 60 sec in order to create a conductive layer on their surface. The elemental composition of catalyst

was confirmed by Energy-dispersive X-ray spectrometer (EDX, Oxford Instruments, 51 XMX 1005) coupled with the FE-SEM chamber.

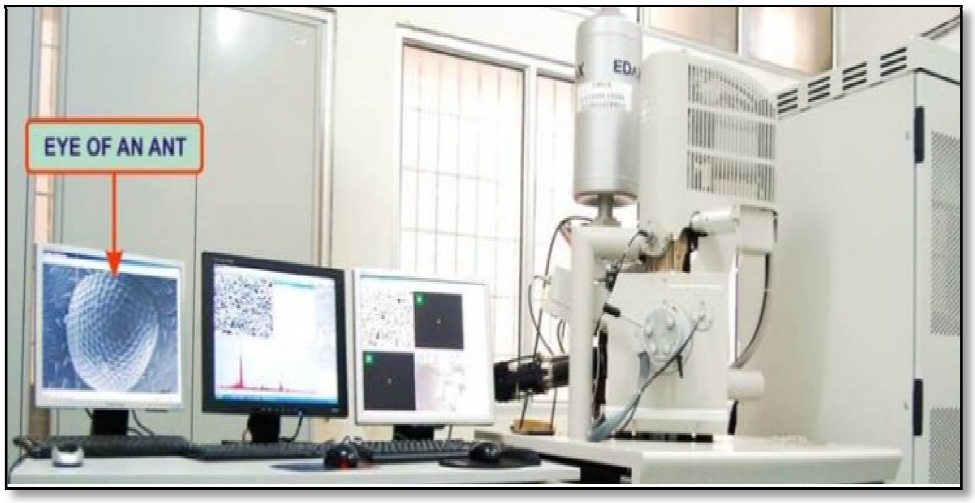

Fig. 2.7. Field emission scanning electron microscope coupled with EDX (Quanta 200F)

2.4.7. Transmission Electron Microscopy (TEM)

The detailed study of particle size and pore structure of samples was done by TEM analysis [32,33]. TEM micrographs were recorded on a Tecnai G^2 STWIN microscope, operating at 200 kV (**Figure 2.8**) was. The samples were prepared by ultrasonically dispersion in ethanol and then depositing them over a thin carbon film supported on a standard copper grid.

2.5. CWAO treatment assembly

The batch oxidative degradation experiments were carried out in a glass reactor at atmospheric pressure. The reactor (**Figure 2.9**) was equipped with a gas inlet (for oxygen supply), a condenser (to limit the loss of reaction mixture) and a stirrer (for good mass transfer). A temperature controlled water bath was used for heating the reactor. The wastewater and weighed amount of catalyst was loaded into the reactor followed by oxygen (O_2) introduction through gas inlet. All CWAO experiments were performed in duplicate. The percent removal efficiency was quantified by the following expression:

$$RE = \frac{[C_o]-[C]}{[C_o]} \times 100 \qquad (2.3)$$

Where; RE is the removal efficiency(%); C_o and C, are initial and final concentration of pollutants.

Fig. 2.8. Transmission Electron Microscope (Tecnai G^2 STWIN)

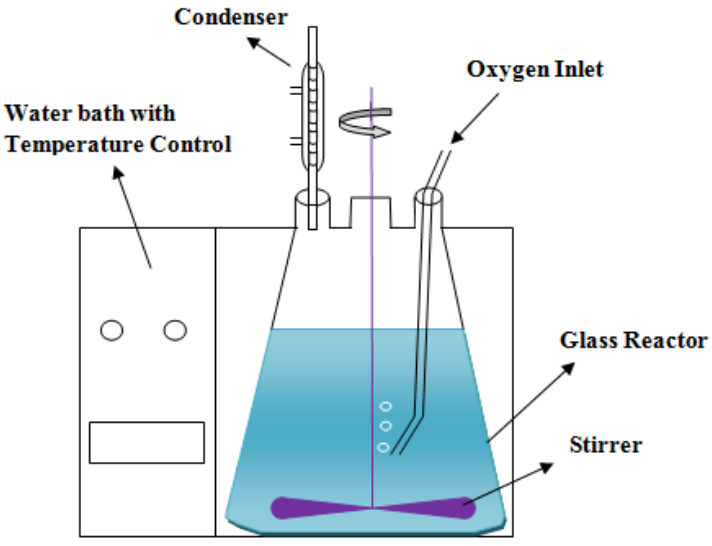

Fig. 2.9. Schematic diagram of experimental set-up for CWAO

2.6. Analytical methods for wastewater characterization

The physicochemical analysis of wastewater before and after CWAO experiments was performed according to the standard methods for wastewater analysis [34].

2.6.1. Chemical oxygen demand (COD)

COD indicates the equivalent amount of oxygen, which is required to chemically oxidize the organic compounds [35]. COD was measured by closed reflux titrimetric method, where the sample was refluxed in a mixture of chromic ($K_2Cr_2O_7$) and sulfuric acids, using a block heater operating at 150 ± 2 °C. After digestion, the amount of consumed $K_2Cr_2O_7$ was determined by titrating the unreduced $K_2Cr_2O_7$ with ferrous ammonium sulfate (FAS) in presence of ferroin indicator. COD was calculated using following expression:

$$\text{COD as mg } O_2\ L^{-1} = \frac{(A-B) \times M \times 8000}{\text{mL sample}} \qquad (2.4)$$

Where; A is FAS used for blank (mL), B is FAS used for sample (mL), M is molarity of FAS and 8000 is milli-equivalent weight of oxygen × 1000 ml L^{-1}

2.6.2. Biological Oxygen Demand (BOD)

BOD measures the biodegradable fraction of organic load in wastewater [36]. BOD_5 was determined by measuring the dissolved oxygen (DO) before and after incubation of samples at 20 °C for 5 days using following expression:

$$BOD_5\ \text{mg}\ L^{-1} = \frac{(D_1-D_2)-V_s}{P} \qquad (2.5)$$

Where; D_1 is DO of sample before incubation, D_2 is DO of sample after 5 day incubation, V_s is volume of seed and P is decimal volumetric fraction of sample

2.6.3. Color

Paper industry wastewater is highly colored [37]. The color values of wastewater were assessed by UV-Visible spectrophotometer (SPEKOL 2000, Analytic Jena) at a wavelength of 465 nm. Before color measurement, the *pH* of wastewater was adjusted to 7.6 followed by centrifugation at 1500 rpm. The color values were calculated from the calibration curve made between absorbance and color units for different concentrations of standard Pt-Co solution [38].

2.6.4. Total Organic Carbon (TOC)

TOC is an important collective parameter for the organic load of wastewater [39]. TOC value was determined by the Shimadzu TOC-L CPH TOC analyzer (**Figure 2.10**) based on catalytic combustion oxidation of organic carbon to CO_2. The analysis was carried out through difference method, where the difference between total carbon (TC) and total inorganic carbon (IC) gives the TOC value.

2.6.5. Adsorbable organic halogen (AOX)

AOX was analyzed by a Dextar AOX analyzer based on combustion ion chromatography (**Figure 2.11**). For AOX analysis, sample was firstly subjected to the activated charcoal column, where halogens get adsorbed. Halogen loaded charcoal was then offered to combustion in the stream of pure oxygen at a temperature of 900 °C. After combustion, the halogen atoms were absorbed in acetic acid through the exhaust gas of incineration furnace. The microcoulometric titration (electrochemical method) was utilized for the quantification of halogens as AOX.

Fig. 2.10. TOC analyzer (Shimadzu TOC-L CPH)

Fig. 2.11. AOX analyzer (Thermo Electron Corporation, Dextar AOX analyzer)

2.6.6. Gas Chromatography Mass Spectrometry (GC-MS)

The qualitative and quantitative analysis of chlorophenolic compounds (CHPs) was done by GC-MS. For this analysis, CHPs were first extracted from wastewater by liquid-liquid extraction method.

2.6.6.1. Extraction and Derivatization of CHPs

CHP's were extracted by following the procedure outlined by Lindstrom et al. [40]. The *pH* of wastewater (1 L) was adjusted to 2 with dilute H_2SO_4. 400 mL of diethyl ether/acetone (90/10) mixture was added to the acidic wastewater, and was kept for 48 h. The emulsion formed in the ether layer was broken by a heat gun. After 48 h, the whole ethereal extract of the sample was transferred into another separating funnel, and shaken with 0.5 M $NaHCO_3$ (5 mL) solution to remove the acidic impurities. Then the ether layer was shaken with 0.5 M NaOH (5 mL) of solution. The aqueous NaOH layer (containing CHPs) was separated and washed with diethyl ether (10 mL) for the removal of neutral impurities. Before injection into GC-MS, the extracted CHPs were converted to readily volatilized acetyl derivatives through acetylation reaction.

Acetylation was done by the procedure suggested by Abrahamsson and Xie et al. [41]. After extraction of 1 L wastewater, around 4 mL extract was obtained. Total effluent extract (4 mL) was diluted to 4.5 mL using distilled water. 0.5 M Na_2HPO_4 (0.5 mL) buffer solution was added to the diluted sample, and shaken for 2 min. Then acetic anhydride (0.5 mL) was added, and the solution

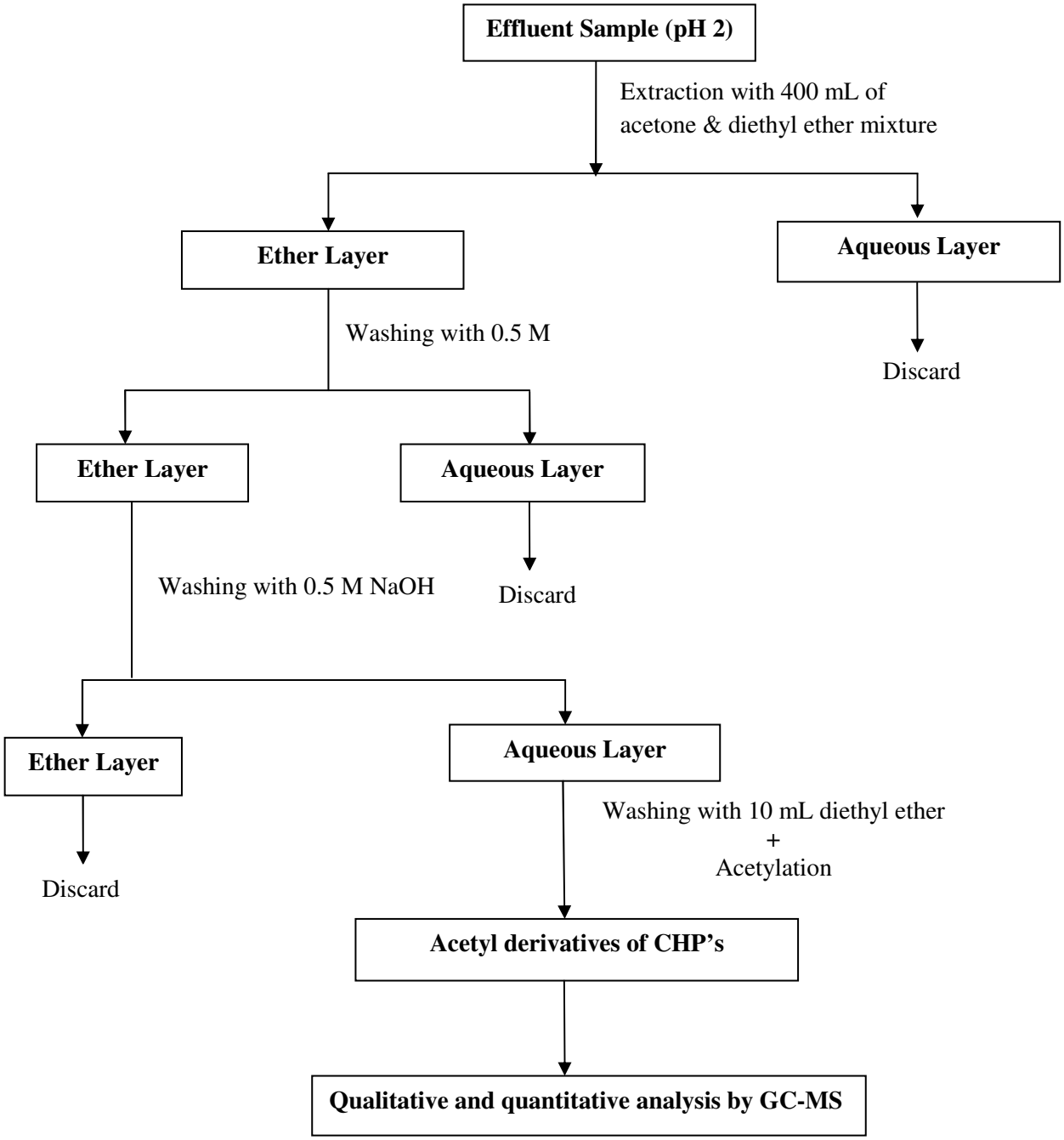

Figure 2.12. Schematic diagram for extraction of Chlorophenolic compounds from wastewater

Table 2.1. GC-MS conditions for analysis of Chlorophenolic compounds

Gas Chromatography		Mass Spectrometer	
Parameter	**Condition**	**Parameter**	**Condition**
Column	Capillary column (TR-5)	Ionization mode	Electron Impact (EI)
Column dimension	30 m x 0.25 mm	Ionising energy (eV)	70
Detector	Mass Spectrometer	Scan range (m/z)	42 to 336
Film thickness	0.25 µm	Scan speed (amu/sec)	216.7
Sample injection volume	1 µL	Fore pressure (mTorr)	38 to 45
Sample injection mode	Split less	Ion source temperature (°C)	200
Carrier gas (Flow rate)	Helium (1mL/min)	Mass transfer line (°C)	280
Injector temperature (°C)	210		
Column temperature (°C)	45 for 1 min 45 to 280 at 6°C min^{-1} 280 for 25 min^{-1}	-	-

was shaken for 5 minutes for the derivatization of CHPs. The acetyl derivatives of CHPs were extracted in 1 mL of n-hexane [42]. The acetyl derivatives from n-hexane layer were injected into GC column by an auto sampler (AI 3000, Thermo Electron Corporation). A schematic flow sheet of detailed procedure followed for CHP's extraction and derivatization is presented in **Figure 2.12**.

2.6.6.2.GC-MS conditions

GC-MS analysis was done by a Trace GC Ultra-DSQ, Thermo Electron Corporation instrument (**Figure 2.13**), equipped with a TR-5 capillary column, containing 5% phenyl methyl polysiloxane. The CHPs in wastewater (as acetyl derivative) were first identified by matching their mass spectrum with the NIST library. Once the compounds were identified, retention time (RT) was determined by injecting the pure standard solutions of respective CHP. The GC and MS conditions used are presented in **Table 2.1**.

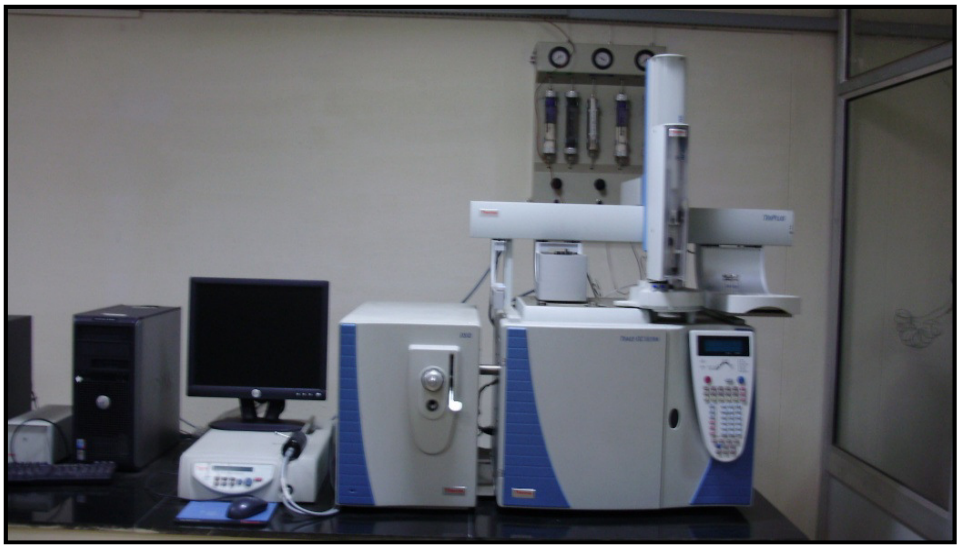

Figure 2.13. Gas Chromatograph-Mass Spectrometer (Thermo Electron Corporation, Trace GC Ultra-DSQ)

2.6.6.3.Quantitative analysis of CHPs

The quantitative analysis of CHPs was carried out with the help of calibration curve and extraction efficiency. For calibration curve, the standard solutions of CHPs were injected at different concentrations. For extraction efficiency, the standard solution (1 mL) of particular CHP was diluted to 1 L, followed by extraction and derivatization by the above mentioned procedure (section 2.6.6.1.). The derivatized sample (1 µL) was injected and the peak area was determined in order to find out the quantity of CHP in extracted sample, as outlined by Choudhary et al. [43].

2.6.7. Inductively Coupled Plasma Optical Emission Spectrometry (ICP-OES)

The amount of leached metal in wastewater after CWAO was studied by ICP-OES. It is an emission spectrophotometric technique, which is based on the excitation of component elements (atoms) in presence of plasma energy. When these excited atoms return to ground state, they emit energy at multiple wavelengths. The intensity of the emitted radiation at particular wavelength indicates the concentration of element [44,45]. ICP-OES analysis was done on a Teledyne Leeman Labs, ICP-OES, Prodigy Spec, 3043 equipment (**Figure 2.14**). The working standard solutions were prepared by diluting the standard solution (VHG Labs, LGC Standards, USA) with deionized water (using 5% HNO_3).

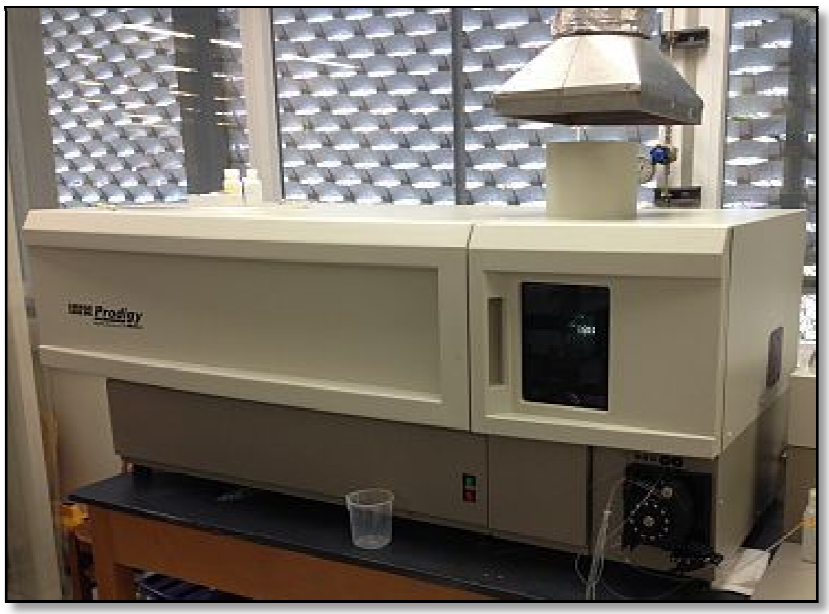

Fig. 2.14. ICP-OES spectrophotometer (Leeman Labs, ICP-OES, Prodigy Spec)

REFERENCES

[1] Kumar, P., Kumar, S. and Bhardwaj, N.K., 2012. Advanced Oxidation of ECF Bleaching Wastewater Using TiO_2 Photocatalysis. *International Journal of Environmental Science and Development*, *3*(5), p.501.

[2] Catalkaya, E.C. and Kargi, F., 2008. Advanced oxidation treatment of pulp mill effluent for TOC and toxicity removals. *Journal of environmental management*, *87*(3), pp.396-404.

[3] Savant, D.V., Abdul-Rahman, R. and Ranadi, D.R., 2005. Anaerobic digestion of absorbable organic halides (AOX) from pulp and paper industry wastewater. *Bioresource Technology*, *30*, pp.30-40.

[4] Freire, C.S., Silvestre, A.J. and Neto, C.P., 2003. Carbohydrate-derived chlorinated compounds in ECF bleaching of hardwood pulps: Formation, degradation, and contribution to AOX in a bleached kraft pulp mill. *Environmental science & technology*, *37*(4), pp.811-814.

[5] Karrasch, B., Parra, O., Cid, H., Mehrens, M., Pacheco, P., Urrutia, R., Valdovinos, C. and Zaror, C., 2006. Effects of pulp and paper mill effluents on the microplankton and microbial self-purification capabilities of the Biobio River, Chile. *Science of the Total Environment*, *359*(1), pp.194-208.

[6] Vepsäläinen, M., Kivisaari, H., Pulliainen, M., Oikari, A. and Sillanpää, M., 2011. Removal of toxic pollutants from pulp mill effluents by electrocoagulation. *Separation and purification technology*, *81*(2), pp.141-150.

[7] Monte, M.C., Fuente, E., Blanco, A. and Negro, C., 2009. Waste management from pulp and paper production in the European Union. *Waste management*, *29*(1), pp.293-308.

[8] Ali, M. and Sreekrishnan, T.R., 2001. Aquatic toxicity from pulp and paper mill effluents: a review. *Advances in environmental research*, *5*(2), pp.175-196.

[9] Deshmukh, N.S., Lapsiya, K.L., Savant, D.V., Chiplonkar, S.A., Yeole, T.Y., Dhakephalkar, P.K. and Ranade, D.R., 2009. Upflow anaerobic filter for the degradation of adsorbable organic

halides (AOX) from bleach composite wastewater of pulp and paper industry. *Chemosphere*, *75*(9), pp.1179-1185.

[10] Buyukkamaci, N. and Koken, E., 2010. Economic evaluation of alternative wastewater treatment plant options for pulp and paper industry. *Science of the total environment*, *408*(24), pp.6070-6078.

[11] Choudhary, A.K., Kumar, S. and Sharma, C., 2013. Removal of chlorophenolics from pulp and paper mill wastewater through constructed wetland. *Water Environment Research*, *85*(1), pp.54-62.

[12] Kozak, V.P., Simsiman, G.V., Chesters, G., Stensby, D. and Harkin, J., 1979. *Reviews of the environmental effects of pollutants: XI. Chlorophenols*(No. ORNL/EIS-128; EPA-600/1-79-012). Wisconsin Univ., Madison (USA). Water Resources Center.

[13] Leppänen, H. and Oikari, A., 1999. Occurrence of retene and resin acids in sediments and fish bile from a lake receiving pulp and paper mill effluents. *Environmental toxicology and chemistry*, *18*(7), pp.1498-1505.

[14] Johnsen, K., Tana, J., Lehtinen, K.J., Stuthridge, T., Mattsson, K., Hemming, J. and Carlberg, G.E., 1998. Experimental field exposure of brown trout to river water receiving effluent from an integrated newsprint mill. *Ecotoxicology and environmental safety*, *40*(3), pp.184-193.

[15] Kovacs, T.G., Martel, P.H. and Voss, R.H., 2002. Assessing the biological status of fish in a river receiving pulp and paper mill effluents. *Environmental pollution*, *118*(1), pp.123-140.

[16] Mueting, A.M., Alexander, B.D., Boyle, P.D., Casalnuovo, A.L., Ito, L.N., Johnson, B.J., and Pignolet, L. H., 1992. In "Inorganic Syntheses". (R.N. Grimes, Ed.), Vol. 29, p. 280. Wiley, New York.

[17] Poncelet, G., Jacobs, P.A. and Grange, P. eds., 1983. *Preparation of Catalysts III* (Vol. 16). Elsevier.

[18] Kingery, W.D., 1960. Introduction to ceramics, *Wiley, New York.*

[19] Jenkins, R. and Snyder, R.L., 1996. Diffraction theory. *Introduction to X-ray Powder Diffractometry, Volume 138*, pp.47-95.

[20] Moore, D.M. and Reynolds, R.C., 1989. *X-ray Diffraction and the Identification and Analysis of Clay Minerals* (Vol. 378). Oxford: Oxford university press.

[21] Suryanarayana, C. and Norton, M.G., 1998. X-ray diffraction: a practical approach. *Microsc Microanal*, New York.

[22] Schrader, B., 1995. Infrared and Raman Spectroscopy: Methods and Applications. VCH Publisheres. *New York*.

[23] Skoog, D.A., Holler and F.J., Nieman, T.A., 1998. Principles of Instrumental Analysis, 5th ed., Saunders College Publishing, Philadelphia.

[24] Turrell, G. and Corset, J. eds., 1996. Raman microscopy: developments and applications. Academic Press, San Diego.

[25] Lewis, I.R. and Edwards, H., 2001. Handbook of Raman spectroscopy: from the research laboratory to the process line. CRC Press, Dekker: New York.

[26] Al-Dhhan, Z.T., Hashemi, T. and Hogarth, C.A., 1989. X-ray photoelectron spectroscopy of dielectric films of CeO_2, CeO_2/Cd, and CeO_2/SiO prepared by thermal evaporation. *Spectrochimica Acta Part B: Atomic Spectroscopy*, *44*(2), pp.205-208.

[27] Rivière, J.C. and Myhra, S. eds., 2009. Handbook of surface and interface analysis: methods for problem-solving. CRC Press, New York.

[28] Reshak, A.H., Khenata, R., Kityk, I.V., Plucinski, K.J. and Auluck, S., 2009. X-ray photoelectron spectrum and electronic properties of a noncentrosymmetric chalcopyrite compound HgGa2S4: LDA, GGA, and EV-GGA. *The Journal of Physical Chemistry B*, *113*(17), pp.5803-5808.

[29] Haul, R., 1969. Adsorption, Surface Area and Porosity. *Zeitschrift für Physikalische Chemie*, *63*(1-4), pp.220-221.

[30] Sing, K., 2001. The use of nitrogen adsorption for the characterisation of porous materials. *Colloids and Surfaces A: Physicochemical and Engineering Aspects*, *187*, pp.3-9.

[31] Goldstein, J., Newbury, D.E., Echlin, P., Joy, D.C., Romig Jr, A.D., Lyman, C.E., Fiori, C. and Lifshin, E., 2012. *Scanning electron microscopy and X-ray microanalysis: a text for biologists, materials scientists, and geologists*. Springer Science & Business Media.

[32] Bhushan, B. and Marti, O., 2010. *Scanning probe microscopy–principle of operation, instrumentation, and probes* (pp. 573-617). Springer Berlin Heidelberg.

[33] Pyrz, W.D. and Buttrey, D.J., 2008. Particle size determination using TEM: a discussion of image acquisition and analysis for the novice microscopist. *Langmuir*, *24*(20), pp.11350-11360.

[34] Eaton, A.D., Clesceri, L.S., Rice, E.W. and Greenberg, A.E., 2008. Standard methods for the examination of water and wastewater, *American Public Health Association*, Washington, USA.

[35] Henze, M., Harremoes, P., la Cour Jansen, J. and Arvin, E., 2001.*Wastewater treatment: biological and chemical processes*. Springer Science & Business Media. Springer, Germany.

[36] Brookman, S.K.E., 1997. Estimation of biochemical oxygen demand in slurry and effluents using ultra-violet spectrophotometry. *Water Research*, *31*(2), pp.372-374.

[37] Pearce, C.I., Lloyd, J.R. and Guthrie, J.T., 2003. The removal of colour from textile wastewater using whole bacterial cells: a review. *Dyes and pigments*, *58*(3), pp.179-196.

[38] Choudhary, A.K., Kumar, S. and Sharma, C., 2010. Removal of chemical oxygen demand and color from pulp and paper mill wastewater using horizontal subsurface flow constructed wetland. In *Proceedings of the International conference on emerging technologies for sustainable environment,* Aligarh, India.

[39] Najm, I., and Marcinko, J. (1995). Impact of Analytical Methodology and Water Quality on TOC Analytical Results. Proceedings of the 1995 Water Quality Technology Conference, pp. 71-77.

[40] Lindström, K. and Nordin, J., 1976. Gas chromatography-mass spectrometry of chlorophenols in spent bleach liquors. *Journal of Chromatography A*,*128*(1), pp.13-26.

[41] Abrahamsson, K. and Xie, T.M., 1983. Direct determination of trace amounts of chlorophenols in fresh water, waste water and sea water. *Journal of Chromatography A*, *279*, pp.199-208.

[42] Sharma, C., Mohanty, S., Kumar, S. and Rao, N.J., 1996. Gas chromatographic analysis of chlorophenolic, resin and fatty acids in chlorination and caustic extraction stage effluent from Kahi-grass. *Analyst*, *121*(12), pp.1963-1967.

[43] Choudhary, A.K., Kumar, S. and Sharma, C., 2015. Removal of chloro-organics and color from pulp and paper mill wastewater by polyaluminium chloride as coagulant. *Desalination and Water Treatment*, *53*(3), pp.697-708.

[44] Olesik, J.W., 1991. Elemental Analysis Using ICP-OES and ICP/MS. *Analytical Chemistry*, *63*(1), pp.12A-21A.

[45] Cornelis, R., Caruso, J., Crews, H. and Heumann, K., 2003. Handbook of Elemental Speciation: Techniques and Methodology, *John Wiley & Sons*, Chichester, England.

Chapter 3

Fe-Ce Nanocatalysts: Characterization and Application in CWAO

Fe_2O_3 is gaining remarkable interest in many scientific and industrial fields, as it is cheap, abundant, easy to synthesize and environmentally benign [1]. Fe_2O_3 based materials are particularly appealing in the field of oxidation catalysis [2,3]. A number of studies indicated the environmental applications of Fe_2O_3 based materials. The yolk-shell Fe_2O_3@mesoporous SiO_2 nanoreactors achieved 90% degradation of methylene blue through Fenton-like reaction [4]. Graphene oxide-Fe_2O_3 (GO-Fe_2O_3) hybrid material exhibited 99% discoloration and 76% TOC removal during the photo-Fenton degradation of Rhodamine B [5]. Iron-cerium mixed oxide was efficient photocatalyst in degradation of phenol (13%), methylene blue (93%) and congo red (100%) [6]. Fe_2O_3/SBA-15 achieved 66% TOC conversion of phenolic effluent through catalytic wet peroxide oxidation (CWPO) [7]. $Ce_{1-x}Fe_xO_2$ solid solution was also efficient in the oxidation of CO [8,9].

Based on these oxidation applications of Fe_2O_3, it was selected for the formation of mixed oxide with CeO_2. A series of $Ce_{1-x}Fe_xO_2$ mixed oxides (x = 0, 0.2, 0.4, 0.5, 0.6, 0.8, and 1) were synthesized by co-precipitation method (discussed in Chapter 2) and characterized by various techniques. Present chapter deals with the result and discussions related to the structural and textural characteristics of $Ce_{1-x}Fe_xO_2$ mixed oxides, followed by their activity towards CWAO of wastewater.

3.1. Characterization of $Ce_{1-x}Fe_xO_2$ mixed oxides

3.1.1. XRD analysis

The phase composition, crystal structure, crystallite sizes, lattice parameters and structural imperfections of catalysts were studied from X-ray diffraction (XRD) analysis. XRD patterns of $Ce_{1-x}Fe_xO_2$ mixed oxides are presented in **Figure 3.1 (a)**. XRD patterns illustrated the effect of incorporation of Fe ions into ceria matrix with varied composition. The diffraction pattern for CeO_2 match well with the characteristic cubic peaks at 2θ values of 28.5°, 33°, 47.4°, 56.3°, corresponding to (111), (200), (220), (311) crystal planes, respectively (JCPDS 81-0792).

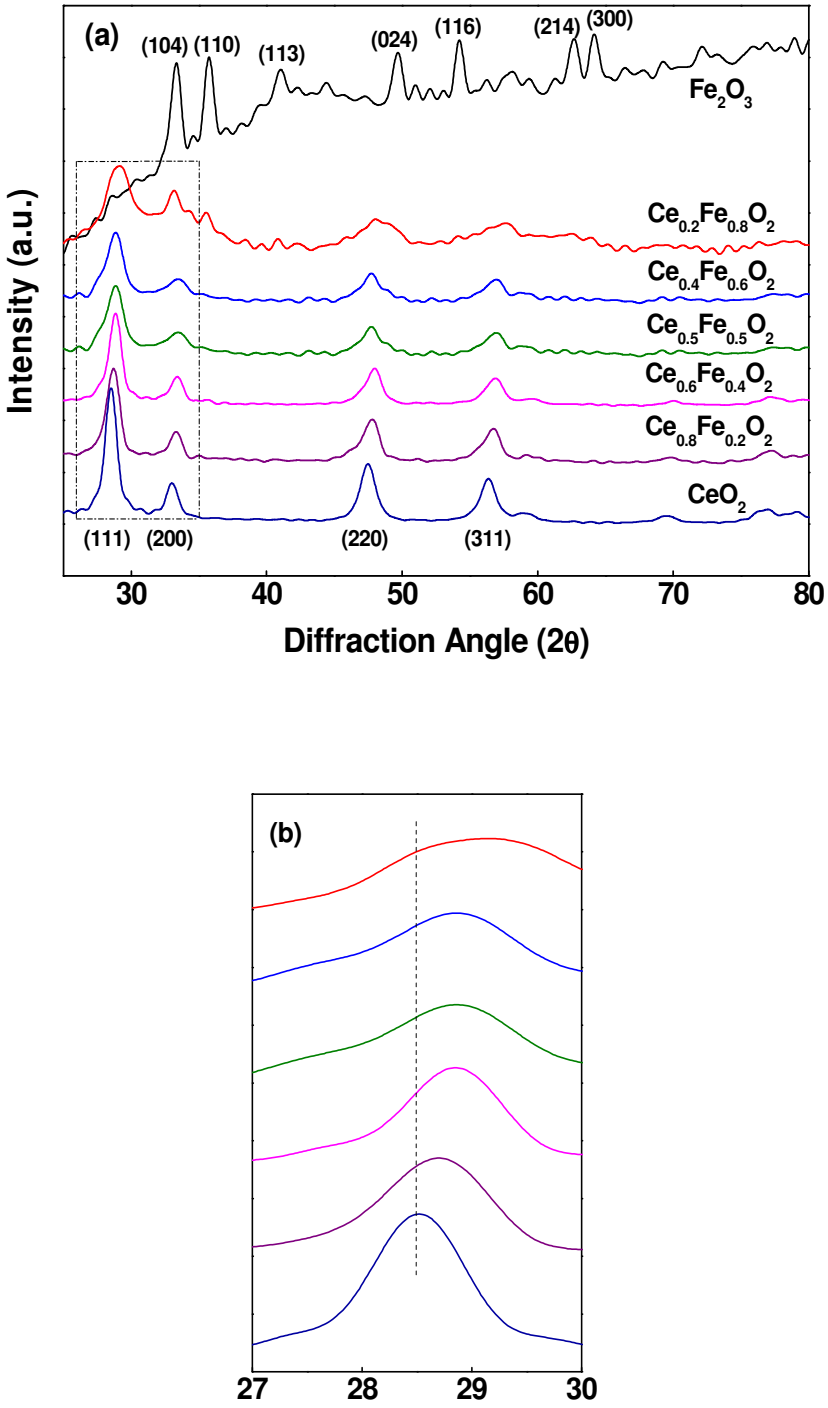

Fig.3.1. (a) XRD pattern of samples (b) low angle region from 27-30°

For Fe_2O_3, all the reflections were characteristic of tetragonal hematite structure with peaks at 2θ values of 33.1°, 35.6°, 49.4°, 54°, 62.4°, 64°, corresponding to (104), (110), (024), (116), (214), (300) crystal planes, respectively (JCPDS 86-0550). In mixed oxides, no peak corresponding to Fe_2O_3 phase was found upto $x \leq 0.6$. A weak diffraction peak at 2θ value of 35.4° corresponding to (110) crystal plane of Fe_2O_3 was obtained in $Ce_{0.2}Fe_{0.8}O_2$ mixed oxide. It showed the successful incorporation of Fe into ceria lattice upto x=0.6, while in case of $Ce_{0.2}Fe_{0.8}O_2$ precipitation of Fe_2O_3 takes place as a separate phase. For mixed oxides the characteristic ceria peaks (111) were shifted to higher angles (28.5 to 28.7°), indicating the decrease in lattice parameter and hence increased lattice deformation [9]. The shifting is shown in the low angle region from 27 to 30° **(Figure 3.1(b))**. Similar findings have also been reported by Sirichaipraserta et al. [10].

The average crystallite size and lattice parameters are presented in **Table 3.1**. As expected, the crystallite size of CeO_2 was smaller in mixed oxides. There was no significant change in the crystallite size of Fe_2O_3, indicating the formation of CeO_2-like solid solution. This decrease in crystallite size was related to the presence of dopant ions (Fe), which inhibited the grain growth [11,12]. As expected, the lattice parameter of CeO_2 was decreased for mixed oxides. This decrease was due to the small ionic radii of Fe ions, which contributed to CeO_2 lattice contraction [13,9]. The overall trend of decrease in lattice parameters was in accordance with the previous studies [14-16]. This lattice contraction indicated the presence of oxygen vacancies in mixed oxides [17,18].

3.1.2. FTIR analysis

The interaction between two phases was ascertained by FT-IR study. FTIR spectra of CeO_2, $Ce_{0.4}Fe_{0.6}O_2$ and Fe_2O_3 catalysts are presented in **Figure 3.2**. CeO_2 showed a broad band at 560 cm^{-1}, corresponding to Ce-O vibrations [19]. Fe_2O_3 exhibited two strong bands at 540 cm^{-1} and 464 cm^{-1}, which can be assigned to Fe-O bonds in the internal structure of Fe_2O_3 [20]. For $Ce_{0.4}Fe_{0.6}O_2$ mixed oxide, Fe-O band at 540 cm^{-1} was shifted to 510 cm^{-1} and second band at 464cm^{-1} was decreased to 430cm^{-1}. This red shift (decrease in frequency) was due to increase in lattice parameter from Fe_2O_3 (5.043 Å) to $Ce_{0.4}Fe_{0.6}O_2$ (5.069 Å), which is in agreement with the results reported by Harish et al. [21]. Decreased band intensity for $Ce_{0.4}Fe_{0.6}O_2$ mixed oxide supported the interaction between CeO_2 and Fe_2O_3 phases.

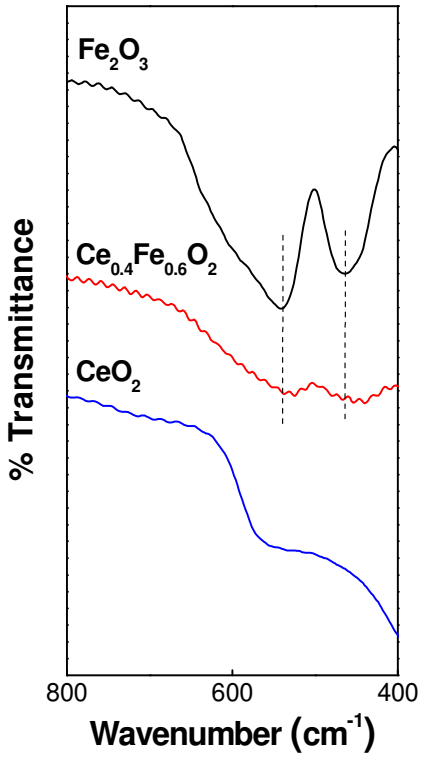

Fig.3.2. FTIR spectra of catalysts

3.1.3. Raman analysis

Raman spectroscopy was carried out to characterize the oxygen vacancies, as it is sensitive to the crystal symmetry and deals with the oxygen lattice vibrations. Raman spectra of $Ce_{1-x}Fe_xO_2$ catalysts are presented in **Figure 3.3 (a)**. CeO_2 exhibited a prominent F_{2g} peak at 460 cm^{-1}, corresponding to symmetric breathing mode of oxygen atoms around cerium ions (Ce^{4+}) [22,23]. For $Ce_{1-x}Fe_xO_2$ mixed oxides, a weak and less-prominent broad band was observed at 530 to 740 cm^{-1}. This broad band was deconvoluted in two bands centred at 600 cm^{-1} and 675 cm^{-1}. First band at 600 cm^{-1} was due to the Raman inactive LO mode caused by relaxation of symmetry selection rules [24-26].

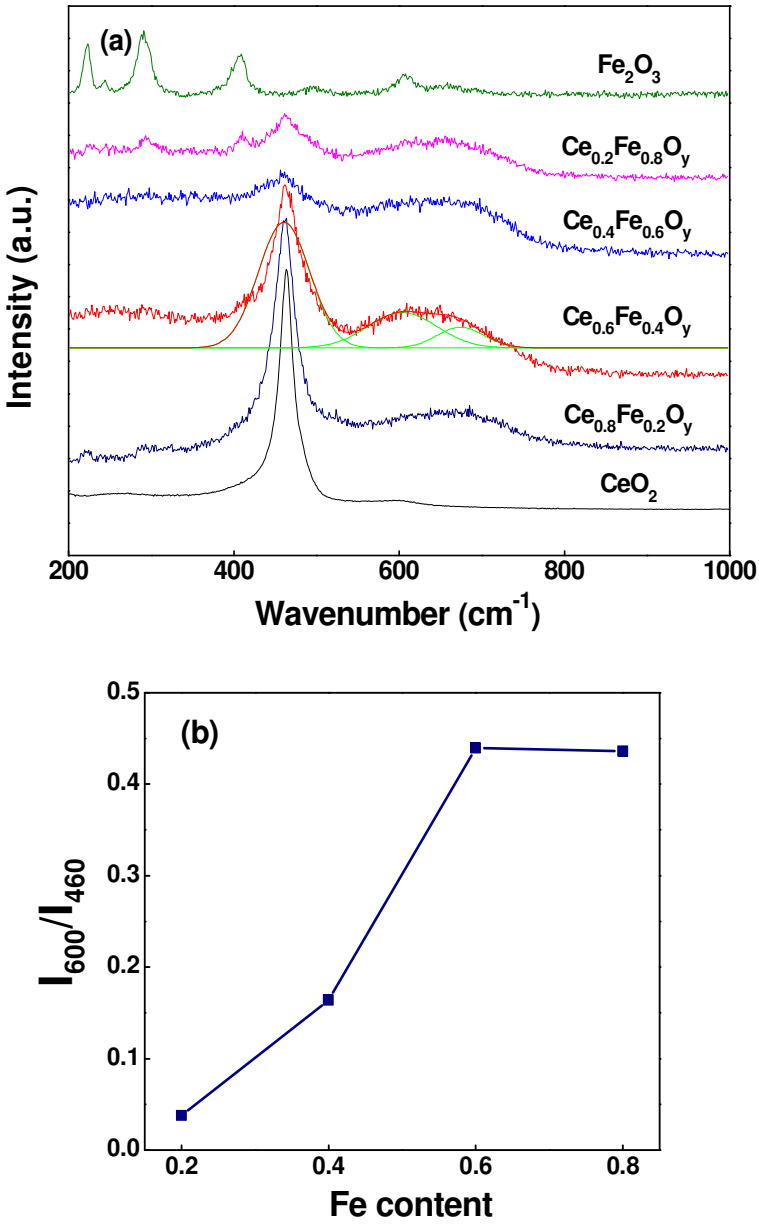

Fig.3.3. (a) Raman spectra of catalysts (b) variation of I_{600}/I_{460} with Fe content

In particular, this band was attributed to the intrinsic oxygen vacancies which are formed due to the presence of Ce^{3+}. Second weak band at 675 cm^{-1} indicated the presence of small amount of Fe_3O_4 in the surface layer of mixed oxide. The shifting of Raman peaks was related to the structural changes in mixed oxides, as suggested by XRD analysis. The concentration of oxygen vacancies was compared by calculating the intensity ratio of bands at 600 and 460 cm^{-1} [27]. **Figure 3.3 (b)** shows the variation of I_{600}/I_{460} as a function of Fe concentration. The I_{600}/I_{460} was

increased with increasing Fe content and reached a maximum for $Ce_{0.4}Fe_{0.6}O_2$ mixed oxide. The value of I_{600}/I_{460} was significantly higher than the previous reports [28,29], indicating appreciably high concentration of oxygen vacancies. Fe_2O_3 exhibited the Raman peaks at 225, 245, 292, 408 and 497 cm^{-1}, corresponding to α-Fe_2O_3 [30].

3.1.4. XPS analysis

The oxidation state of metal ions in $Ce_{0.4}Fe_{0.6}O_2$ mixed oxide was confirmed by XPS spectra deconvoluted using a peak fitting process. Ce 3d spectra **(Figure 3.4 (a))** exhibited three main $3d_{5/2}$ features at the binding energies of 881.8 eV, 887.6 eV, 897.4 eV corresponding to v, v″, v‴ components, respectively. The $3d_{3/2}$ feature corresponding to u, u″ and u‴ component were observed at 899.9 eV, 906.1 eV and 915.7 eV. The v, v″, v‴, u, u″ and u‴ peaks are characteristic of Ce^{4+} oxidation state (CeO_2), with v and u splitting of 18.4 eV. Additional peaks corresponding to v′ (884 eV), u′ (902 eV), v^o (880.8 eV) and u^o (899 eV) components indicated the presence of Ce^{3+} [31]. These results are in good accordance with the previous studies [32,33]. The atomic fraction of Ce^{3+} was calculated from the integrated peak areas according to the following equations:

$$Ce^{3+} = v^o + v' + u^o + u' \quad (3.1)$$

$$Ce^{4+} = v + v'' + v''' + u + u'' + u''' \quad (3.2)$$

$$\% Ce^{3+} = \frac{Ce^{3+}}{Ce^{3+}+Ce^{4+}} \quad (3.3)$$

Ce^{3+} percentage was found to be 28%, confirming the under stoichiometric ceria. This percentage indicates the significant oxygen vacancies as stated in earlier reports [34-36]. Some theoretical studies have related the presence of Ce^{3+} to the formation of oxygen vacancies [37,38]. **Figure 3.4 (b)** presents the Fe 2p core level binding energy spectra for $Ce_{0.4}Fe_{0.6}O_2$ mixed oxide. The peak profile indicated strong binding energies centered at around 709.4 eV and 723 eV assigned to Fe^{2+}. The peaks centered at about 711.5 and 725 eV can be ascribed to Fe^{3+} in the spinal structure. The spectra also exhibited well-defined shake-up satellite peaks at 716.8 eV and 731.7 eV [39-41]. O 1s spectra **(Figure 3.4 (c))** exhibited three components, the relative percentage of each component is provided in parenthesis. The peak centered at 528.5 eV was related to the lattice oxygen/ structural oxygen (69.5%). The peak at 531.4 eV indicated the presence of adsorbed surface

oxygen in the form of OH ions (9.4%). The additional peak at 530.2 eV was related to the supercharged oxygen (O_2^-) near oxygen vacant sites at the surface (21%) [42]. This particular peak evidenced the oxygen storage/release capacity of the nanocatalyst [43,44]. Thus XPS analysis indicated the presence of oxygen vacancies accompanied with Ce^{4+} reducing to Ce^{3+} in presence of Fe^{3+} and Fe^{2+} ions.

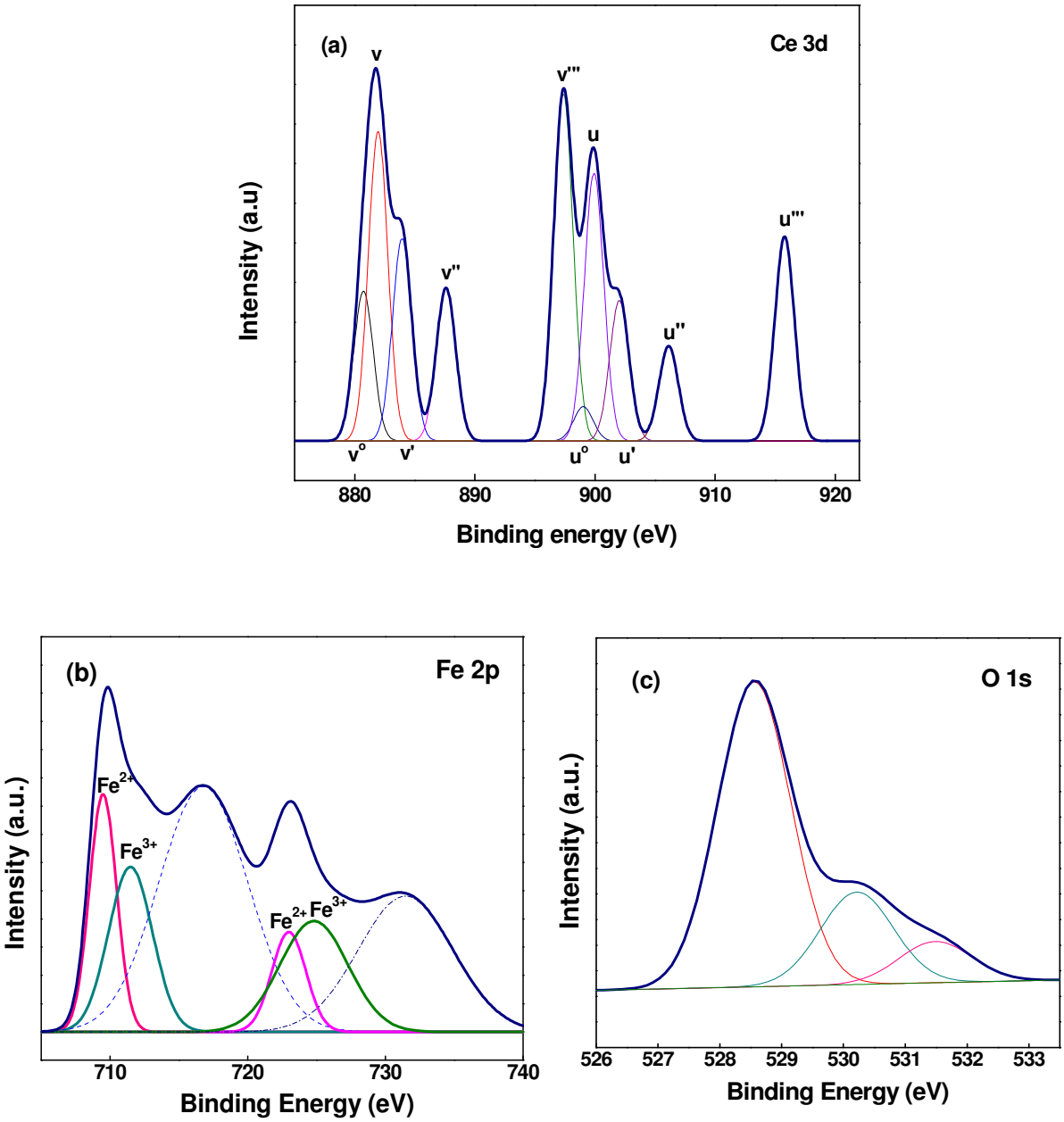

Fig.3.4. Fitted XPS spectra of $Ce_{0.4}Fe_{0.6}O_2$ mixed oxide (a) Ce 3d (b) Fe 2p (c) O 1s

3.1.5. N_2-adsorption/desorption analysis

The adsorption-desorption isotherm of CeO_2, $Ce_{0.4}Fe_{0.6}O_2$ and Fe_2O_3 catalysts are presented in **Figure 3.5 (a)**. The inflection in adsorption isotherm at high relative pressure indicated the presence of secondary pores. The desorption isotherms gave rise to the narrow hysteresis, indicating the irregular shape of pores [45]. Pore size distribution (PSD) confirmed the presence of pores with wide distribution for CeO_2 and Fe_2O_3 (**Figure 3.5 (b)**. $Ce_{0.4}Fe_{0.6}O_2$ mixed oxide presented relatively uniform pores of 3-5 nm. The BET specific surface areas of catalysts along with pore volume are listed in **Table 3.1**. Pure CeO_2 exhibited low specific surface area of 20 m^2/g and pore volume of 0.0897 cc/g. Surface areas and pore volume were found to increase with increasing Fe content and reached the maximum (149 m^2g^{-1}, 0.283 ccg^{-1}) for $Ce_{0.4}Fe_{0.6}O_2$ mixed oxide. The surface area and pore volume of $Ce_{1-x}Fe_xO_2$ mixed oxides are appreciably higher than the previous reports on Ce-Fe mixed oxides synthesized by sol-gel [46], chemical looping [47] and co-precipitation method [8,9]. The surface area of $Ce_{1-x}Fe_xO_2$ catalysts was comparable to the study by Liang et al. [48], where synthesis was carried out by impregnation method using the carbon material as a template (3234 m^2 g^{-1}, 1.78 ccg^{-1}). Thus, N_2-sorption measurements indicated the suitability of Fe-Ce mixed oxides for catalytic applications [49].

Table 3.1. Structural and textural parameters of $Ce_{1-x}Fe_xO_2$ mixed oxides

Sample	Crystallite size (nm)[a]	Lattice parameter (Å)[a]	Average particle size (nm)[c]	Specific surface area (m^2/g)[d]	Total pore volume (cc/g)[d]
CeO_2	10.6	5.416	45 ± 4	20	0.089
$Ce_{0.8}Fe_{0.2}O_2$	7.1	5.385	28 ± 2	94	0.256
$Ce_{0.6}Fe_{0.4}O_2$	6.7	5.355	23 ± 3	97	0.269
$Ce_{0.5}Fe_{0.5}O_2$	6	5.347	20 ± 3	109	0.256
$Ce_{0.4}Fe_{0.6}O_2$	5.5	5.332	17 ± 1	149	0.283
$Ce_{0.2}Fe_{0.8}O_2$	5, 8.5[b]	5.229, 5.047[b]	14 ± 2, 37 ± 3	135	0.252
Fe_2O_3	9.5[b]	5.043[b]	35 ± 5	35	0.176

[a]Calculated from (111) peak of CeO_2, [b] (110) peak of Fe_2O_3, [c] FE-SEM images, [d] N_2-adsorption/desorption

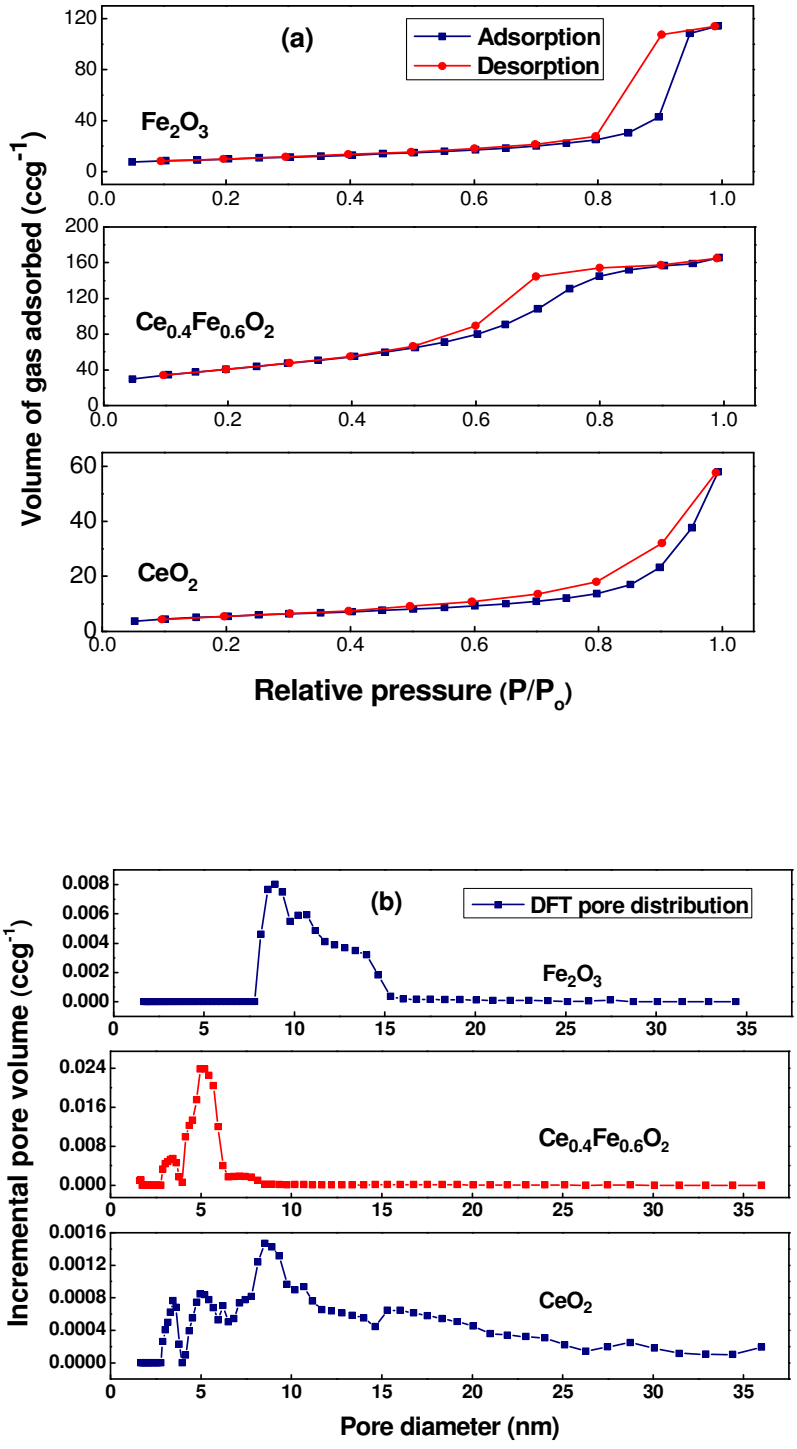

Fig.3.5. (a) N_2 adsorption-desorption isotherm (b) Pore size distribution

3.1.6. FE-SEM and TEM analysis

The microstructures of $Ce_{1-x}Fe_xO_2$ mixed oxides were investigated by FE-SEM and TEM analysis. **Figure 3.6** shows the FE-SEM micrographs of all samples and the particle size ranges are mentioned in **Table 3.1**. The micrographs clearly illustrated that all these samples were aggregated nanoparticles. The average particle size of CeO_2 was 45 nm which decreased to 28 nm for $Ce_{0.8}Fe_{0.2}O_2$ mixed oxide. Further increase in Fe content resulted in considerably decreased particle size. These results are in good agreement with XRD analysis. EDX spectra of mixed oxides are presented in **Figure 3.7**, and the expected as well as obtained values of Ce/Fe mole ratio are provided in **Table 3.2**. EDX analysis confirmed that the obtained mole ratio of Ce/Fe was close to the expected values, confirming the presence of Ce and Fe with required mole ratio.

More detailed characterization of particle size and pore structure of catalysts was performed by TEM analysis (**Figure 3.8**). TEM micrographs revealed the presence of disordered pores, which is in accordance with N_2-sorption analysis. Statistical analysis of micrographs revealed that the mean diameter of CeO_2, $Ce_{0.4}Fe_{0.6}O_2$ and Fe_2O_3 particles was 16, 8 and 6 nm, respectively. SAED pattern of $Ce_{0.4}Fe_{0.6}O_2$ confirmed its polycrystalline nature as the diffraction rings were attributable to (111), (220), (220), (311) planes of cubic CeO_2 and (104), (116) planes of Fe_2O_3.

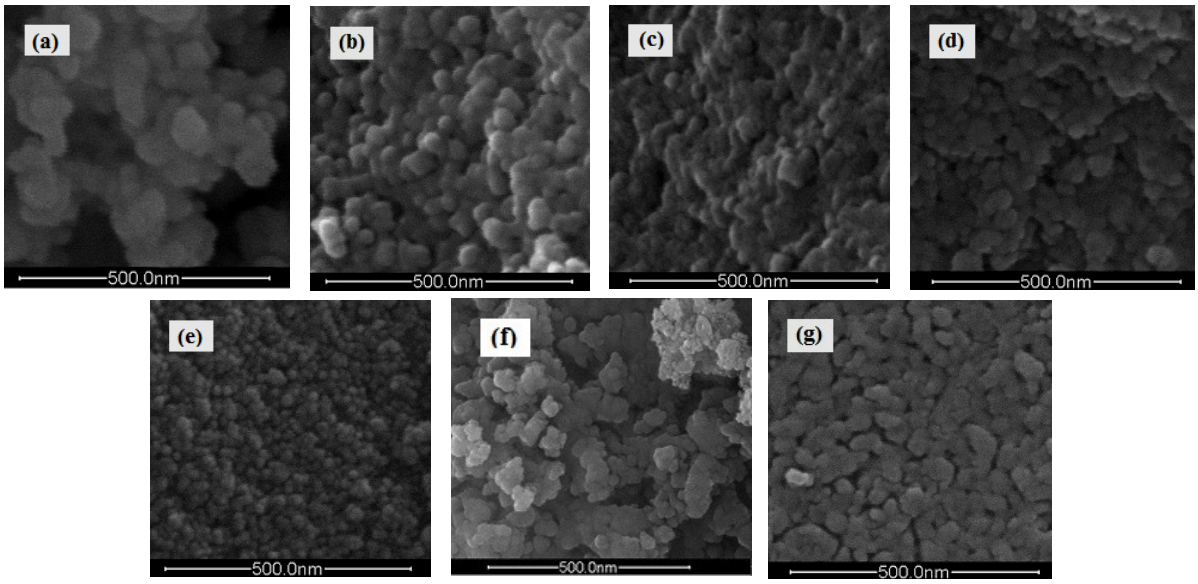

Fig.3.6. FE-SEM micrograph of (a) CeO_2 (b) $Ce_{0.8}Fe_{0.2}O_2$ (c) $Ce_{0.6}Fe_{0.4}O_2$ (d) $Ce_{0.5}Fe_{0.5}O_2$ (e) $Ce_{0.4}Fe_{0.6}O_2$ (f) $Ce_{0.2}Fe_{0.8}O_2$ (g) Fe_2O_3

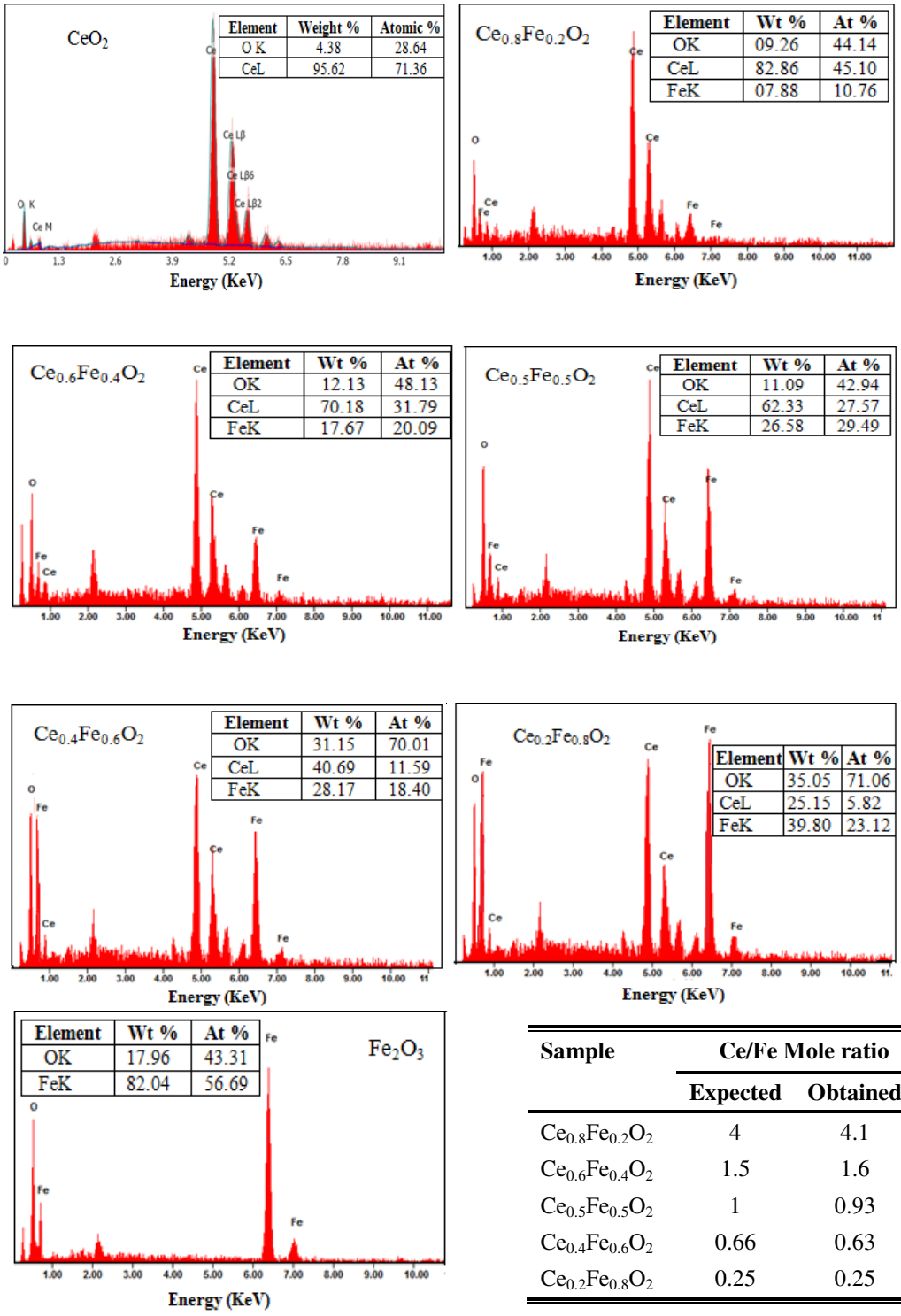

Fig.3.7. EDX spectra of catalysts

Sample	Ce/Fe Mole ratio	
	Expected	Obtained
$Ce_{0.8}Fe_{0.2}O_2$	4	4.1
$Ce_{0.6}Fe_{0.4}O_2$	1.5	1.6
$Ce_{0.5}Fe_{0.5}O_2$	1	0.93
$Ce_{0.4}Fe_{0.6}O_2$	0.66	0.63
$Ce_{0.2}Fe_{0.8}O_2$	0.25	0.25

Table 3.2. Ce/Fe mole ratio from EDX

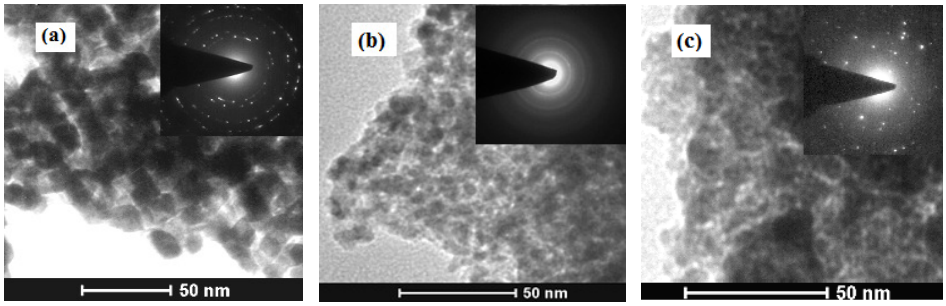

Fig.3.8. TEM micrograph and SAED pattern (a) CeO_2 (b) $Ce_{0.4}Fe_{0.6}O_2$ (c) Fe_2O_3

3.2. Optimization of operating parameters

The paper industry wastewater exhibited high organic load in terms of COD, color, TOC, AOX and CHPs **(Table 3.3)**. The influence of various reaction variables i.e. *pH* (3.0-8.0), reaction temperature (40-90°C), reaction time (0.5-2.5 h) and catalyst dose (0.5-2 g/L) on treatment efficiency was studied and the results are presented below.

3.2.1. Effect of pH

The *pH* of solution is an important parameter for catalysis, as it affects the catalyst charge [50]. Influence of initial *pH* was studied in the range of 3.0 to 8.0, using 1 gL^{-1} $Ce_{0.4}Fe_{0.6}O_2$ at 70°C for 2 h. The results are presented in **Figure 3.9 (a)**. Maximum removal of COD (65%) and color (80%) was obtained at *pH* 3, which decreased slightly at *pH* 4 (COD 63% and color 78%); after that the removal efficiency dropped significantly. High efficiency in acidic medium can be related to the positive charge of catalyst surface (isoelectric point of CeO_2=6.7; Fe_2O_3=8.4), which facilitates the adsorption of anionic organic pollutants present in paper industry wastewater [51]. Therefore, *pH* 4 was selected as optimum value for further studies.

3.2.2. Effect of temperature

The effect of temperature was studied in the range of 40 to 90°C, using 1 gL^{-1} $Ce_{0.4}Fe_{0.6}O_2$ at *pH* 4 for 2 h. **Figure 3.9 (b)** presents the removal of COD and color with increasing reaction temperature. The raise of temperature from 40 to 50°C produces only a slight increase in removal efficiencies. After that removal efficiency increased steadily and the maximum removal was attained at 90°C. This increase can be related to the accelerated oxygen supercharging of small

particles with increasing temperature [52]. Therefore 90°C was selected as optimum temperature for further studies.

Table 3.3. Average value of environmental parameters of wastewater

Parameter	Value
Color (mg Pt-Co/L)	2768 ± 114.46
COD (mg/L)	865 ± 32.14
TOC (mg L^{-1})	172.3 ± 4.8
AOX(mg L^{-1})	16.2 ± 0.35
CHPs(μg L^{-1})	485 ± 4.45
BOD_5 (mg/L)	234 ± 12.84
BOD_5/COD	0.27

3.2.3. Effect of reaction time

The reaction time was optimized within time interval of 0.5 to 2.5 h under the treatment conditions; 1 gL^{-1} $Ce_{0.4}Fe_{0.6}O_2$ catalyst, 90°C, *pH* 4. A rapid decrease in COD and color was attained with increase in treatment time up to 2 h and thereafter reached a nearly constant value **(Figure 3.9 (c))**. The wastewater contains large amount of organic pollutants and decrease in the rate of degradation after 2 h may be due to the adsorption of organic matter on catalyst surface, which hinders the oxidation process by decreasing the oxygen supply to catalyst surface and increasing competition for active sites between the reaction intermediates and organic matter [53,54]. Hence, a 2 h reaction time was selected as optimum for further experiments.

3.2.4. Effect of catalyst dose

The influence of catalyst dose was studied by varying the $Ce_{0.4}Fe_{0.6}O_2$ dose from 0.5 to 2 gL^{-1} at 90°C, *pH* 4 for 2 h. The removal efficiency increased rapidly with increasing catalyst concentration upto 1 gL^{-1} **(Figure 3.9 (d))**. Further increase in amount of catalyst resulted in a slight increase in removal efficiency. Therefore catalyst dose of 1 gL^{-1} was chosen as optimum.

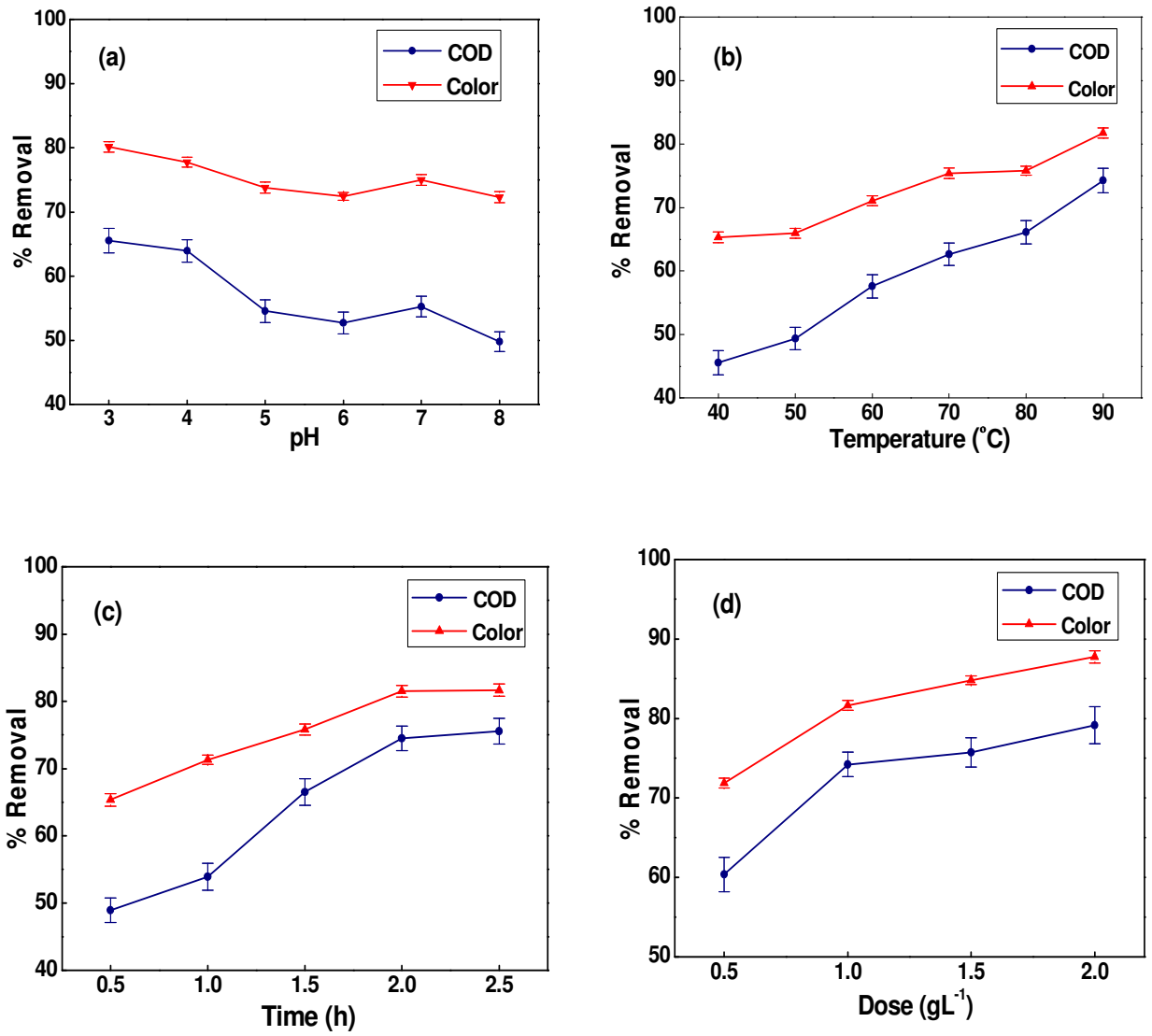

Fig.3.9. Effect of operating variables (a) *pH* (b) Temperature (c) Time (d) Dose

3.3. CWAO study over $Ce_{1-x}Fe_xO_2$ nanocatalysts

Figure 3.10 shows the percent removal of COD, color TOC and AOX as a function of Ce/Fe mole ratio. Pure CeO_2 demonstrated very low removal efficiency. The catalytic activity augmented with increasing Fe content and attained a maximum value of 74% COD, 82% color, 72% TOC and 68% AOX reduction with $Ce_{0.4}Fe_{0.6}O_2$ mixed oxide under optimum conditions (90°C, *pH* 4, 1 gL^{-1}, 2 h). High removal efficiency of $Ce_{0.4}Fe_{0.6}O_2$ mixed oxide was consistent with the above characterization results. Thus $Ce_{0.4}Fe_{0.6}O_2$ mixed oxide was selected for further study. The initial biodegradability index (BOD/COD ratio) of wastewater was low, i.e. 0.27. According to literature,

the biodegradability index should be at least 0.40 for complete biodegradation [55]. After CWAO, the biodegradability index was increased to 0.47, indicating the substantial improvement in the biodegradability of wastewater.

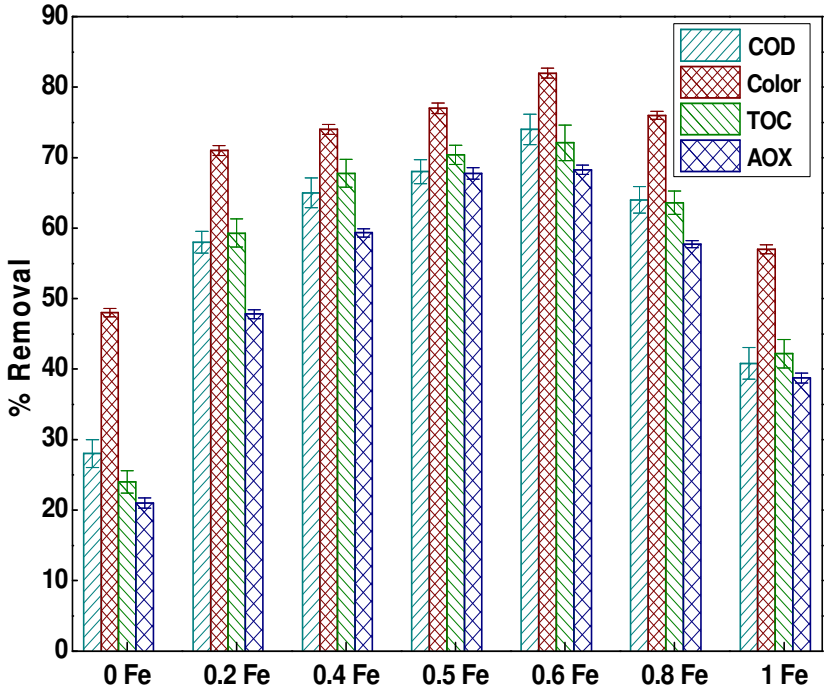

Fig.3.10. Effect of mole ratio on COD, color, TOC and AOX removal

Chlorophenolics removal

The Chlorophenolic compounds (CHPs) in wastewater were identified by GC-MS analysis. The gas chromatogram of mixtures of 25 reference CHPs (Acetyl derivatives) is shown in **Figure 3.11**. The corresponding retention time (RT) and base peak mass/charge ratio (m/z) values are listed in **Table 3.4.** These results are in accordance with the earlier findings [56,57]. **Figure 3.12** shows the gas chromatogram of CHPs in paper industry wastewater, before and after CWAO. GC-MS analysis of wastewater **(Table 3.5)**, revealed the presence of total 25 compounds falling under six categories (chemical family): chlorophenols (CP), chloroguaiacols (CG), chlorocatechols (CC), chlorovanilin (CV), chlorosyringols (CS) and chlorosyringaldehydes (CSA). The structure of CHPs by their chemical family is depicted in **Figure 3.13**, and their proportions in wastewater before CWAO are shown in **Figure 3.14 (a)**.

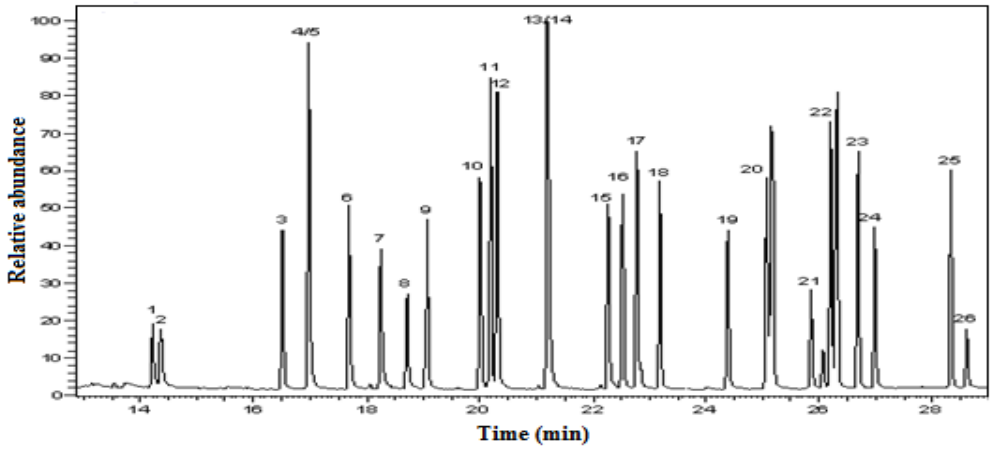

Fig.3.11. Chromatogram showing separation of a mixture of pure Chlorophenolic compounds

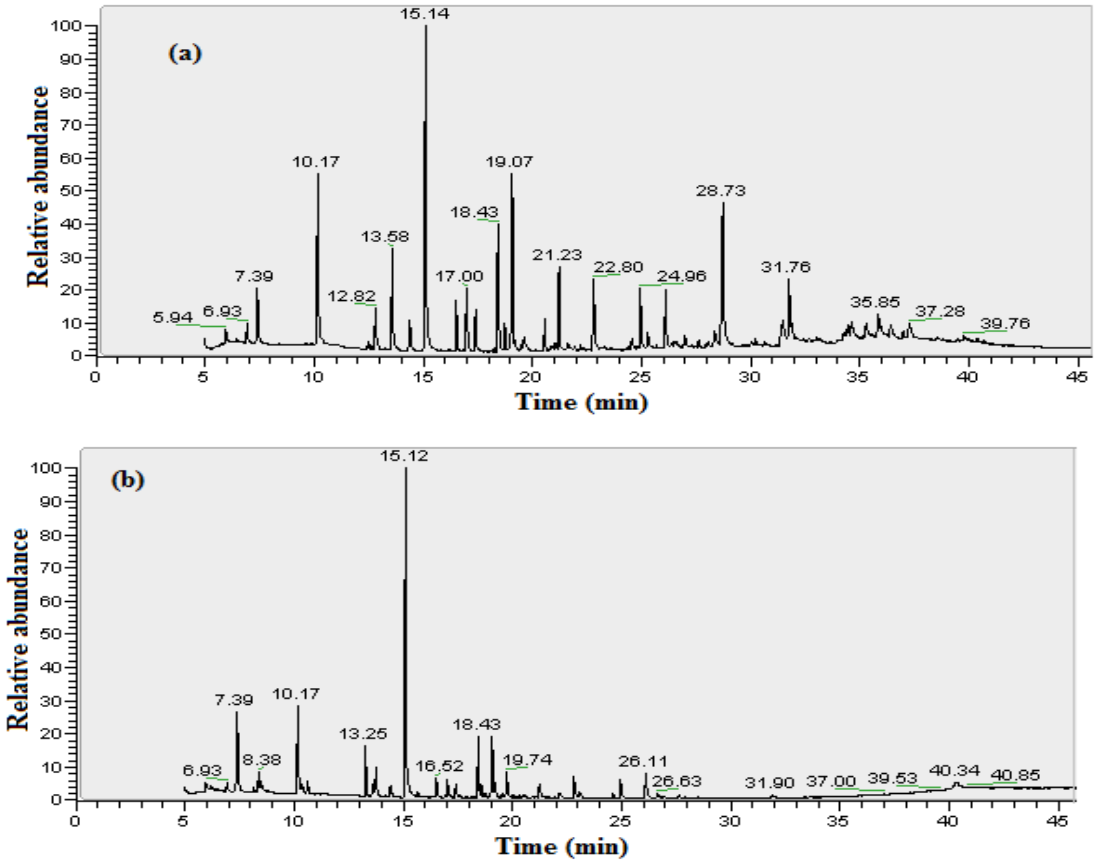

Fig.3.12. Gas chromatogram of CHPs in paper industry wastewater (a) before (b) after CWAO

Table 3.4. Retention time (RT) and m/z of Chlorophenolic reference compounds

S. No.	Compound	RT (min)	m/z
1.	3-Chlorophenol (3-CP)	14.20	127.9
2.	4-Chlorophenol (4-CP)	14.36	127.9
3.	2,6-Dichlorophenol (2,6-DCP)	16.52	161.9
4.	2,5-Dichlorophenol (2,5-DCP)	16.96	161.9
5.	2,4-Dichlorophenol (2,4-DCP)	16.98	161.8
6.	2,3-Dichlorophenol (2,3-DCP)	17.69	161.8
7.	3,4-Dichlorophenol (3,4-DCP)	18.27	161.9
8.	4-Chloroguaiacol (4-CG)	18.70	157.9
9.	2,4,5-Trichlorophenol (2,4,5-TCP)	19.07	195.8
10.	2,3,6-Trichlorophenol (2,3,6-TCP)	20.01	195.8
11.	2,3,5-Trichlorophenol (2,3,5-TCP)	20.17	195.9
12.	2,4,6-Trichlorophenol (2,4,6-TCP)	20.31	195.8
13.	4,5-Dichloroguaiacol (4,5-DCG)	21.19	191.9
14.	2,3,4-Trichlorophenol (2,3,4-TCP)	21.23	195.8
15.	4,6-Dichloroguaiacol (4,6-DCG)	22.27	191.9
16.	3,6-Dichlorocatechol (3,6-DCC)	22.50	177.9
17.	3,5-Dichlorocatechol (3,5-DCC)	22.77	177.9
18.	3,4,6-Trichloroguaiacol (3,4,6-TCG)	23.16	225.9
19.	3,4,5-Trichloroguaiacol (3,4,5-TCG)	24.40	225.8
20.	4,5,6-Trichloroguaiacol (4,5,6-TCG)	25.07	225.9
21.	5,6-Dichlorovanillin (5,6-DCV)	25.85	219.9
22.	Pentachlorophenol (PCP)	26.22	265.7
23.	2,3,5,6-Tetrachloroguaiacol (Tet-CG)	26.66	261.8
24.	Trichlorosyringol (TCS)	26.96	255.8
25.	2,6-Dichlorosyringaldehyde (2,6-DCSA)	28.59	249.9

Table 3.5. Concentration of CHPs in paper industry wastewater

S.No.	Compound	Initial Conc. (µg/L)	Final Conc. (µg/L)	% Removal
1.	3-CP	14.9 ± 10.98	7.5 ± 1.52	49.8
2.	4-CP	6.2 ± 4.55	2.5 ± 0.31	59.0
3.	2,3-DCP	0.8 ± 0.01	0.1 ± 0.10	86.9
4.	2,4-DCP	26.5 ± 0.47	10.8 ± 0.78	59.2
5.	2,5-DCP	62.4 ± 0.78	26.2 ± 1.15	57.9
6.	2,6-DCP	22.9 ± 4.45	6.3 ± 1.09	72.3
7.	3,4- DCP	0.6 ± 0.08	0.02 ± 0.03	95.9
8.	2,3,4- TCP	3.3 ± 0.10	0.4 ± 0.13	87.4
9.	2,3,5- TCP	2.5 ± 0.03	1.8 ± 0.10	26.0
10.	2,3,6- TCP	1.2 ± 0.01	0.9 ± 0.16	24.7
11.	2,4,5- TCP	132.9 ±19.7	49.5 ±1.33	62.8
12.	2,4,6- TCP	0.4 ± 0.03	0.05 ±0.02	85.7
13.	3,4,5- TCG	0.6 ± 0.11	0.4 ±0.42	33.2
14.	4-CG	83.6 ±19.45	13.3 ±1.20	84.1
15.	4,5-DCG	103 ±1.92	11.6 ±1.89	88.7
16.	4,6-DCG	2.6 ± 0.52	1.2 ±0.04	55.9
17.	3,4,6-TCG	0.5 ± 0.19	ND	100
18.	4,5,6-TCG	0.7 ± 0.10	0.1 ±0.02	81.3
19.	Tet-CG	1.8 ± 0.22	0.3 ±0.05	85.7
20.	3,5- DCC	2.9 ± 0.21	2.3 ±0.59	20.8
21.	3,6- DCC	8.5 ± 0.05	5.2 ±2.05	38.8
22.	5,6-DCV	0.3 ± 0.19	0.2 ±0.04	35.9
23.	TCS	5.9 ± 0.89	0.3 ±0.02	94.2
24.	PCP	0.4 ± 0.02	ND	100
25.	2,6-DCSA	0.1 ±0.02	0.07±0.03	21.4
	Total	**485±65.63**	**141±13.1**	**71**

*ND- Not Detected

The data exhibits highest contribution of CP (56.6%), followed by CG (39.7%), CC (2.3%), CS (1.21%), CV (0.06%) and CSA (0.02%). Based on chlorine atom substitution, di-chlorophenolics (DCHPs) exhibited highest share of 47.5%, followed by tri-chlorophenolics (TCHPs, 30.5%), mono-chlorophenolics (MCHPs, 21.6%), tetra-chlorophenolics (TeCHPs, 0.37%) and penta- chlorophenolics (PCHPs, 0.08%) **(Figure 3.14(b))**. The data indicate that about 99.5% of identified CHPs are MCHPs, DCHPs and TCHPs. Among all CHPs, 2,4,5-TCP contributed maximum share of 27.4% followed by 4,5-DCG (21.2%), 4-CG (17.2%), 2,5-DCP (12.8%), 2,4-DCP (5.5%), 2,6-DCP (4.7%) and 3-Chlorophenol (3%), while rest of CHPs are present in relatively lower quantities.

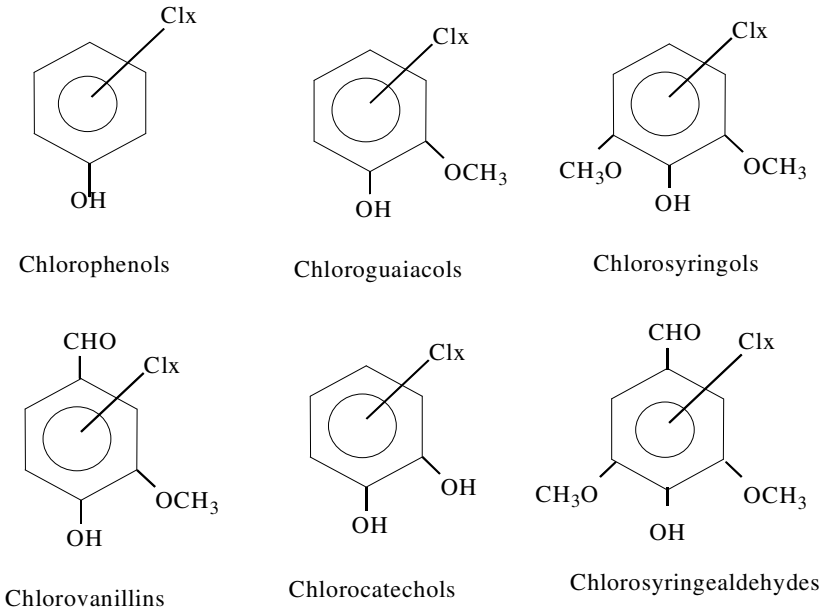

Fig.3.13. Structure of Chlorophenolic compounds

Under optimum conditions 71% of CHPs were removed in presence of $Ce_{0.4}Fe_{0.6}O_2$ mixed oxide. The removal of individual CHPs are given in **Table 3.5**. The removal of most of the compounds was from 20% to 100%. The compounds like PCP and 3,4,6-TCG were completely removed or not detected. 3,4-DCP was removed up to 95.9%, followed by TCS (94.2%), 4,5-DCG (88.7%), 2,3,4-TCP (87.4), 2,3-DCP (86.9%), 2,4,6-TCP (85.7%), 2,3,5,6-TeCG (85.7%), 4-CG (84.1%), 4,5,6-TCG (81.2) and 2,6-DCP (72.3%). The rest of the compounds were removed up to 20-63% only. 2,4,5-TCP, 2,4-DCP, 4-CP, 2,5-DCP and 4,6-DCG were removed only 62.8%, 59.2%, 59%, 57.9% and 55.9% respectively. Treatment data **(Figure 3.15(a))** revealed 61.4%, 86%, 34.2%, 36%, 94.2% and 21.4% removal of CP, CG, CC, CV, CS and CSA, respectively.

According to attached Cl atom, highest degradation was achieved for PCHPs (100%) and TeCHPs (85.7%). MCHPs, DCHPs and TCHPs were reduced by 77.7%, 72.2% and 63.8%, respectively **(Figure 3.15(b))**. The removal of high chlorinated CHPs was higher as compared to low chlorinated CHPs. This may be due to the higher negative charge on highly chlorinated CHPs, which favors their adsorption on positively charged metal ions on catalyst surface. Removal of high chlorinated CHPs by CWAO also reduces the toxicity of paper industry wastewater as these compounds are more toxic in comparison to low chlorinated CHPs [58].

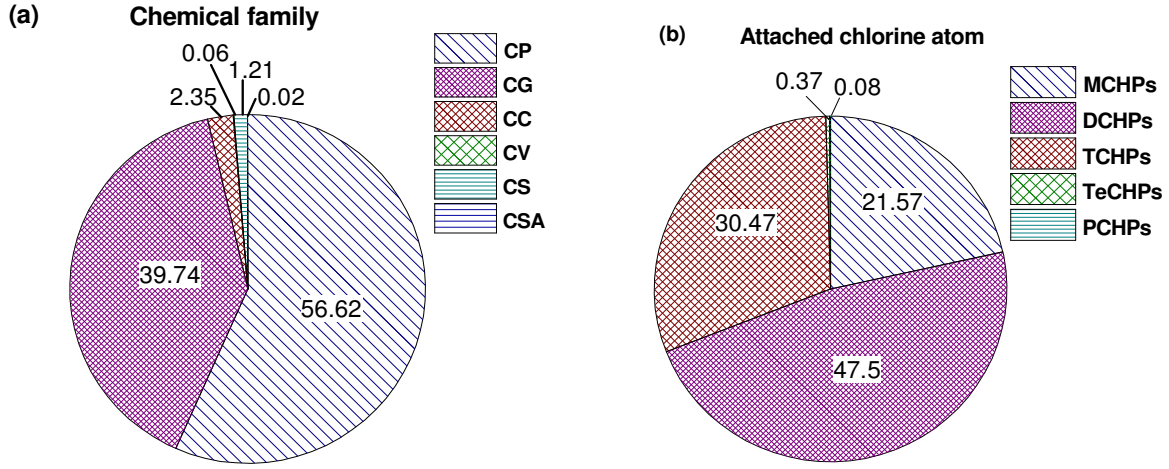

Fig.3.14. Percentage of CHPs

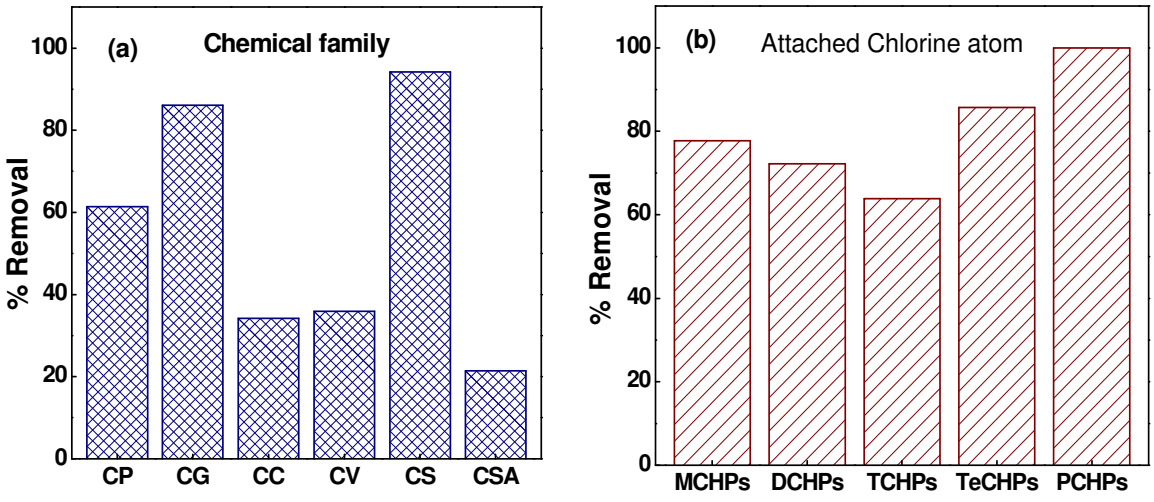

Fig.3.15. Percent removal of CHPs

3.4. Role of catalyst in oxidation

Based on the above characterization results and the mechanisms suggested in literature [59-61], it can be concluded that Ce^{4+} and Fe^{3+} in catalyst are easily reduced to Ce^{3+} and Fe^{2+}, respectively. Ce^{3+} and Fe^{2+} ions are the main active sites, where reactant molecule (R-H) gets attached. The reactant is oxidized by the interface lattice oxygen, generating oxygen vacancy at the interface; in next, the gaseous O_2 fills up the oxygen vacancy, forming adsorbed active oxygen species which can react with another reactant molecule. Guzman et al. [62] confirmed these species to be superoxide anion ($O_2^{\cdot -}$), which are formed when an electron trapped at reduced ceria surface (Ce^{3+} site) gets transferred to an adsorbed O_2 molecule. Therefore, $Ce_{1-x}Fe_xO_2$ mixed oxides can be considered as an "oxygen buffer" which responds to excess or lack of oxygen in the environment. The role of $Ce_{1-x}Fe_xO_2$ catalyst in CWAO is graphically illustrated in **Figure 3.16**.

Here are some factors, which can be related to the high efficiency of $Ce_{1-x}Fe_xO_2$ mixed oxides in CWAO at mild conditions:

1. High surface area and porosity provide high number of active sites, which facilitate the contact between reactant molecules and catalyst surface [63,64].
2. The interaction of Fe ions with CeO_2 lattice generates oxygen vacancies (confirmed by Raman and XPS). Increased oxygen vacancies directly increase the oxygen buffering capacity of catalyst.
3. Interaction of Fe cation with ceria lattice resulted in decreased particle size, which is evidenced by XRD, FE-SEM and TEM analysis. Small particles are known to increase the availability of oxygen vacancies during reaction [65].
4. $Ce_{1-x}Fe_xO_2$ mixed oxides can be interpreted in terms of bivalent catalytic centers such as (Ce^{4+}-Fe^{3+} and Ce^{3+}-Fe^{2+}) beside the one component sites (Ce^{4+}-Ce^{3+} and Fe^{3+}-Fe^{2+}). The dispersion of Fe ions can be directly related to the formation of ion pairs via following synergistic mechanism (Equation 3.4-3.6):

$$2FeO_2 \rightarrow Fe_2O_3 + O \qquad (3.4)$$

$$Fe_2O_3 + 2CeO_2 \rightarrow 2FeO_2 + Ce_2O_3 \qquad (3.5)$$

$$Ce_2O_3 + \frac{1}{1}O_2 \rightarrow 2CeO_2 \qquad (3.6)$$

The co-existence of Fe_2O_3 and FeO_2 can further increase the oxidation property of catalyst. The oxygen generated by Equation 3.4 may be more active and easy to access. Also, the oxygen transfer from CeO_2 to Fe_2O_3 may improve the oxidation reactions [66,67].

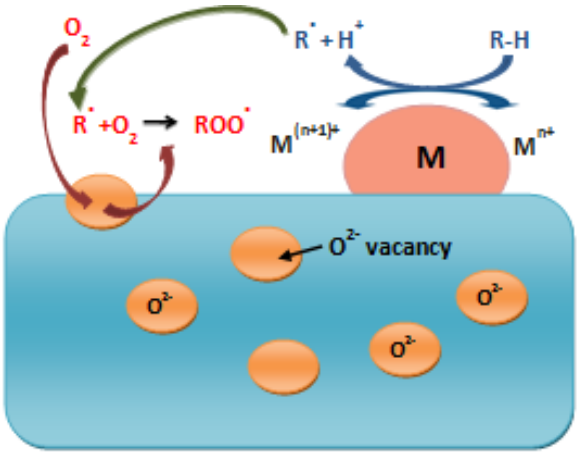

Fig.3.16. Graphical illustration for role of catalyst

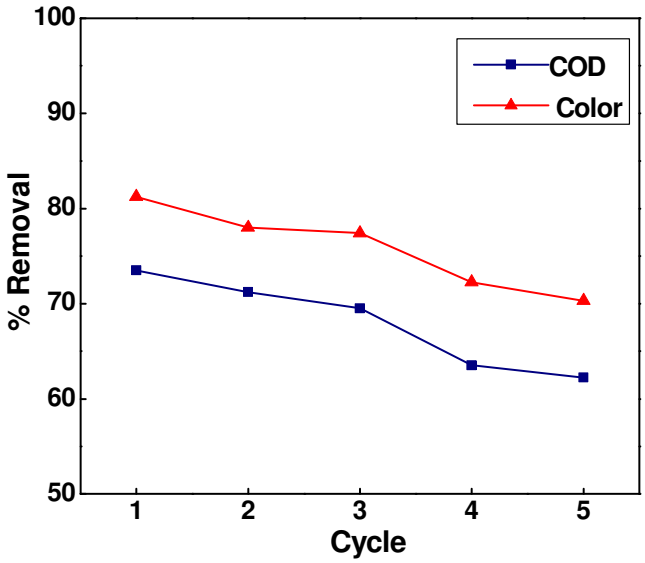

Fig.3.17. Effect of catalyst recycling on COD and color removal

3.5. Reusability and leaching studies

To test the reusability of $Ce_{0.4}Fe_{0.6}O_2$ catalyst, 5 treatment cycles were conducted with the same catalyst. The used catalyst was removed, dried and calcined before each run. After three cycles the COD removal efficiency decreased from 74 to 69%, while color removal efficiency declined from 82 to 77% and after that the removal efficiency decreased considerably (**Figure**

3.17). Results depicted that after being reused thrice, the $Ce_{0.4}Fe_{0.6}O_2$ mixed oxide still retained satisfactory activity.

The dissolved Ce and Fe concentration in treated wastewater was determined using the ICP-OES, where the most sensitive lines of Ce IV (418.6 nm) and Fe III (259.9 nm) were measured. The results showed that Ce concentrations in supernatant ranged from 0.12 to 0.132 ppm and Fe concentration ranged from 0.339-0.512 ppm. The values of metal leaching was appreciably low [68-70], indicating the stability of catalyst during treatment. This low leaching can be related to the operation of process at low temperature.

3.6. Kinetic studies

The reaction kinetics of CWAO was studied in order to understand the rate of reaction during oxidation. Paper industry wastewater contains mixture of various compounds with different reactivity. Therefore, it is quite difficult to study a detailed analysis of individual compound. To study such a complicated process, the rate of reaction can be studied in terms of a collective parameter (i.e. COD). The experimental data obtained with time-dependent COD removal in presence of $Ce_{0.4}Fe_{0.6}O_2$ catalyst was modelled on the assumption of first-order kinetics, where the progressive disappearance of COD can be presented as follows [71]:

$$-\frac{d[COD]}{dt} = k_1[COD] \qquad (3.7)$$

$$-\frac{d[COD]}{[COD]} = k_1 dt$$

By integrating both sides of equation:

$$-\int_{[COD]_o}^{[COD]} \frac{d[COD]}{[COD]} = k_1 \int_0^t dt$$

$$\ln\frac{[COD]_o}{[COD]} = k_1 t \qquad (3.8)$$

The experimental data fitted well for first order kinetics, as straight line with R^2 values of 0.99 was obtained in the plot constructed between $\ln[COD]_o/[COD]$ and time (t) **(Figure 3.18)**. Thus the CWAO of wastewater in presence of $Ce_{1-x}Fe_xO_2$ was found to follow the first order kinetics.

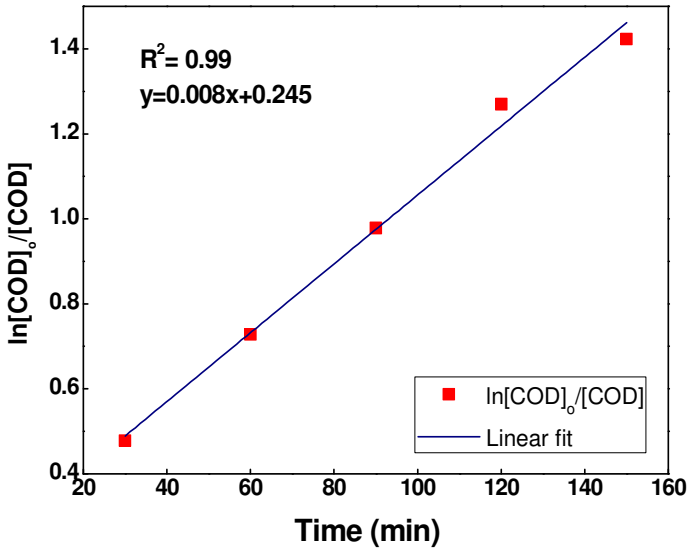

Fig.3.18. Plot of $\ln[COD]_o/[COD]$ as a function of reaction time

3.7. Summary

1. The mixed oxides exhibited improved structural, textural and catalytic property than the single metal oxides.
2. $Ce_{0.4}Fe_{0.6}O_2$ nanocatalyst presented high surface area (149 m^2g^{-1}), pore volume (0.283 ccg^{-1}) and uniform pore size distribution (3-5 nm).
3. Raman analysis confirmed the increase in oxygen vacancies with increasing Fe content.
4. XPS analysis indicated the presence of high and low oxidation states for Ce (4+, 3+) and Fe (3+, 2+) metal ions. Ce^{3+} concentration was found to be 28%.
5. The optimum conditions for CWAO were found to be: temperature 90°C, *pH* 4, catalyst dose 1 gL^{-1} and treatment time of 2 h.
6. $Ce_{0.4}Fe_{0.6}O_2$ nanocatalyst exhibited maximum COD (74%), color (82%), TOC (72%) AOX (68%) and CHPs (71%) removal under optimum experimental conditions.
7. Biodegradability index increased appreciably from 0.27 to 0.47 after treatment.
8. CWAO was found to follow the first order kinetics with R^2 values of 0.99.
9. The catalysts exhibited low leaching values for Ce (0.12 to 0.132 ppm) and Fe (0.339-0.512 ppm) metals.

References

[1] Cao, S.W. and Zhu, Y.J., 2008. Hierarchically nanostructured α-Fe_2O_3 hollow spheres: preparation, growth mechanism, photocatalytic property, and application in water treatment. *The Journal of Physical Chemistry C*, *112*(16), pp.6253-6257.

[2] Laguna, O.H., Centeno, M.A., Arzamendi, G., Gandía, L.M., Romero-Sarria, F. and Odriozola, J.A., 2010. Iron-modified ceria and Au/ceria catalysts for total and preferential oxidation of CO (TOX and PROX). *Catalysis Today*, *157*(1), pp.155-159.

[3] Zhong, D.K., Sun, J., Inumaru, H. and Gamelin, D.R., 2009. Solar water oxidation by composite catalyst/α-Fe_2O_3 photoanodes. *Journal of the American Chemical Society*, *131*(17), pp.6086-6087.

[4] Cui, Z.M., Chen, Z., Cao, C.Y., Jiang, L. and Song, W.G., 2013. A yolk–shell structured Fe_2O_3@mesoporous SiO_2 nanoreactor for enhanced activity as a Fenton catalyst in total oxidation of dyes. *Chemical Communications*, *49*(23), pp.2332-2334.

[5] Guo, S., Zhang, G., Guo, Y. and Jimmy, C.Y., 2013. Graphene oxide–Fe_2O_3 hybrid material as highly efficient heterogeneous catalyst for degradation of organic contaminants. *Carbon*, *60*, pp.437-444.

[6] Pradhan, G.K. and Parida, K.M., 2010. Fabrication of iron-cerium mixed oxide: an efficient photocatalyst for dye degradation. *International Journal of Engineering, Science and Technology*, *2*(8).

[7] Martínez, F., Melero, J.A., Botas, J.Á., Pariente, M.I. and Molina, R., 2007. Treatment of phenolic effluents by catalytic wet hydrogen peroxide oxidation over Fe_2O_3/SBA-15 extruded catalyst in a fixed-bed reactor. *Industrial & engineering chemistry research*, *46*(13), pp.4396-4405.

[8] Qiao, D., Lu, G., Liu, X., Guo, Y., Wang, Y. and Guo, Y., 2011. Preparation of $Ce_{1-x}Fe_xO_2$ solid solution and its catalytic performance for oxidation of CH_4 and CO. *Journal of materials science*, *46*(10), pp.3500-3506.

[9] Sudarsanam, P., Mallesham, B., Durgasri, D.N. and Reddy, B.M., 2014. Physicochemical characterization and catalytic CO oxidation performance of nanocrystalline Ce-Fe mixed oxides. *RSC Advances*, *4*(22), pp.11322-11330.

[10] Sirichaiprasert, K., Luengnaruemitchai, A. and Pongstabodee, S., 2007. Selective oxidation of CO to CO_2 over Cu-Ce-Fe-O composite-oxide catalyst in hydrogen feed stream. *International journal of hydrogen energy*, *32*(7), pp.915-926.

[11] Comini, E., Guidi, V., Frigeri, C., Ricco, I. and Sberveglieri, G., 2001. CO sensing properties of titanium and iron oxide nanosized thin films. *Sensors and Actuators B: Chemical*, *77*(1), pp.16-21.

[12] Li, X., Wang, Y., Liu, W., Jiang, G. and Zhu, C., 2012. Study of oxygen vacancies influence on the lattice parameter in ZnO thin film. *Materials Letters*, *85*, pp.25-28.

[13] Li, L. and Li, X., 2013. Strain-Engineered Cube Nanocrystals $Ce_{1-y}Fe_yO_2$ That Brought Forth Abnormal Structural and Magnetic Properties. *The Journal of Physical Chemistry C*, *117*(29), pp.15383-15393.

[14] Singh, P. and Hegde, M.S., 2010. Sonochemical synthesis of $Ce_{1-x}Fe_xO_{2-\delta}$ ($0 \leq x \leq 0.45$) and Ce 0.65 Fe 0.33 Pd 0.02 $O_{2-\delta}$ nanocrystallites: oxygen storage material, CO oxidation and water gas shift catalyst. *Dalton Transactions*, *39*(44), pp.10768-10780.

[15] Pérez-Alonso, F.J., López Granados, M., Ojeda, M., Terreros, P., Rojas, S., Herranz, T., Fierro, J.L.G., Gracia, M. and Gancedo, J.R., 2005. Chemical structures of coprecipitated Fe-Ce mixed oxides. *Chemistry of Materials*, *17*(9), pp.2329-2339.

[16] Li, K., Wang, H., Wei, Y. and Yan, D., 2010. Direct conversion of methane to synthesis gas using lattice oxygen of CeO_2-Fe_2O_3 complex oxides.*Chemical Engineering Journal*, *156*(3), pp.512-518.

[17] Liu, X.S., Wang, X.D., Yao, M., Cui, W. and Yan, H., 2015. Effects of Fe doping on oxygen vacancy formation and CO adsorption and oxidation at the ceria (111) surface. *Catalysis Communications*, *63*, pp.35-40.

[18] Mamontov, E., Egami, T., Brezny, R., Koranne, M. and Tyagi, S., 2000. Lattice defects and oxygen storage capacity of nanocrystalline ceria and ceria-zirconia. *The Journal of Physical Chemistry B*, *104*(47), pp.11110-11116.

[19] Dos Santos, M.L., Lima, R.C., Riccardi, C.S., Tranquilin, R.L., Bueno, P.R., Varela, J.A. and Longo, E., 2008. Preparation and characterization of ceria nanospheres by microwave-hydrothermal method. *Materials Letters*, *62*(30), pp.4509-4511.

[20] Zhao, B., Wang, Y., Guo, H., Wang, J., He, Y., Jiao, Z. and Wu, M., 2007. Iron oxide (III) nanoparticles fabricated by electron beam irradiation method. *Materials Science Poland*, *25*(4), pp.1143-1148.

[21] Harish, K.N., Naik, H.B., Kumar, P.P., Vishwanath, R. and Kumar, G.Y., 2013. Optical and photocatalytic properties of $CdFe_2O_4$ nanocatalysts: potential application in water treatment under solar light irradiation. *Arch. Appl. Sci. Res.*, *5*, pp.42-51.

[22] Lee, Y., He, G., Akey, A.J., Si, R., Flytzani-Stephanopoulos, M. and Herman, I.P., 2011. Raman analysis of mode softening in nanoparticle $CeO_{2-\delta}$ and Au-$CeO_{2-\delta}$ during CO oxidation. *Journal of the American Chemical Society*, *133*(33), pp.12952-12955.

[23] Varshney, M., Sharma, A., Kumar, R. and Verma, K.D., 2014. Structural, Optical and Morphological Properties of Different Techniques Grown CeO_2 Thin Films. *Advanced Science, Engineering and Medicine*, *6*(2), pp.208-213.

[24] Wu, Z., Li, M., Howe, J., Meyer III, H.M. and Overbury, S.H., 2010. Probing Defect Sites on CeO_2 Nanocrystals with Well-Defined Surface Planes by Raman Spectroscopy and O_2 Adsorption†. *Langmuir*, *26*(21), pp.16595-16606.

[25] Chen, L., Fleming, P., Morris, V., Holmes, J.D. and Morris, M.A., 2010. Size-related lattice parameter changes and surface defects in ceria nanocrystals. *The Journal of Physical Chemistry C*, *114*(30), pp.12909-12919.

[26] Guo, M., Lu, J., Wu, Y., Wang, Y. and Luo, M., 2011. UV and visible Raman studies of oxygen vacancies in rare-earth-doped ceria. *Langmuir*, *27*(7), pp.3872-3877.

[27] Naganuma, T. and Traversa, E., 2012. Stability of the Ce^{3+} valence state in cerium oxide nanoparticle layers. *Nanoscale*, *4*(16), pp.4950-4953.

[28] Han, J., Meeprasert, J., Maitarad, P., Namuangruk, S., Shi, L. and Zhang, D., 2016. Investigation of the Facet-Dependent Catalytic Performance of Fe_2O_3/CeO_2 for the Selective Catalytic Reduction of NO with NH_3. *The Journal of Physical Chemistry C*., *120* (3), pp 1523-1533.

[29] López, J.M., Gilbank, A.L., García, T., Solsona, B., Agouram, S. and Torrente-Murciano, L., 2015. The prevalence of surface oxygen vacancies over the mobility of bulk oxygen in

nanostructured ceria for the total toluene oxidation. *Applied Catalysis B: Environmental*, *174*, pp.403-412.

[30] Nasibulin, A.G., Rackauskas, S., Jiang, H., Tian, Y., Mudimela, P.R., Shandakov, S.D., Nasibulina, L.I., Jani, S. and Kauppinen, E.I., 2009. Simple and rapid synthesis of α-Fe_2O_3 nanowires under ambient conditions.*Nano Research*, *2*(5), pp.373-379.

[31] Reddy, A.S., Chen, C.Y., Chen, C.C., Chien, S.H., Lin, C.J., Lin, K.H., Chen, C.L. and Chang, S.C., 2010. Synthesis and characterization of Fe/CeO_2 catalysts: epoxidation of cyclohexene. *Journal of Molecular Catalysis A: Chemical*, *318*(1), pp.60-67.

[32] Shah, L.R., Wang, W., Zhu, H., Ali, B., Song, Y.Q., Zhang, H.W., Shah, S.I. and Xiao, J.Q., 2009. Role of dopant, defect, and host oxide in the observed room temperature ferromagnetism: Co-ZnO versus Co-CeO_2. *Journal of Applied Physics*, *105*(7), p.7C515.

[33] Bera, P. and Anandan, C., 2014. XRD and XPS studies of room temperature spontaneous interfacial reaction of CeO_2 thin films on Si and Si_3N_4 substrates. *RSC Advances*, *4*(108), pp.62935-62939.

[34] Renuka, N.K., Harsha, N. and Divya, T., 2015. Supercharged ceria quantum dots with exceptionally high oxygen buffer action. *RSC Advances*, *5*(49), pp.38837-38841.

[35] Zhang, F., Wang, P., Koberstein, J., Khalid, S. and Chan, S.W., 2004. Cerium oxidation state in ceria nanoparticles studied with X-ray photoelectron spectroscopy and absorption near edge spectroscopy. *Surface Science*, *563*(1), pp.74-82.

[36] Babu, S., Thanneeru, R., Inerbaev, T., Day, R., Masunov, A.E., Schulte, A. and Seal, S., 2009. Dopant-mediated oxygen vacancy tuning in ceria nanoparticles. *Nanotechnology*, *20*(8), p.085713.

[37] Nolan, M., 2011. Enhanced oxygen vacancy formation in ceria (111) and (110) surfaces doped with divalent cations. *Journal of Materials Chemistry*, *21*(25), pp.9160-9168.

[38] Yeriskin, I. and Nolan, M., 2010. Doping of ceria surfaces with lanthanum: a DFT+ U study. *Journal of Physics: Condensed Matter*, *22*(13), p.135004.

[39] Grosvenor, A.P., Kobe, B.A. and McIntyre, N.S., 2004. Examination of the oxidation of iron by oxygen using X-ray photoelectron spectroscopy and QUASES TM. *Surface science*, *565*(2), pp.151-162.

[40] Aronniemi, M., Sainio, J. and Lahtinen, J., 2005. Chemical state quantification of iron and chromium oxides using XPS: the effect of the background subtraction method. *Surface science*, *578*(1), pp.108-123.

[41] Mi, W.B., Jiang, E.Y. and Bai, H.L., 2009. Fe^{3+}/Fe^{2+} ratio controlled magnetic and electrical transport properties of polycrystalline $Fe_{3(1-\delta)}O_4$ films. *Journal of Physics D: Applied Physics*, *42*(10), p.105007.

[42] Wang, X., Jiang, Z., Zheng, B., Xie, Z. and Zheng, L., 2012. Synthesis and shape-dependent catalytic properties of CeO_2 nanocubes and truncated octahedra. *Cryst Eng Comm*, *14*(22), pp.7579-7582.

[43] Xu, J., Harmer, J., Li, G., Chapman, T., Collier, P., Longworth, S. and Tsang, S.C., 2010. Size dependent oxygen buffering capacity of ceria nanocrystals.*Chemical Communications*, *46*(11), pp.1887-1889.

[44] Kullgren, J., Hermansson, K. and Broqvist, P., 2013. Supercharged low-temperature oxygen storage capacity of ceria at the nanoscale. *The journal of physical chemistry letters*, *4*(4), pp.604-608.

[45] Thommes, M., 2010. Physical adsorption characterization of nanoporous materials. *Chemie Ingenieur Technik*, *82*(7), pp.1059-1073.

[46] Bhosale, R.R., Kumar, A., AlMomani, F. and Alxneit, I., 2016. Sol-Gel Derived CeO_2-Fe_2O_3 Nanoparticles: Synthesis, Characterization and Solar Thermochemical Application. *Ceramics International*. *42*(6), pp.6728-6737.

[47] Galvita, V.V., Poelman, H., Bliznuk, V., Detavernier, C. and Marin, G.B., 2013. CeO_2-modified Fe_2O_3 for CO_2 utilization via chemical looping.*Industrial & Engineering Chemistry Research*, *52*(25), pp.8416-8426.

[48] Liang, C., Ma, Z., Lin, H., Ding, L., Qiu, J., Frandsen, W. and Su, D., 2009. Template preparation of nanoscale $Ce_xFe_{1-x}O_2$ solid solutions and their catalytic properties for ethanol steam reforming. *Journal of Materials Chemistry*, *19*(10), pp.1417-1424.

[49] Pan, J.H., Dou, H., Xiong, Z., Xu, C., Ma, J. and Zhao, X.S., 2010. Porous photocatalysts for advanced water purifications. *Journal of Materials Chemistry*, *20*(22), pp.4512-4528.

[50] Wang, Y., Hong, C.S. and Fang, F., 1999. Effect of solution matrix on TiO_2 photocatalytic degradation of 2-chlorobiphenyl. *Environmental engineering science*, *16*(6), pp.433-440.

[51] Rodrigues, A.C., Boroski, M., Shimada, N.S., Garcia, J.C., Nozaki, J. and Hioka, N., 2008. Treatment of paper pulp and paper mill wastewater by coagulation-flocculation followed by heterogeneous photocatalysis. *Journal of Photochemistry and Photobiology A: Chemistry*, *194*(1), pp.1-10.

[52] Mohammed, W.T. and Kadim, H.A., 2007. Effect of operation conditions on Catalytic Oxidation of Phenol in Aqueous Solution. *Iraqi J. Che. Pet. Eng.*, *9*, pp.21-28.

[53] Perez, M., Torrades, F., García-Hortal, J.A., Domenech, X. and Peral, J., 1997. Removal of organic contaminants in paper pulp treatment effluents by TiO_2 photocatalyzed oxidation. *Journal of Photochemistry and Photobiology A: Chemistry*, *109*(3), pp.281-286.

[54] Catalkaya, E.C. and Kargi, F., 2008. Advanced oxidation treatment of pulp mill effluent for TOC and toxicity removals. *Journal of environmental management*, *87*(3), pp.396-404.

[55] Chamarro, E., Marco, A. and Esplugas, S., 2001. Use of Fenton reagent to improve organic chemical biodegradability. *Water research*, *35*(4), pp.1047-1051.

[56] Kringstad, K.P. and Lindström, K., 1984. Spent liquors from pulp bleaching. *Environmental science & technology*, *18*(8), pp.236A-248A.

[57] Pérez, M., Torrades, F., Peral, J., Lizama, C., Bravo, C., Casas, S., Freer, J. and Mansilla, H.D., 2001. Multivariate approach to photocatalytic degradation of a cellulose bleaching effluent. *Applied Catalysis B: Environmental*, *33*(2), pp.89-96.

[58] Parker, W.J., Farquhar, G.J. and Hall, E.R., 1993. Removal of chlorophenolics and toxicity during high-rate anaerobic treatment of segregated kraft mill bleach plant effluents. *Environmental science & technology*, *27*(9), pp.1783-1789.

[59] Qiao, B., Wang, A., Lin, J., Li, L., Su, D. and Zhang, T., 2011. Highly effective CuO/Fe $(OH)_x$ catalysts for selective oxidation of CO in H_2-rich stream. *Applied Catalysis B: Environmental*, *105*(1), pp.103-110.

[60] Gamarra, D., Belver, C., Fernández-García, M. and Martínez-Arias, A., 2007. Selective CO oxidation in excess H_2 over copper-ceria catalysts: Identification of active entities/species. *Journal of the American Chemical society*, *129*(40), pp.12064-12065.

[61] Zhang, Z., Han, D., Wei, S. and Zhang, Y., 2010. Determination of active site densities and mechanisms for soot combustion with O_2 on Fe-doped CeO_2 mixed oxides. *Journal of Catalysis*, *276*(1), pp.16-23.

[62] Guzman, J., Carrettin, S., Fierro-Gonzalez, J.C., Hao, Y., Gates, B.C. and Corma, A., 2005. CO Oxidation Catalyzed by Supported Gold: Cooperation between Gold and Nanocrystalline Rare-Earth Supports Forms Reactive Surface Superoxide and Peroxide Species. *Angewandte Chemie International Edition*, *44*(30), pp.4778-4781.

[63] Said, A.E.A.A., El-Wahab, M.M.A., Soliman, S.A. and Goda, M.N., 2014. Synthesis and Characterization of Nano CuO-NiO Mixed Oxides. *Nanoscience and Nanoengineering*, *2*(1), pp.17-28.

[64] Amin, N.H., Ali, L.I., El-Molla, S.A., Ebrahim, A.A. and Mahmoud, H.R., 2011. Effect of Fe_2O_3 precursors on physicochemical and catalytic properties of CuO/Fe_2O_3 system. *Arabian Journal of Chemistry*. DOI: 10.1016/j.arabjc.2011.07.026.

[65] Yao, X., Tang, C., Ji, Z., Dai, Y., Cao, Y., Gao, F., Dong, L. and Chen, Y., 2013. Investigation of the physicochemical properties and catalytic activities of $Ce_{0.67}M_{0.33}O_2$ ($M=Zr^{4+}$, Ti^{4+}, Sn^{4+}) solid solutions for NO removal by CO. *Catalysis Science & Technology*, *3*(3), pp.688-698.

[66] Li, G., Smith, R.L. and Inomata, H., 2001. Synthesis of Nanoscale $Ce_{1-x}Fe_xO_2$ Solid Solutions via a Low-Temperature Approach. *Journal of the American Chemical Society*, *123*(44), pp.11091-11092.

[67] Qi, G., Yang, R.T. and Chang, R., 2004. MnO_x-CeO_2 mixed oxides prepared by co-precipitation for selective catalytic reduction of NO with NH_3 at low temperatures. *Applied Catalysis B: Environmental*, *51*(2), pp.93-106.

[68] Neri, G., Pistone, A., Milone, C. and Galvagno, S., 2002. Wet air oxidation of p-coumaric acid over promoted ceria catalysts. *Applied Catalysis B: Environmental*, *38*(4), pp.321-329.

[69] Catrinescu, C., Teodosiu, C., Macoveanu, M., Miehe-Brendle, J. and Le Dred, R., 2003. Catalytic wet peroxide oxidation of phenol over Fe-exchanged pillared beidellite. *Water research*, *37*(5), pp.1154-1160.

[70] Quintanilla, A., Casas, J.A., Zazo, J.A., Mohedano, A.F. and Rodríguez, J.J., 2006. Wet air oxidation of phenol at mild conditions with a Fe/activated carbon catalyst. *Applied Catalysis B: Environmental*, *62*(1), pp.115-120.

[71] Lucas, M.S. and Peres, J.A., 2009. Removal of COD from olive mill wastewater by Fenton's reagent: Kinetic study. *Journal of hazardous materials*, *168*(2), pp.1253-1259.

Chapter 4

Co-Ce Nanocatalysts: Characterization and application in CWAO

Co_3O_4 based materials are widely studied oxidation catalysts [1,2]. A number of studies have been carried out on their environmental applications. Co_3O_4 nanorods exhibited 82% removal of phenol in microwave-enhanced catalytic degradation [3]. Co-Fe_3O_4 nanoparticles attained 97.9% degradation during CWAO of phenol [4]. Nanosized Co_3O_4/SiO_2 was found to be highly active in sulphate radical generation from oxone, during the phenol degradation [5]. Nanosized Co_3O_4-CeO_2 catalysts were efficient in CO oxidation [6]. Porous Co_3O_4 nanorods-reduced graphene oxide (PCNG) hybrid material attained 97% degradation of methylene blue through CWPO [7]. Co_3O_4 nanoparticles have also been studied as water-oxidation catalyst [8]. The mesoporous Co_3O_4-supported gold nanocatalyst (Au/meso-Co_3O_4) was found to be efficient for the oxidation of different organics, i.e., CO, benzene, toluene and o-xylene [9].

In the prospect of these oxidation applications of Co_3O_4, it was chosen for the formation of mixed oxide with CeO_2. A series of $Ce_{1-x}Co_xO_y$ mixed oxides (x = 0, 0.2, 0.4, 0.5, 0.6, 0.8, and 1) was synthesized by co-precipitation method (discussed in **Chapter 2**), and characterized by variety of techniques. Present chapter deals with the result and discussion on the structural and textural characteristics of $Ce_{1-x}Co_xO_y$ mixed oxides, followed by their activity study in CWAO of wastewater.

4.1. Characterization of $Ce_{1-x}Co_xO_y$ mixed oxides

4.1.1. XRD analysis

The XRD pattern of $Ce_{1-x}Co_xO_y$ mixed oxides are shown in **Figure 4.1(a)**. The diffraction pattern for CeO_2 was consistent with JCPDS file 81-0792, as discussed in Chapter 3. The peaks for pure cobalt oxide at 2θ = 31.2 (220), 36.8 (311), 44.8 (400), 59.3 (511), 65.2 (440) represented the cubic phase of Co_3O_4 (JCPDS 74-2120). In mixed oxides, the CeO_2 diffraction peaks were broadened and shifted to higher diffraction angle **(Figure 4.1(b))**. No diffraction peaks corresponding to cobalt oxide were observed up to $x \leq 0.5$, indicating the incorporation of Co_3O_4

within the ceria lattice. Further augmentation in Co content exhibited peaks for Co_3O_4 phase. The average crystallite size and lattice parameter calculated from the (111) diffraction of CeO_2 and

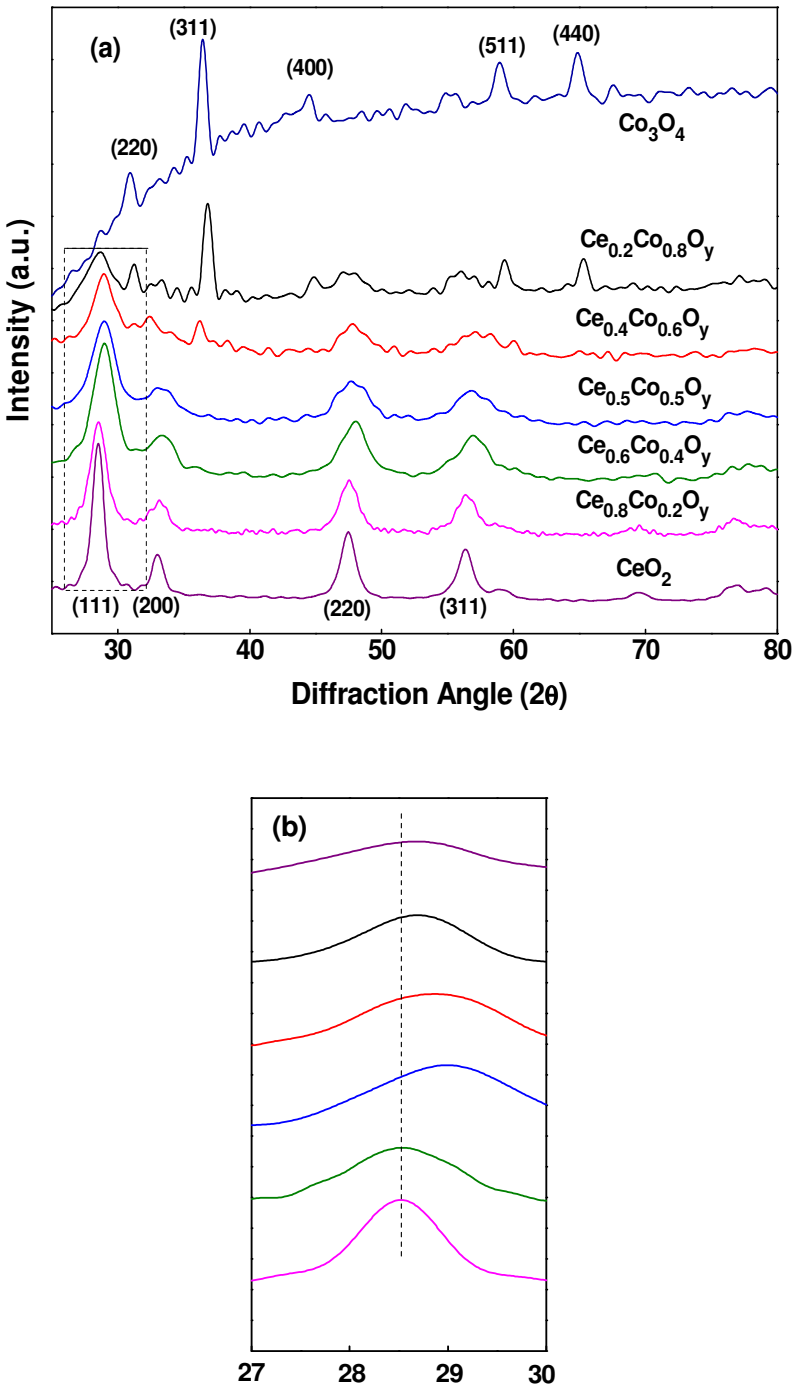

Fig.4.1. (a) XRD pattern of catalysts (b) low angle region from 27 to 30°

(311) diffraction of Co_3O_4 are reported in **Table 4.1**. Average crystallite sizes of catalysts were linearly decreased with increasing Co content. The ceria lattice parameter was also decreased with increasing Co content up to x=0.5, and then increased at x>0.5, indicating that the solid solubility of cobalt in ceria up to x=0.5. The decrease in lattice parameter was higher than the earlier studieson Co-Ce system [10-12], indicating high degree of lattice deformation.

4.1.2. FT-IR analysis

Formation of CeO_2, Co_3O_4 and $Ce_{0.5}Co_{0.5}O_y$ mixed catalysts was further verified from their FTIR spectra (**Figure 4.2**). CeO_2 exhibited the characteristic absorption band at 560 cm^{-1}. The IR spectrum of Co_3O_4 showed two distinct bands at 569 and 664 cm^{-1} assigned to Co-O stretching vibrations [13,14]. In $Ce_{0.5}Co_{0.5}O_y$ mixed catalyst the peaks for Co_3O_4 at 569 and 664 cm^{-1} were shifted to 561 and 657 cm^{-1}, respectively. This red shift indicated the increasing lattice parameter of Co_3O_4 for the $Ce_{1-x}Co_xO_y$ mixed oxides (**Table 4.1**). The decreased band intensity confirmed the interaction between CeO_2 and Co_3O_4 phases in mixed oxide.

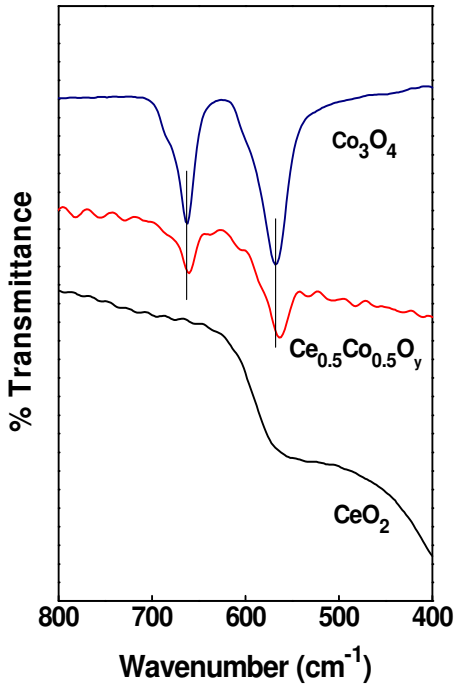

Fig.4.2. FT-IR of catalysts

4.1.3. Raman analysis

The Raman spectrum of CeO_2, Co_3O_4 and $Ce_{1-x}Co_xO_y$ catalysts are shown in **Figure 4.3**. CeO_2 exhibited the characteristic band at 462 cm^{-1}. For $Ce_{1-x}Co_xO_y$ mixed oxides, the characteristic band of intrinsic oxygen vacancies was also observed at 600 cm^{-1}. The I_{600}/I_{462} **(Figure 4.3 (b))** ratio was increased with increasing Co content, indicating the increasing amount of oxygen vacancies.

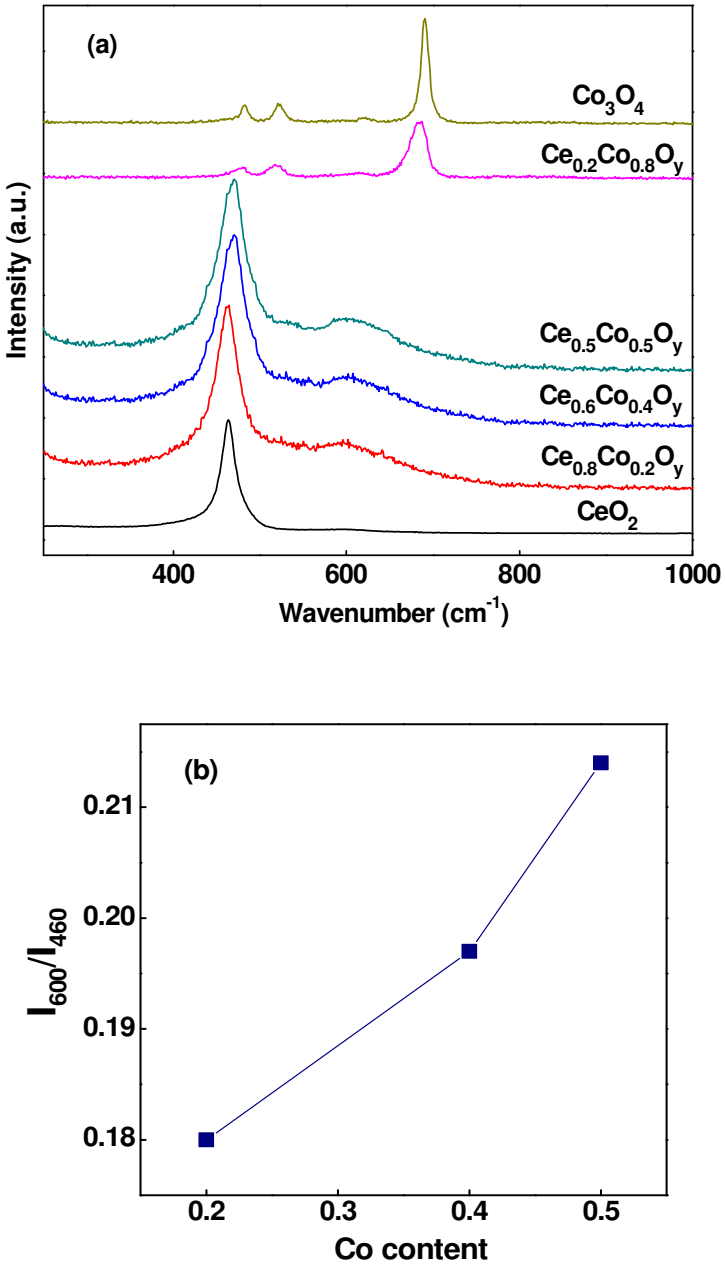

Fig.4.3. (a) Raman spectra of catalysts (b) variation of I_{600}/I_{460} with Co content

Co_3O_4 spectra showed the peaks at 483, 521, 620, and 690 cm^{-1}, corresponding to four Raman-active modes i.e., A_{1g}, E_g, and $2F_{2g}$ of Co_3O_4, caused by the lattice vibrations of the spinal structure, where Co^{2+} and Co^{3+} cations are situated at tetrahedral and octahedral sites in the cubic lattice [15,16].

$Ce_{0.2}Fe_{0.8}O_2$

4.1.4. XPS analysis

The XPS spectra of $Ce_{0.5}Co_{0.5}O_y$ mixed oxide is presented in **Figure 4.4**. Ce 3d spectra (**Figure 4.4 (a)**) exhibited three main $3d_{5/2}$ features at 881.3 eV, 888.5 eV, 897.2 eV corresponding to v, v″, v‴ components, respectively. The $3d_{3/2}$ feature corresponding to u, u″ and u‴ component were observed at 899.5 eV, 906.5 eV and 915.8 eV. These peaks are characteristic of Ce^{4+} oxidation state with the v and u splitting of 18.1 eV. Additional peaks for v^o (880.4 eV), v′ (886 eV), u^o (898.1 eV) and u′ (901.4 eV) components were also observed. These peaks are characteristic of Ce^{3+} oxidation state. The atomic fraction of Ce^{3+} was found to be 28%, which is comparable to the value reported by Konsolakis et al. [17]. **Figure 4.4(b)** shows the Co2p spectra of $Ce_{0.5}Co_{0.5}O_y$ mixed oxide. The prominent $Co2p_{3/2}$ peak was composed of two peaks at 779.4 and 780.9 eV corresponding to Co^{3+} and Co^{2+}, respectively. Also there were peaks corresponding to Co^{3+} (794.3 eV) and Co^{2+} (795.8 eV) in the $2p_{1/2}$ spin orbit component. Additionally, the weak satellite structures were found in the high binding energy side of $2p_{3/2}$ and $2p_{1/2}$ transitions at 785.4 eV and 801.6 eV. These results confirmed the formation of Co_3O_4 with Co^{3+} and Co^{2+} species [18,19]. The O 1s spectra (**Figure 4.4(c))** of $Ce_{0.5}Co_{0.5}O_y$ mixed oxide exhibited three components corresponding to lattice oxygen/ structural oxygen (528.1 eV, 70.9%), supercharged oxygen (O_2^-) near oxygen vacant sites at the surface (530.1 eV, 19.3%) and adsorbed surface oxygen in the form of OH ions (531.2 eV, 9.7%). The peak at 530.1 eV evidenced the oxygen storage/release capacity of the nanocatalyst. Thus XPS analysis confirmed the presence of oxygen vacancies accompanied with Ce^{4+} reducing to Ce^{3+} in presence of Co^{3+} and Co^{2+} ions.

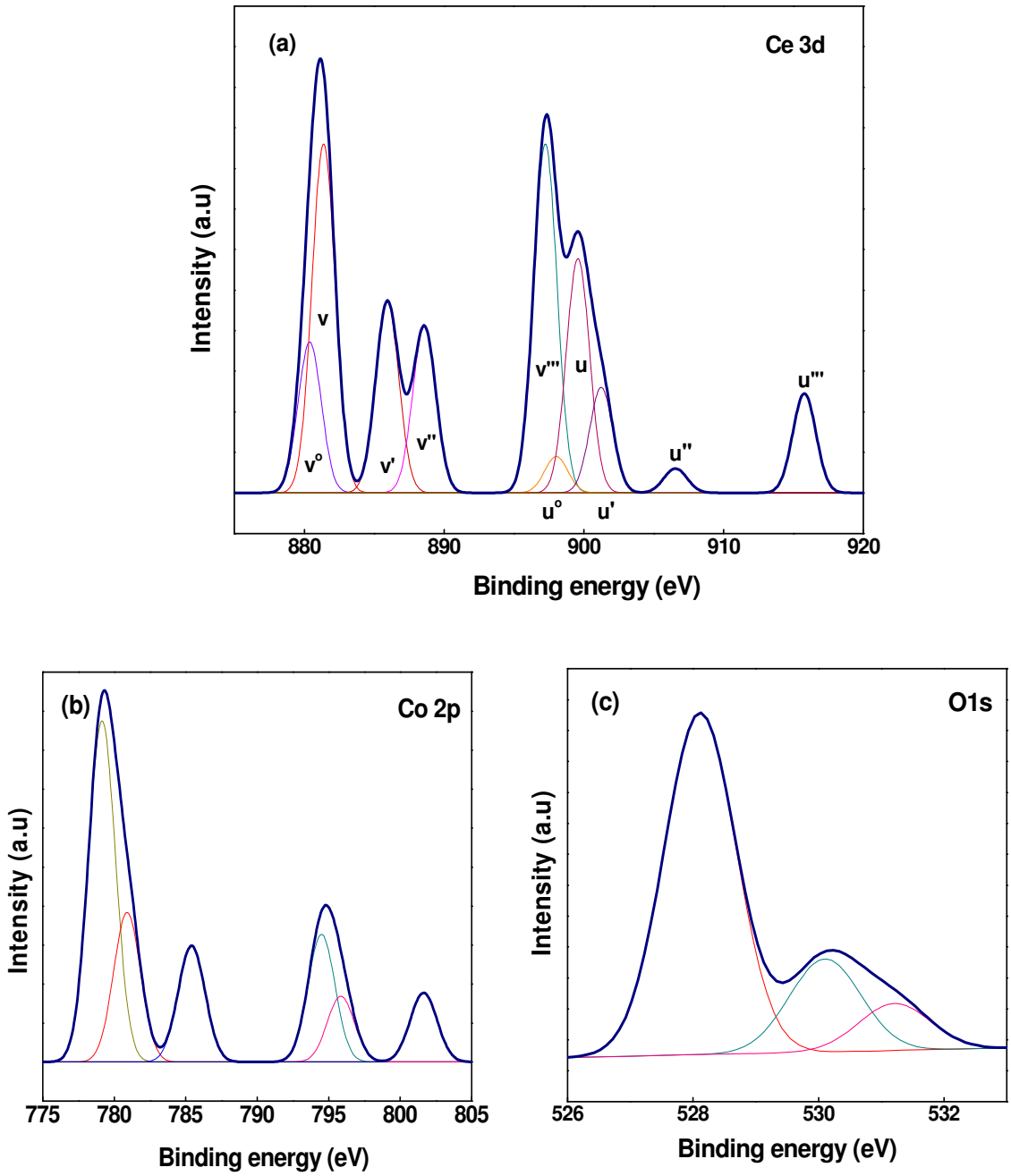

Fig.4.4. XPS spectra of $Ce_{0.5}Co_{0.5}O_y$ (a) Ce 3d (b) Co 2p (c) O 1s

4.1.5. N_2-adsorption/desorption analysis

The N_2-adsorption/desorption isotherm and pore size distribution of CeO_2, $Ce_{0.5}Co_{0.5}O_y$ and Co_3O_4 catalysts are presented in **Figure 4.5(a)**. For adsorption isotherms the inflection at higher relative pressure indicated the presence of secondary pores. The desorption isotherm resulted in a

narrow hysteresis, indicating the irregular shape of pores. PSD **(Figure 4.5(b))** confirmed the presence of disordered and wide pores for CeO_2 and Co_3O_4 catalysts (3-15 nm). While, $Ce_{0.5}Co_{0.5}O_y$ was found to have the narrow pores (3-8 nm).

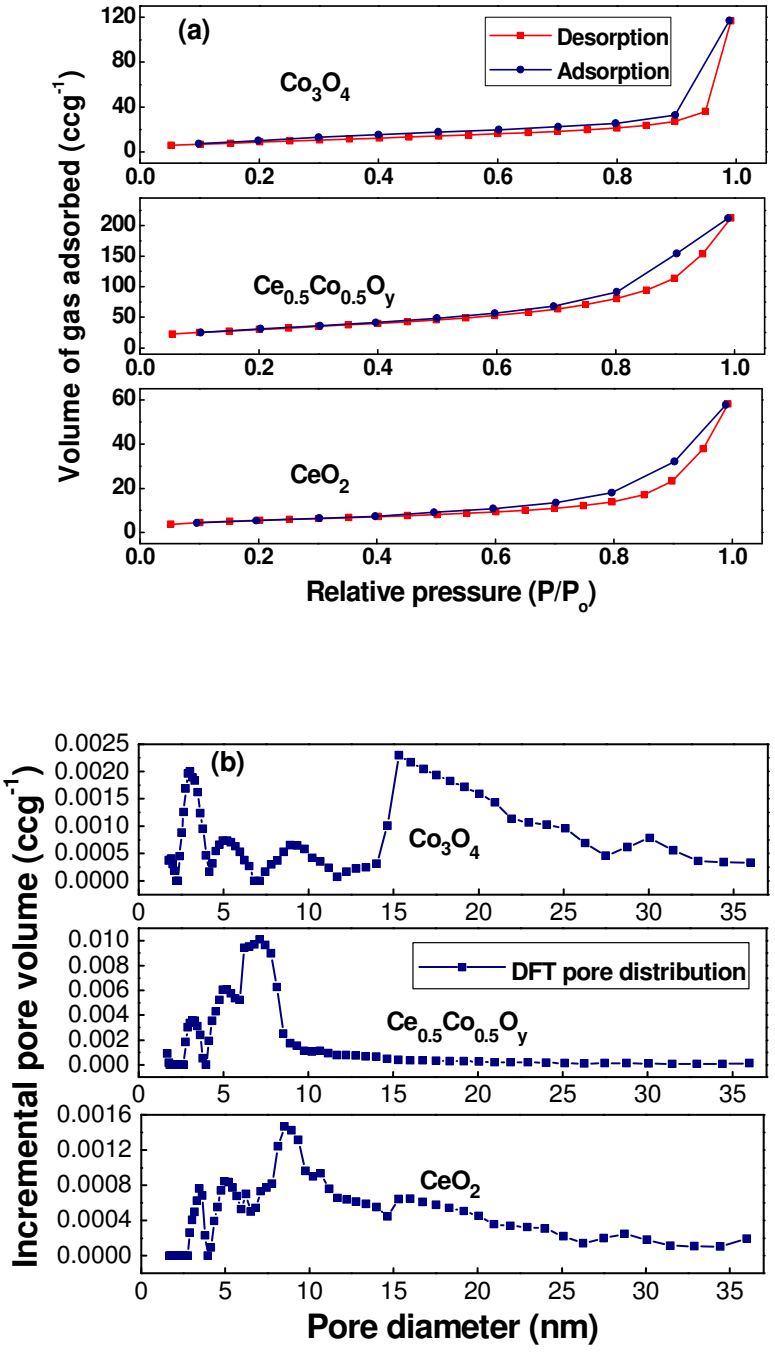

Fig.4.5. (a) N_2-adsorption/desorption isotherms (b) Pore size distribution

Table.4.1. Structural and textural parameters of $Ce_{1-x}Co_xO_y$ nano-catalysts

Samples	Crystallite size (nm)[a]		Lattice parameter (Å)[a]		Average particle size (nm)[b]	Specific surface area (m^2g^{-1})[c]	Total pore volume (ccg^{-1})[c]
	CeO_2	Co_3O_4	CeO_2	Co_3O_4			
CeO_2	10.6	--	5.416	--	45 ± 1.4	20	0.089
$Ce_{0.8}Co_{0.2}O_y$	8.55	--	5.399	--	39.5 ± 3.5	92	0.233
$Ce_{0.6}Co_{0.4}O_y$	6.15	--	5.324	--	25 ± 1.4	100	0.248
$Ce_{0.5}Co_{0.5}O_y$	4.74	--	5.314	---	22.5 ± 1.1	109	0.416
$Ce_{0.4}Co_{0.6}O_y$	4.59	10.75	5.347	8.220	16.5 ± 0.7	99	0.390
$Ce_{0.2}Co_{0.8}O_y$	3.63	10.3	5.368	8.089	15.5 ± 2.1	70	0.328
Co_3O_4	--	9.8	--	8.090	18 ± 1.4	34	0.181

[a] Calculated from XRD; [b] FE-SEM; [c] N_2-adsorption/desorption

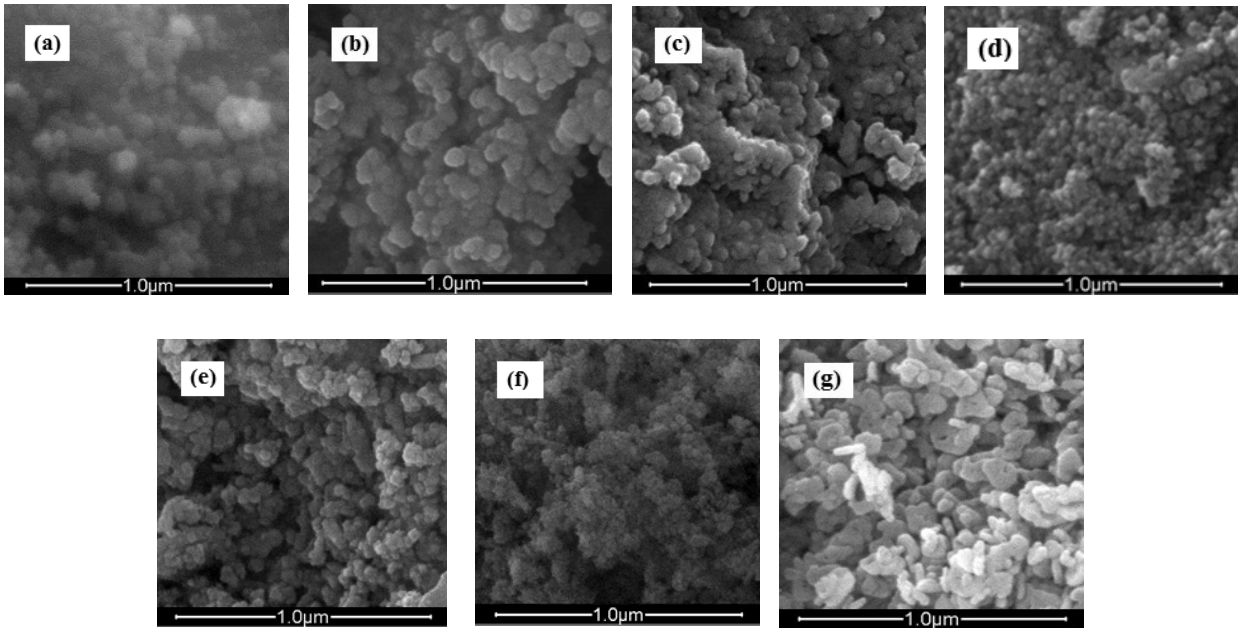

Fig.4.6. FE-SEM micrograph of (a) CeO_2 (b) $Ce_{0.8}Co_{0.2}O_y$ (c) $Ce_{0.6}Co_{0.4}O_y$ (d) $Ce_{0.5}Co_{0.5}O_y$ (e) $Ce_{0.4}Co_{0.6}O_y$ (f) $Ce_{0.2}Co_{0.8}O_y$ (g) Co_3O_4

The textural properties of catalysts are listed in **Table 4.1**. The data indicated that the $Ce_{1-x}Co_xO_y$ catalysts presented high BET surface area of 70-109 $m^2\ g^{-1}$ and pore volume of 0.233-0.416 cc g^{-1}, than that of single metal oxides (CeO_2 and Co_3O_4). The lower value of surface area and pore volume for x>0.5 can be related to the formation of more agglomerates (indicated by FE-SEM

analysis). The surface area and pore volume of $Ce_{1-x}Co_xO_y$ catalysts were significantly higher than the previous reports, where samples were fabricated by sol-gel [10], hydrothermal [12], impregnation [17] and thermal combustion method [20].

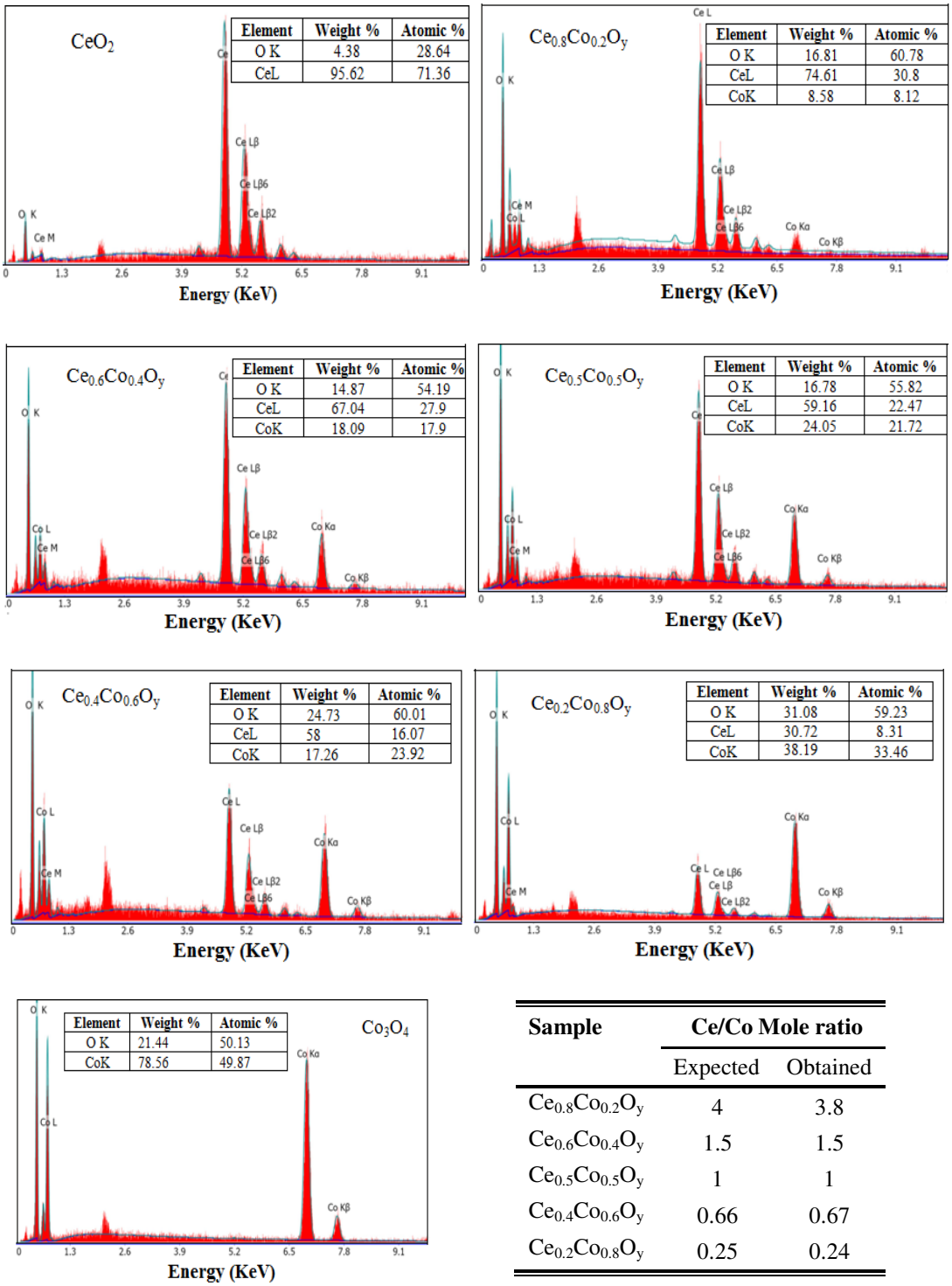

Fig.4.7. EDX spectra of catalysts

Sample	Ce/Co Mole ratio	
	Expected	Obtained
$Ce_{0.8}Co_{0.2}O_y$	4	3.8
$Ce_{0.6}Co_{0.4}O_y$	1.5	1.5
$Ce_{0.5}Co_{0.5}O_y$	1	1
$Ce_{0.4}Co_{0.6}O_y$	0.66	0.67
$Ce_{0.2}Co_{0.8}O_y$	0.25	0.24

Table 4.2. Ce/Co mole ratio from EDX

4.1.6. FE-SEM and TEM analysis

Figure 4.6(a-g) shows the SEM micrographs of $Ce_{1-x}Co_xO_y$ mixed oxides and correspondingly their particle size ranges are mentioned in **Table 4.1**. As depicted in table, average particle size of CeO_2 was 45±1.4 nm which decreased to 39.5±3.5 nm for x=0.2, further increase in Co content resulted in considerable decrease in average particle size. These results were in good agreement with XRD analysis. Micrographs clearly illustrated the high agglomeration of particles for x>0.5. EDX spectra of mixed oxides are presented in **Figure 4.7**, and the expected as well as obtained values of Ce/Co mole ratio are provided in **Table 4.2**. EDX analysis confirmed that the obtained mole ratio values were close to the expected values, confirming the presence of Ce and Co with required mole ratio. The TEM micrographs of CeO_2, $Ce_{0.5}Co_{0.5}O_y$ and Co_3O_4 catalysts are presented in **Figure 4.8**. The presence of disordered pores was further confirmed by TEM micrographs. Statistical analysis of micrographs illustrated that the mean diameter of CeO_2, $Ce_{0.5}Co_{0.5}O_y$ and Co_3O_4 was 16, 5 and 7 nm, respectively. The diffraction rings in SAED pattern of $Ce_{0.5}Co_{0.5}O_y$ were attributable to (111), (311) planes of CeO_2 and (220), (311), (400) planes of Co_3O_4, indicating its polycrystalline nature.

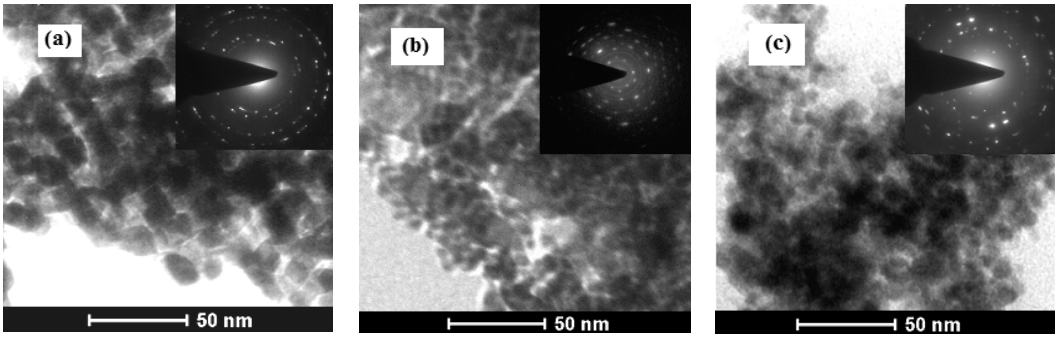

Fig.4.8. TEM micrograph and SAED pattern of (a) CeO_2 (b) $Ce_{0.5}Co_{0.5}O_y$ (c) Co_3O_4

4.2. CWAO study over $Ce_{1-x}Co_xO_y$ nanocatalysts

The treatment efficiency of $Ce_{1-x}Co_xO_y$ catalysts in terms of COD, color, AOX and TOC removal is presented in **Figure 4.9**. Results indicated the high efficiency of $Ce_{1-x}Co_xO_y$ mixed oxides in comparison to single oxides. The $Ce_{0.5}Co_{0.5}O_y$ catalyst was found to be most active with 68% COD, 79% color, 59% AOX and 66% TOC removal. Additionally, the biodegradability index of wastewater was enhanced up to 0.45, indicating the appreciable removal of non-biodegradable component.

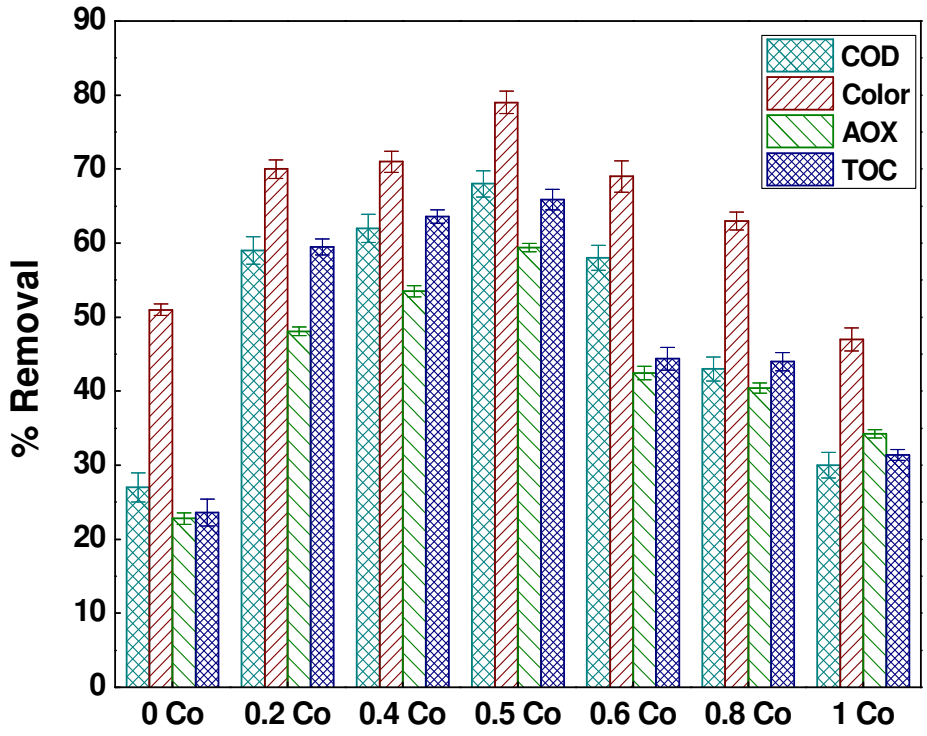

Fig.4.9. Effect of mole ratio on COD, color, AOX and TOC removal

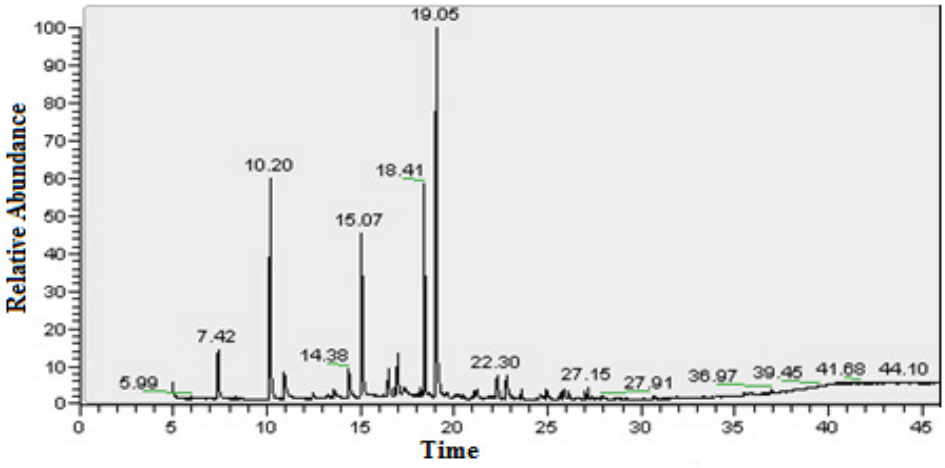

Fig. 4.10. GC chromatogram of CHPs after CWAO

Chlorophenolics removal

CWAO in presence of $Ce_{0.5}Co_{0.5}O_y$ catalyst resulted in 62% removal of CHPs. GC chromatogram of CHPs after treatment is shown in **Figure 4.10**, and the removal of individual CHPs are listed in **Table 4.3**. The removal of CHPs was from 28% to 100%. The compounds like PCP, 3,4-DCP, 2,4,6-TCP and 2,6-DCSA were completely removed or not detected. 3,4,5-TCGU was removed up to 95.8%, followed by 4,5-DCG (95.6%), TCS (93%), 2,3-DCP (90.3), 4-CG (89.6%), 2,3,6-TCP (87.9%), 2,3,5-TCP (86.5%), 2,3,5,6-TeCG (81.9%), 4,5,6-TCG (72.8%), 3,4,6-TCG (70.3%), 2,6-DCP (65.9%) and 2,3,4-TCP (65.1%). The rest of the compounds were removed up to 28-59%. The removal of CP, CG, CC, CV, CS and CSA was 40.9%, 92.1%, 52.6%, 28.7%, 92.99% and 100%, respectively **(Figure 4.11(a))**. The removal of PCHPs was highest (100%) followed by TeCHPs (81.8%), MCHPs (79.9%), DCHPs (72.2%) and TCHPs (33.7%) **(Figure 4.11(b))**.

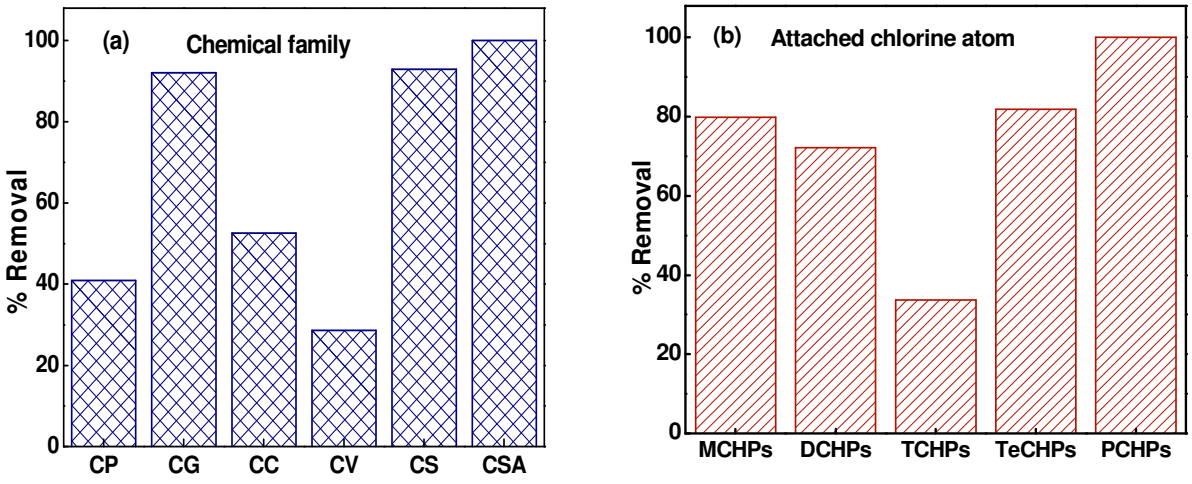

Fig.4.11. Percent removal of CHPs

Table 4.3. Concentration of CHPs with percent removal

S.No	Name of compound	Initial (µg/L)	Final (µg/L)	% Removal
1.	3-CP	14.93 ± 10.91	9.09 ± 1.01	39.1
2.	4-CP	6.16 ± 4.55	3.31 ± 0.14	46.3
3.	2,3-DCP	0.81 ± 0.01	0.08 ± 0.01	90.3
4.	2,4-DCP	26.54 ± 0.47	13.59 ± 1.13	48.8
5.	2,5-DCP	62.41 ± 0.78	31.21 ± 2.02	49.9
6.	2,6-DCP	22.92 ± 4.45	7.8 ± 1.16	65.9
7.	3,4-DCP	0.56 ± 0.08	ND	100
8.	2,3,4-TCP	3.31 ± 0.10	1.15 ± 0.07	65.1
9.	2,3,5-TCP	2.45 ± 0.03	0.33 ± 0.04	86.5
10.	2,3,6-TCP	1.15 ± 0.01	0.14 ± 0.07	87.9
11.	2,4,5-TCP	132.87 ± 19.69	95.7 ± 2.1	28.0
12.	2,4,6-TCP	0.36 ± 0.03	ND	100
13.	PCP	0.40 ± 0.02	ND	100
14.	4-CG	83.64 ± 19.45	8.69 ± 0.31	89.6
15.	4,5-DCG	102.98 ± 1.92	4.49 ± 0.13	95.6
16.	4,6-DCG	2.6 ± 0.52	1.35 ± 0.16	48.1
17.	3,4,5-TCG	0.64 ± 0.11	0.03 ± 0.05	95.8
18.	3,4,6-TCG	0.53 ± 0.19	0.16 ± 0.01	70.3
19.	4,5,6-TCG	0.71 ± 0.10	0.19 ± 0.02	72.8
20.	2,3,5,6-TeCG	1.81 ± 0.22	0.33 ± 0.07	81.9
21.	3,5-DCC	2.93 ± 0.21	1.92 ± 0. 08	34.5
22.	3,6-DCC	8.47 ± 0.05	3.48 ±0.13	58.9
23.	5,6-DCV	0.28 ± 0.19	0.20 ± 0.01	28.7
24.	TCS	5.87 ± 0.89	0.41 ± 0.05	93.0
25.	2,6-DCSA	0.09 ± 0.02	ND	100
	Total	**485**	**183.6**	**62.3%**

*ND- Not Detected

4.3. Reusability and leaching studies

The reusability experiments of $Ce_{0.5}Co_{0.5}O_y$ mixed oxide (calcined) were carried out up to 5 treatment cycles. After being reused thrice, the $Ce_{0.5}Co_{0.5}O_y$ mixed oxide still retained satisfactory activity, with 63% COD and 74% color removal **(Figure 4.12)**. The dissolved concentration of Ce IV (418.6 nm) in treated wastewater ranged from 0.121 to 0.126 ppm and Co II (228.6 nm) concentration ranged from 0.346-0.595 ppm. The metal leaching values were low [21], indicating the negligible leaching.

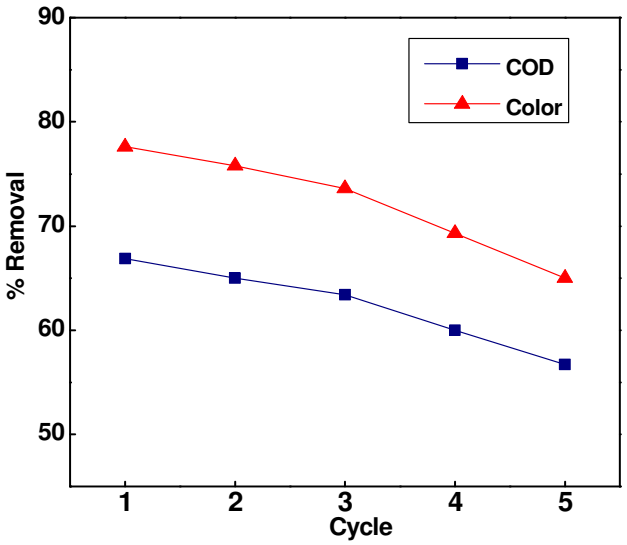

Fig.4.12. Effect of catalyst recycling on COD and color removal

4.4. Kinetic studies

The kinetic study on time-dependent COD removal indicated the first order kinetics as straight line with R^2 values of 0.952 was obtained in the plot constructed between $\ln[COD]_o/[COD]$ on x-axis versus time (t) on y-axis (**Figure 4.13**).

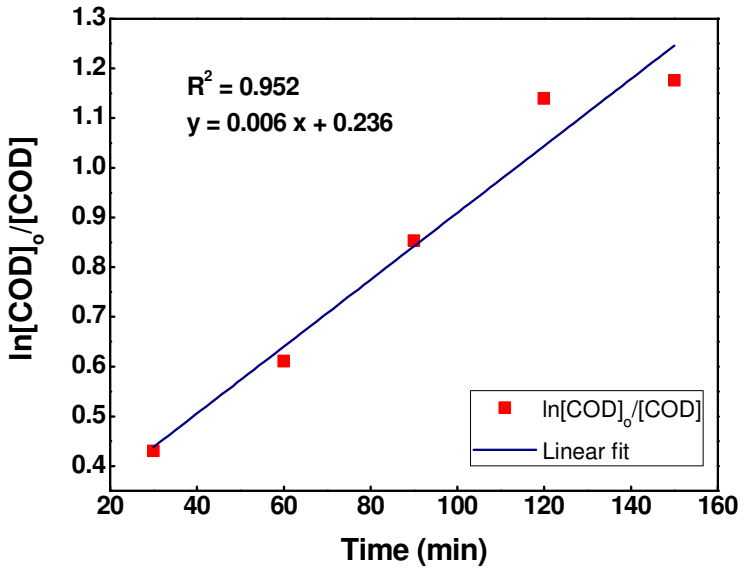

Fig.4.13. Linear fitting of $\ln[COD]_o/[COD]$ as a function of reaction time

4.5. Summary

1. The $Ce_{1-x}Co_xO_y$ mixed oxides exhibited improved structural, textural and catalytic property than the single metal oxides.
2. $Ce_{0.5}Co_{0.5}O_y$ presented high surface area (109 m^2g^{-1}) and pore volume (0.416 ccg^{-1}). The pore size was found to be 3-8 nm.
3. Raman analysis confirmed the presence of O-vacancies in mixed oxides.
4. XPS analysis indicated the presence of high and low oxidation states for Ce (4+, 3+) and Co (3+, 2+) metal ions. Ce^{3+} concentration was found to be 28%
5. $Ce_{0.5}Co_{0.5}O_y$ exhibited maximum COD (68%), color (79%), TOC (66%), AOX (59%) and CHPs (62%) removal.
6. Biodegradability index increased from 0.27 to 0.45.
7. The first order kinetics was ascertained with R^2 values of 0.952.
8. The low leaching values of Ce (0.121 to 0.126 ppm) and Co (0.346-0.595 ppm) metals was obtained.

References

[1] Alvarez, A., Ivanova, S., Centeno, M.A. and Odriozola, J.A., 2012. Sub-ambient CO oxidation over mesoporous Co_3O_4: Effect of morphology on its reduction behavior and catalytic performance. *Applied Catalysis A: General*, *431*, pp.9-17.

[2] Ma, C.Y., Mu, Z., Li, J.J., Jin, Y.G., Cheng, J., Lu, G.Q., Hao, Z.P. and Qiao, S.Z., 2010. Mesoporous Co_3O_4 and Au/Co_3O_4 catalysts for low-temperature oxidation of trace ethylene. *Journal of the American Chemical Society*, *132*(8), pp.2608-2613.

[3] Lai, T.L., Lai, Y.L., Lee, C.C., Shu, Y.Y. and Wang, C.B., 2008. Microwave-assisted rapid fabrication of Co_3O_4 nanorods and application to the degradation of phenol. *Catalysis Today*, *131*(1), pp.105-110.

[4] Song, X.C., Zheng, Y.F. and Yin, H.Y., 2013. Catalytic wet air oxidation of phenol over Co-doped Fe_3O_4 nanoparticles. *Journal of nanoparticle research*, *15*(8), pp.1-9.

[5] Shukla, P., Sun, H., Wang, S., Ang, H.M. and Tadé, M.O., 2011. Nanosized Co_3O_4/SiO_2 for heterogeneous oxidation of phenolic contaminants in waste water. *Separation and Purification Technology*, *77*(2), pp.230-236.

[6] Luo, J.Y., Meng, M., Li, X., Li, X.G., Zha, Y.Q., Hu, T.D., Xie, Y.N. and Zhang, J., 2008. Mesoporous Co_3O_4-CeO_2 and Pd/Co_3O_4-CeO_2 catalysts: synthesis, characterization and mechanistic study of their catalytic properties for low-temperature CO oxidation. *Journal of Catalysis*,*254*(2), pp.310-324.

[7] Zhang, Z., Hao, J., Yang, W., Lu, B., Ke, X., Zhang, B. and Tang, J., 2013. Porous Co_3O_4 nanorods-reduced graphene oxide with intrinsic peroxidase-like activity and catalysis in the degradation of methylene blue. *ACS applied materials & interfaces*, *5*(9), pp.3809-3815.

[8] Blakemore, J.D., Gray, H.B., Winkler, J.R. and Müller, A.M., 2013. Co_3O_4 nanoparticle water-oxidation catalysts made by pulsed-laser ablation in liquids. *ACS Catalysis*, *3*(11), pp.2497-2500.

[9] Liu, Y., Dai, H., Deng, J., Xie, S., Yang, H., Tan, W., Han, W., Jiang, Y. and Guo, G., 2014. Mesoporous Co_3O_4-supported gold nanocatalysts: Highly active for the oxidation of carbon monoxide, benzene, toluene, and o-xylene. *Journal of Catalysis*, *309*, pp.408-418.

[10] Li, H., Lu, G., Qiao, D., Wang, Y., Guo, Y. and Guo, Y., 2011. Catalytic Methane Combustion over Co_3O_4/CeO_2 Composite Oxides Prepared by Modified Citrate Sol-Gel Method. *Catalysis letters*, *141*(3), pp.452-458.

[11] Liu, B., Liu, Y., Hou, H., Liu, Y., Wang, Q. and Zhang, J., 2015. Variation of redox activity and synergistic effect for improving the preferential oxidation of CO in H_2-rich gases in porous Pt/CeO_2-Co_3O_4 catalysts. *Catalysis Science & Technology*, *5*(12), pp.5139-5152.

[12] Varshney, M., Sharma, A., Verma, K.D. and Kumar, R., 2012. Structural and magnetic properties of $Ce_{1-x}Co_xO_2$ ($0 \leqslant x \leqslant 0.1$) nanocrystalline powders.*Physica Scripta*, *86*(1), p.015605.

[13] Xu, J., Gao, P. and Zhao, T.S., 2012. Non-precious Co_3O_4 nano-rod electrocatalyst for oxygen reduction reaction in anion-exchange membrane fuel cells. *Energy & Environmental Science*, *5*(1), pp.5333-5339.

[14] Farhadi, S., Safabakhsh, J. and Zaringhadam, P., 2013. Synthesis, characterization, and investigation of optical and magnetic properties of cobalt oxide (Co_3O_4) nanoparticles. *Journal of Nanostructure in Chemistry*, *3*(1), pp.1-9.

[15] Hadjiev, V.G., Iliev, M.N. and Vergilov, I.V., 1988. The Raman spectra of Co_3O_4. *Journal of Physics C: Solid State Physics*, *21*(7), p.L199.

[16] Pal, J. and Chauhan, P., 2010. Study of physical properties of cobalt oxide (Co_3O_4) nanocrystals. *Materials characterization*, *61*(5), pp.575-579.

[17] Konsolakis, M., Sgourakis, M. and Carabineiro, S.A., 2015. Surface and redox properties of cobalt-ceria binary oxides: On the effect of Co content and pretreatment conditions. *Applied Surface Science*, *341*, pp.48-54.

[18] Wang, X., Chen, X., Gao, L., Zheng, H., Zhang, Z. and Qian, Y., 2004. One-dimensional arrays of Co_3O_4 nanoparticles: synthesis, characterization, and optical and electrochemical properties. *The Journal of Physical Chemistry B*, *108*(42), pp.16401-16404.

[19] Tiwari, A., Bhosle, V.M., Ramachandran, S., Sudhakar, N., Narayan, J., Budak, S. and Gupta, A., 2006. Ferromagnetism in Co doped CeO2: Observation of a giant magnetic moment with a high Curie temperature.*Applied Physics Letters*, *88*(14), pp.142511-142511.

[20] Yan, C.F., Chen, H., Hu, R.R., Huang, S., Luo, W., Guo, C., Li, M. and Li, W., 2014. Synthesis of mesoporous Co-Ce oxides catalysts by glycine-nitrate combustion approach for

CO preferential oxidation reaction in excess H_2. *International Journal of Hydrogen Energy*, *39*(32), pp.18695-18701.

[21] Gruttadauria, M., Liotta, L.F., Di Carlo, G., Pantaleo, G., Deganello, G., Meo, P.L., Aprile, C. and Noto, R., 2007. Oxidative degradation properties of Co-based catalysts in the presence of ozone. *Applied Catalysis B: Environmental*, *75*(3), pp.281-289.

Chapter 5

Cu-Ce Nanocatalysts: Characterization and application in CWAO

CuO have been reported to exhibit appreciable activity in various oxidation processes [1,2]. Various studies indicated the environmental applications of CuO based materials. CuO/Al_2O_3 catalyst achieved 93% degradation of p-nitrophenol in microwave assisted Fenton-like process [3]. $CuO\text{-}MoO_3\text{-}P_2O_5$ catalyst attained 99.65% degradation of methylene blue and 55% degradation of methyl orange during CWAO [4]. The petals like CuO nanostructures achieved 95% and 85% removal of methylene blue in presence of H_2O_2 [5]. $CuMn_2O_4$ catalyst achieved 95% conversion of CO to CO_2 at 200°C [6]. $Cu_{0.1}Ce_{0.9}O_{2-y}$ catalyst exhibited 100% CO conversion at 155 °C [7].

Based on these oxidation applications of CuO based materials, CuO was chosen for the formation of mixed oxide with CeO_2. The $CuO\text{-}CeO_2$ nano-catalysts (0, 20, 40, 50, 60, 80, 100 at% Cu) were prepared by co-precipitation route (discussed in **Chapter 2**) and characterized by various techniques. This chapter describes the characterization results of $CuO\text{-}CeO_2$ mixed oxides, followed by their activity study towards CWAO of wastewater.

5.1. Characterization of $CuO\text{-}CeO_2$ mixed oxides

5.1.1. XRD analysis

XRD patterns of $CuO\text{-}CeO_2$ catalysts are presented in **Figure 5.1 (a)**. The diffraction pattern for CeO_2 was consistent with JCPDS file 81-0792, as discussed in **Chapter 3**. CuO exhibited the diffractions at 2θ= 35.4° (002), 38.7° (111), 48.8° ($\bar{2}02$), 58.1° (202), 61.5° ($\bar{1}13$), 66.3° ($\bar{3}11$) and 68.1° (220) (JCPDS file, 80-0076). There were no diffraction peaks corresponding to CuO with Cu content upto 20 at %, suggesting the incorporation of CuO within the ceria lattice. For $CuO\text{-}CeO_2$ mixed catalysts, the CeO_2 diffractions were broadened **(Figure 5.1(b))**, demonstrating the decreased crystallite size than pure CeO_2. The crystallite sizes and lattice parameters are listed in **Table 5.1**. As expected the crystallite size of CeO_2 was smaller in mixed phases, while there was no significant change in the crystallite size of CuO, indicating the formation of CeO_2-like solid solution. The lattice parameter of CeO_2 was decreased from 5.416 to 5.407, indicating the incorporation of Cu into ceria lattice. This decreased lattice parameter was in accordance with the study by Qin et al [8].

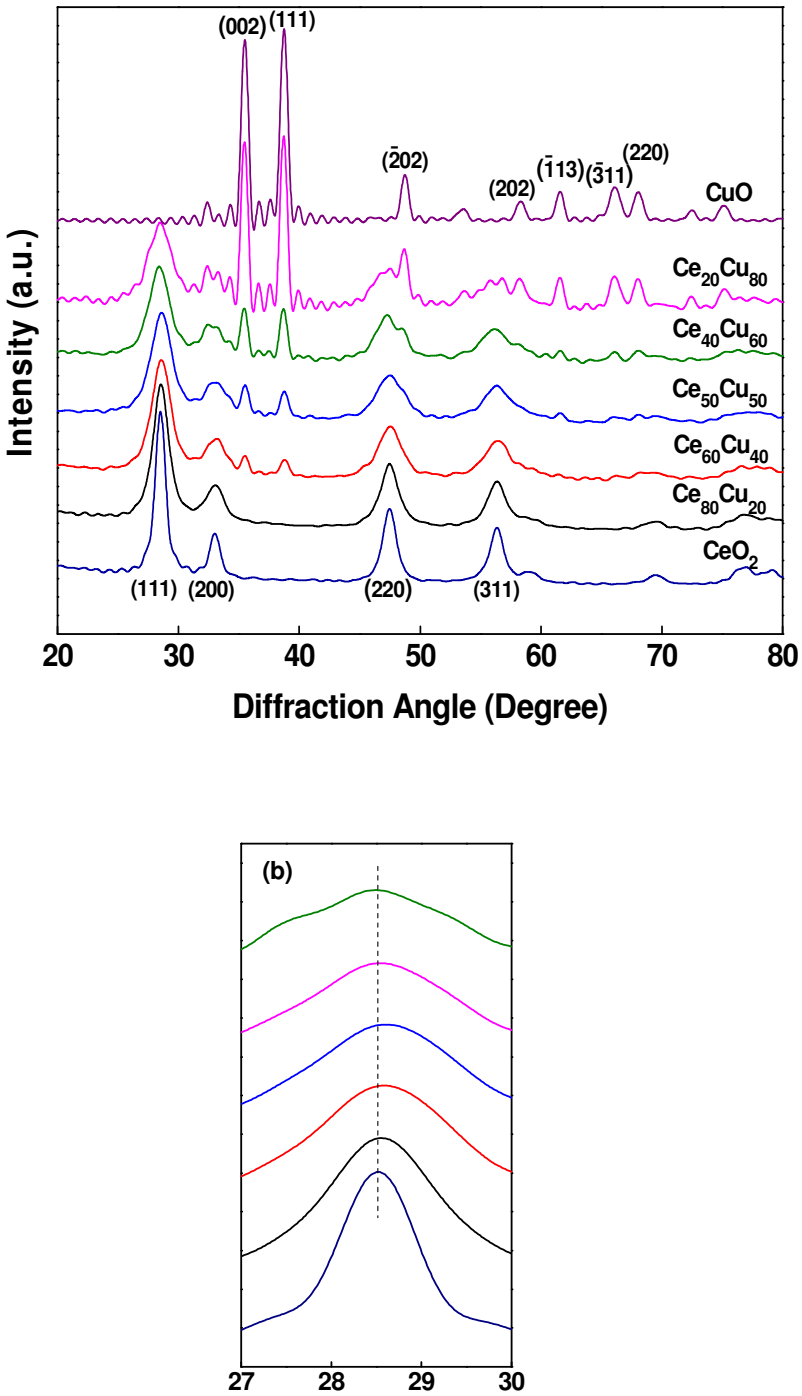

Fig.5.1. (a) XRD pattern (b) low angle region from 27 to 30°

5.1.2. FT-IR analysis

The FT-IR spectra of CeO_2, CuO and $Ce_{40}Cu_{60}$ catalysts are shown in **Figure 5.2**. CeO_2 presented the characteristic band. CuO exhibited three characteristic infrared peaks bands at 420, 498 and 612 cm^{-1} [9,10]. The decreased band intensity for $Ce_{40}Cu_{60}$ supported the interaction between CuO and CeO_2 phases.

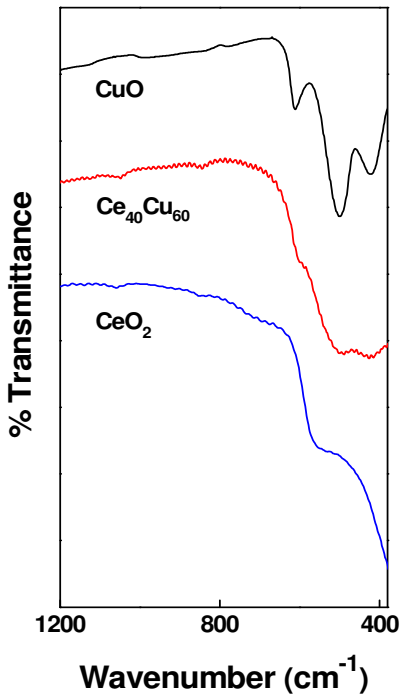

Fig.5.2. FTIR spectra of catalysts

5.1.3. Raman analysis

Raman spectrum of CeO_2, $Ce_{80}Cu_{20}$ and CuO nanocatalysts are shown in **Figure 5.3**. CeO_2 presented the characteristic peak at 462 cm^{-1}. In $Ce_{80}Cu_{20}$ mixed oxide, a less-prominent broad band was observed at 600 cm^{-1}. This particular peak was attributable to the oxygen vacancies in mixed oxide. The I_{600}/I_{462} for $Ce_{80}Cu_{20}$ nanocatalyst was found to be 0.06. CuO exhibited three Raman peaks at 278, 323, and 610 cm^{-1} derived from the Ag, B_1g, and B_2g modes of bulk CuO crystals, respectively [11,12].

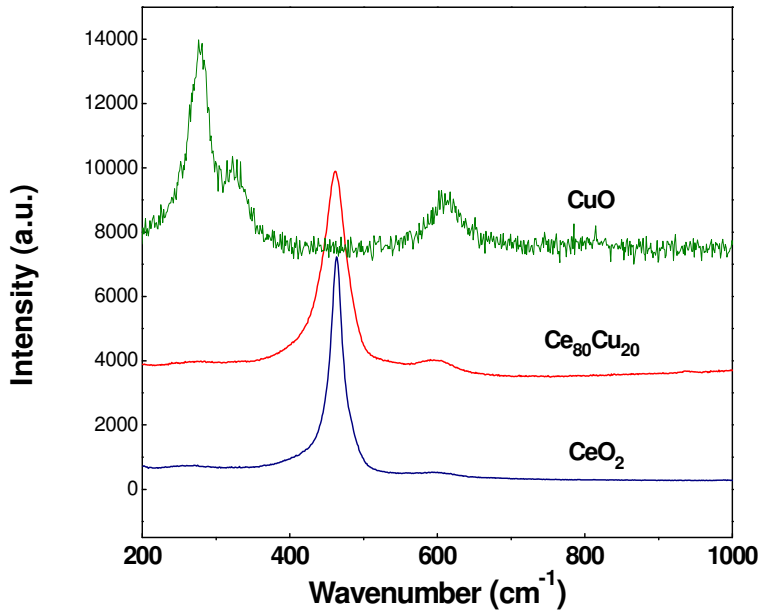

Fig.5.3. Raman spectra of catalysts

5.1.4. XPS analysis

The Ce 3d XPS spectra of $Ce_{40}Cu_{60}$ nanocatalyst **(Figure 5.4(a))** exhibited three main $3d_{5/2}$ features at the binding energies of 881.1, 887.3, 897 eV corresponding to v, v″, v‴ components, respectively. The $3d_{3/2}$ feature corresponding to u, u″ and u‴ components were observed at 899.4 eV, 906.6 eV and 915.8 eV. The v and u splitting was found to be 18.3 eV. The components corresponding to Ce^{3+} were present at 879.9 eV (v^o), 885.3 eV (v′), 898 eV (u^o), and 900.7 eV (u′). Ce^{3+} percentage of 27% indicated the under stoichiometry of ceria. **Figure 5.4(b)** presents the Cu 2p core level binding energy spectra of the $Ce_{40}Cu_{60}$ nanocatalysts. The Cu $2p_{3/2}$ peak profile indicated strong fitting peaks at around 931.2 eV for Cu^+ and 932.3 eV for Cu^{2+} peaks. The well-defined shake-up satellite peaks at 940.2 and 942.3 eV are also typical of Cu^{2+} species, generated due to multiplet splitting of fully oxidized CuO [13,14]. The O 1s spectra (**Figure 5.4(c)**) of $Ce_{40}Cu_{60}$ mixed oxide exhibited three components corresponding to lattice oxygen/ structural oxygen (528.1 eV, 74.2%), supercharged oxygen (O_2^-) near oxygen vacant sites at the surface (529.9 eV, 17.2%) and adsorbed surface oxygen in the form of OH ions (530.8 eV, 8.5%). The peak at 529.9 eV evidenced the oxygen storage/release capacity of nanocatalyst. Thus XPS

analysis also confirmed the presence of oxygen vacancies accompanied with Ce^{4+} reducing to Ce^{3+} in presence of Cu^{2+} and Cu^{+} ions.

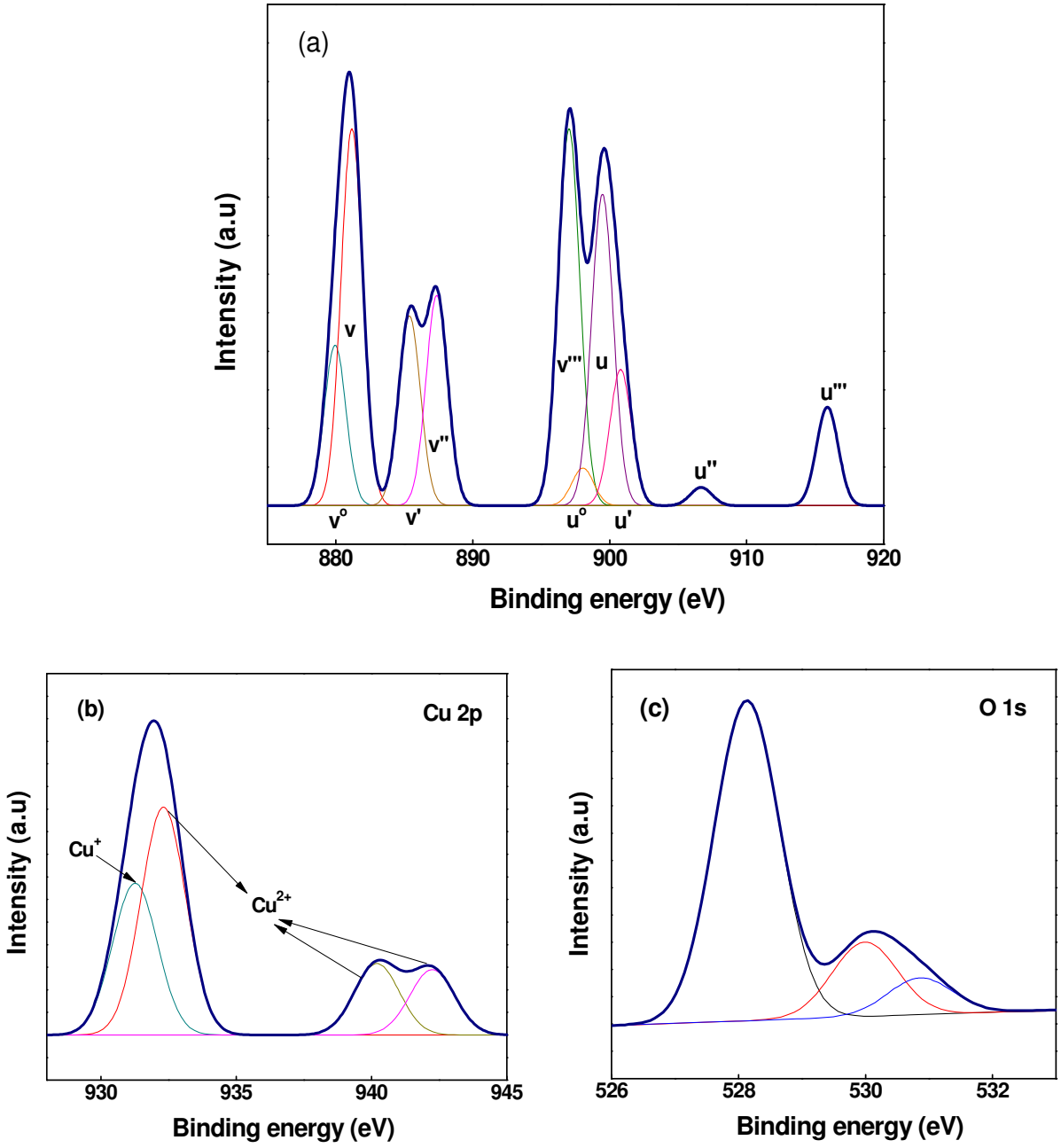

Fig.5.4. XPS spectra of $Ce_{40}Cu_{60}$ catalyst (a) Ce 3d (b) Cu 2p (c) O1s

5.1.5. N_2-adsorption/desorption analysis

N_2-adsorption isotherm of CeO_2, CuO and $Ce_{40}Cu_{60}$ catalysts presented the inflection at high relative pressure **(Figure 5.5(a))**, indicating the filling of secondary pores. Desorption isotherm resulted in a narrow hysteresis. The shape of hysteresis suggested the non-uniform distribution of pores. The pore size distributions are presented in **(Figure 5.5(b))**, which further confirmed the presence of disordered pores. The pores for $Ce_{40}Cu_{60}$ mixed oxide were found to be relatively uniform (3-7 nm). The textural properties i.e., BET surface area (SA) and pore volume (PV) of all samples are summarized in **Table 5.1**. The data indicate that CuO-CeO_2 nanocatalysts possess high BET surface area and pore volume, than the single metal oxides. $Ce_{40}Cu_{60}$ nanocatalyst exhibited the maximum SA of 143 $m^2 g^{-1}$ and PV of 0.386 cc g^{-1}, which is quite larger than the earlier reports by Shan et al. (SA-92 $m^2 g^{-1}$, PV-0.1 cc g^{-1}) [15], Rao et al. (SA-60 $m^2 g^{-1}$) [16], Sun et al. (SA-11 $m^2 g^{-1}$) [17] and Pokrovski et al. (SA-53.7 $m^2 g^{-1}$) [18]. The SA and PV of CuO-CeO_2 nanocatalysts were comparable to the recent study by He et al. [19] and Wang et al. [20], where the samples were fabricated by fast-microwave assisted and hard template (mesoporous KIT-6) method, respectively.

Table 5.1. Structural and textural parameters of CuO-CeO_2 nano-catalysts

Sample	[a]Crystallite size (nm)		[a]Lattice Parameter	[b]Particle size range	[c]BET surface area	[c]Total pore volume
	CeO_2	CuO	CeO_2	(nm)	(m^2/g)	(cc/g)
CeO_2	10.6	--	5.416	44-46	20	0.089
$Ce_{80}Cu_{20}$	5.5	--	5.407	34-36	64	0.201
$Ce_{60}Cu_{40}$	4.7	9.7	5.407	12-14, 21-24	90	0.105
$Ce_{50}Cu_{50}$	4.3	10	5.407	16-20	114	0.382
$Ce_{40}Cu_{60}$	4	10.5	5.407	18-20	143	0.386
$Ce_{20}Cu_{80}$	3.5	10.6	5.416	16-18	104	0.204
CuO	--	11		36-40	32	0.076

[a]Calculated from Scherrer equation , [b]FE-SEM micrographs, [c]N_2 sorption isotherms

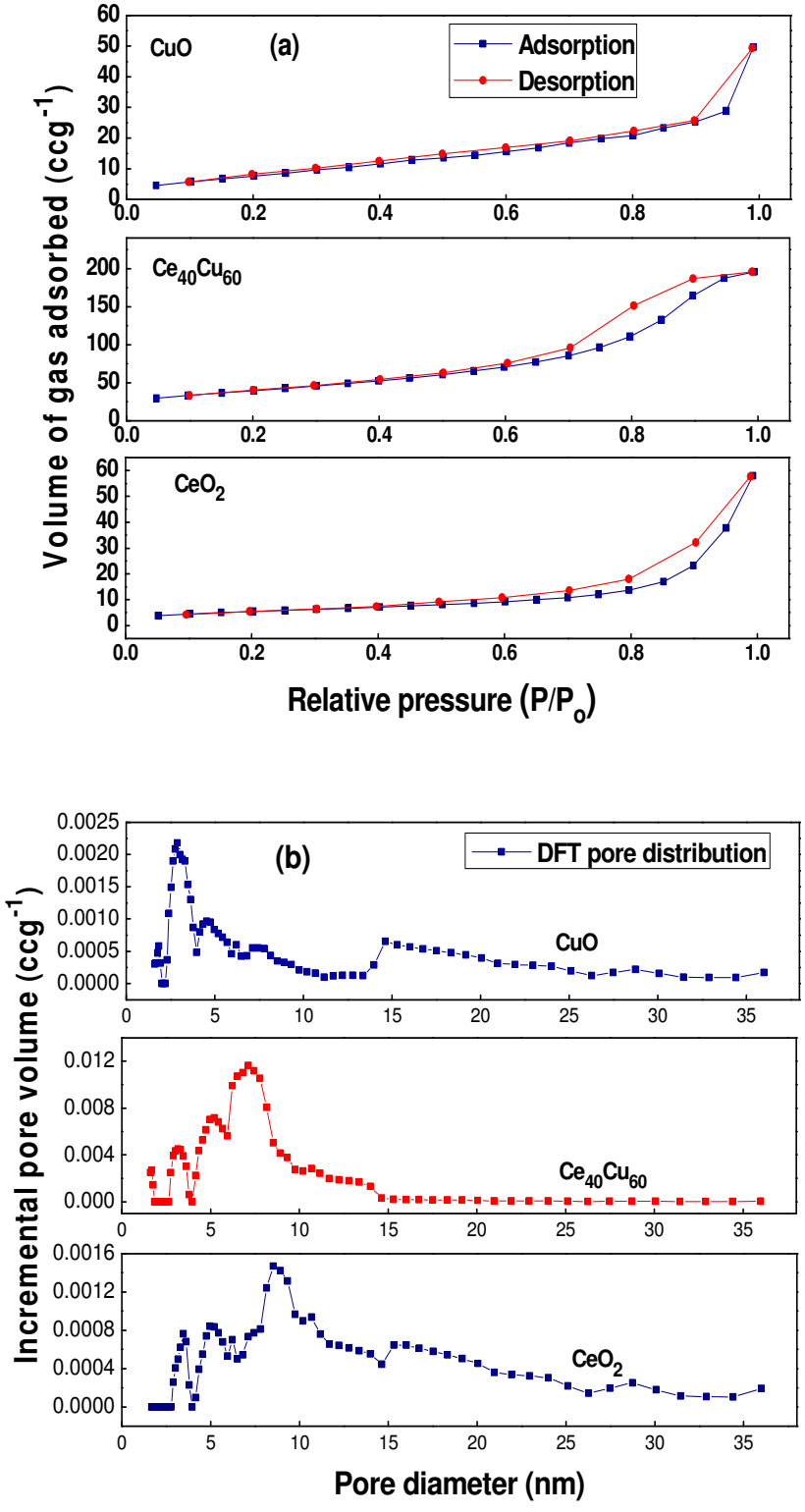

Fig.5.5. (a) N_2-adsorption/desorption isotherm (b) Pore size distribution

5.1.6. FE-SEM and TEM analysis

Figure 5.6 presents the FE-SEM micrographs of catalysts. The particle size ranges assessed from micrographs are reported in **Table 5.1**. As depicted in table, average particle size of CeO_2 was 45 nm which decreased to 35 nm for $Ce_{80}Cu_{20}$ catalyst, further increase in Cu content resulted in considerable decrease in particle size. These results were in good agreement with XRD analysis. EDX spectra of mixed oxides are presented in **Figure 5.7**, and the expected as well as obtained values of Ce/Cu mole ratio are provided in **Table 5.2**. EDX analysis confirmed that the obtained mole ratio values were close to the expected values, confirming the presence of Ce and Cu with required mole ratio.

The TEM micrographs of CeO_2, $Ce_{40}Cu_{60}$ and CuO catalysts along with their SAED patterns are shown in **Figure 5.8**. The presence of disordered pores was further confirmed by TEM micrographs. The average particle sizes (from TEM micrographs) of CeO_2, $Ce_{40}Cu_{60}$ and CuO catalysts were found to be 16, 4 and 8 nm, respectively. The diffraction rings in SAED patterns of $Ce_{40}Cu_{60}$ coincide with the (111), (220) planes of CeO_2 and ($\bar{1}$11), (111), ($\bar{2}$02), (202) planes of CuO, confirming its polycrystalline nature.

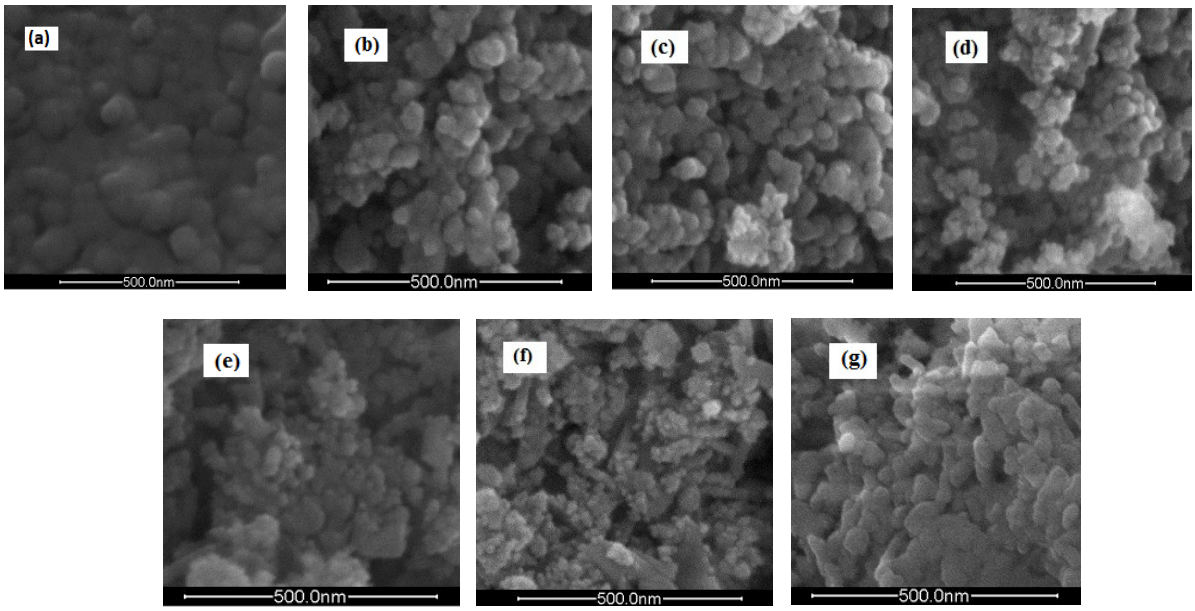

Fig.5.6. FE-SEM micrographs of catalysts (a) CeO_2 (b) $Ce_{80}Cu_{20}$ (c) $Ce_{60}Cu_{40}$ (d) $Ce_{50}Cu_{50}$ (e) $Ce_{40}Cu_{60}$ (f) $Ce_{20}Cu_{80}$ (g) CuO

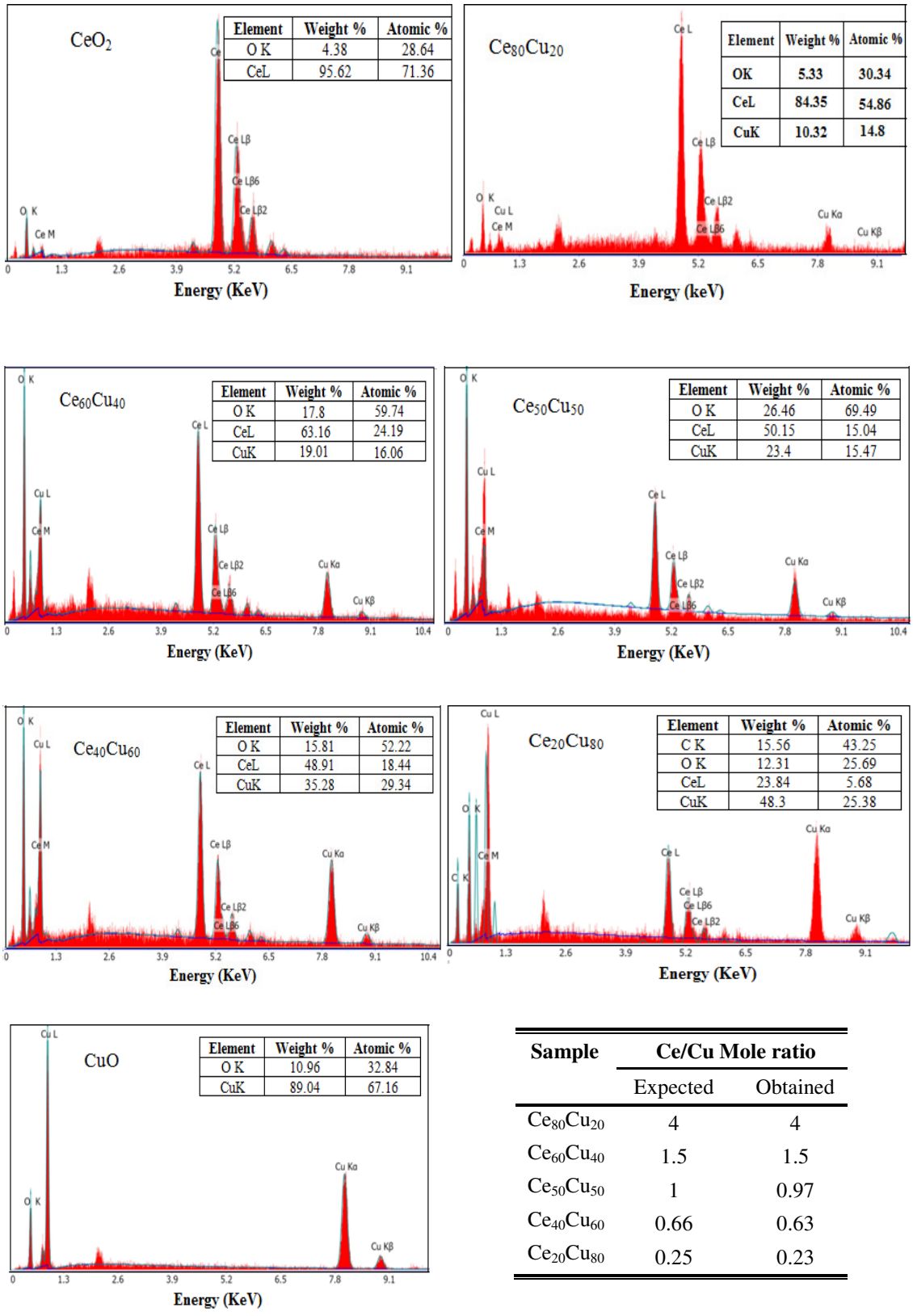

Sample	Ce/Cu Mole ratio	
	Expected	Obtained
$Ce_{80}Cu_{20}$	4	4
$Ce_{60}Cu_{40}$	1.5	1.5
$Ce_{50}Cu_{50}$	1	0.97
$Ce_{40}Cu_{60}$	0.66	0.63
$Ce_{20}Cu_{80}$	0.25	0.23

Fig.5.7. EDX spectra of catalysts

Table 5.2. Ce/Cu mole ratio from EDX

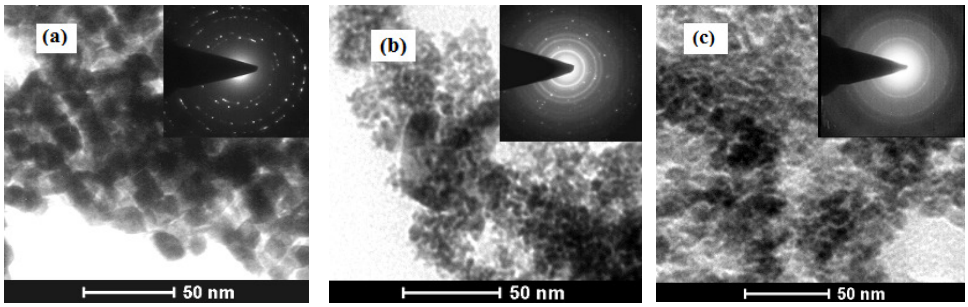

Fig.5.8. TEM micrographs and SAED pattern of (a) CeO_2 (b) $Ce_{40}Cu_{60}$ (c) CuO

5.2. CWAO study over CuO-CeO_2 nanocatalysts

The treatment efficiency of CuO-CeO_2 catalysts in terms of COD, color, AOX and TOC removal is presented in **Figure 5.9**. The mixed catalysts exhibited high removal efficiency, which increased with increasing Cu content and reached maximum with $Ce_{40}Cu_{60}$ catalyst (67% COD, 81% color, 61% AOX and 64% TOC abatement). The BI of wastewater was enhanced up to 0.45 after CWAO over $Ce_{40}Cu_{60}$ nanocatalyst.

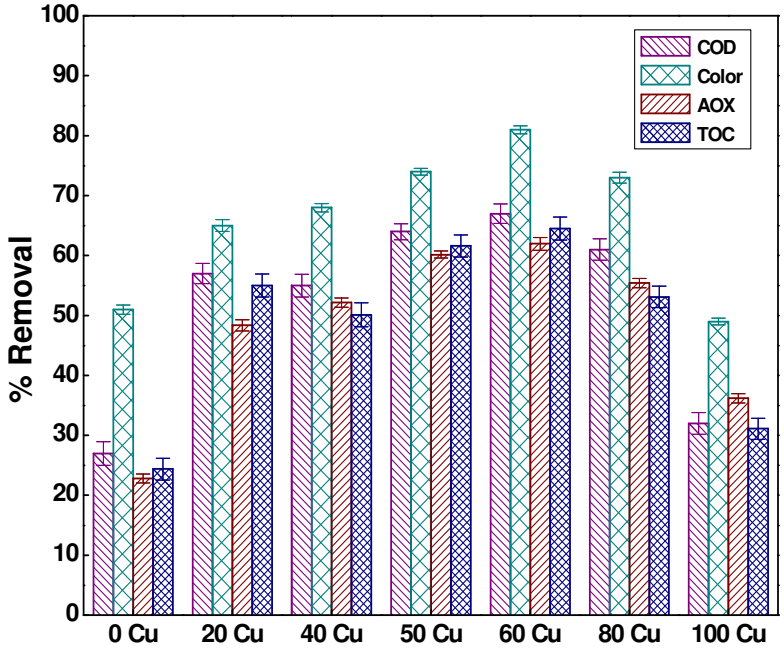

Fig.5.9. Effect of mole ratio on COD, color, AOX and TOC removal

Chlorophenolics removal

GC chromatogram of CHPs after CWAO in presence of $Ce_{40}Cu_{60}$ catalyst is shown in **Figure 5.10**. After CWAO treatment total 19 CHPs **(Table 5.3)** were detected with overall removal of 66%. The removal of most of CHPs was from 47% to 100%. The compounds like PCP, 2,3-DCP, 3,4-DCP, 2,4,6-TCP, 3,4,6-TCG and 2,6-DCSA were completely removed or their concentration fallen below the detection limit of instrument. TCS was removed up to 93.5%, followed by 2,3,5,6-TeCGU (84.3%), 2,3,4-TCP (80.3%), 4,5-DCG (78.1%), 3,4,5-TCG (77.2%), 4,5,6-TCG (76.6%), 4-CG (75.6%), 2,4,5-TCP (67.2%), 2,6-DCP (66%) and 2,5-DCP (62.9%). The rest of the compounds were removed up to 14-50%, whereas 4-CP was reduced only by 8 %. Analysis of treatment data according to chemical family showed 60.5%, 76.7%, 93.5% and 100% removal of CP, CG, CS and CSA, respectively **(Figure 5.11 (a))**. Low removal efficiencies were achieved for CC (17.5%) and CV (14.4%). The removal of PCHPs was highest (100%) followed by TeCHPs (84.3%), TCHPs (68%), DCHPs (66.2%) and MCHPs (63.7%), **(Figure 5.11 (b))**.

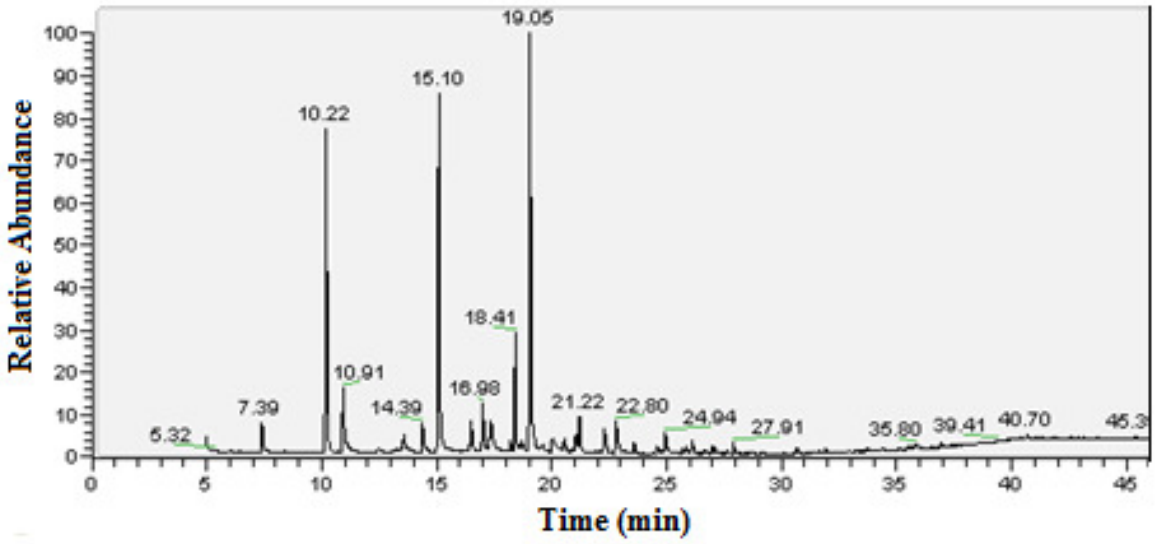

Fig.5.10. GC-MS chromatogram of CHPs after treatment

Table 5.3. Concentration of CHPs with percent removal

S.No.	Name of compound	Initial (µg/L)	Final(µg/L)	% Removal
1.	3-CP	14.9 ± 10.91	11.9 ± 2.08	19.9
2.	4-CP	6.2 ± 4.55	5.7 ± 0.12	8.1
3.	2,3-DCP	0.8 ± 0.01	ND	100
4.	2,4-DCP	26.5 ± 0.47	13.4 ± 0.67	49.5
5.	2,5-DCP	62.4 ± 0.78	23.1 ± 1.21	62.9
6.	2,6-DCP	22.9 ± 4.45	7.8 ± 1.16	66
7.	3,4-DCP	0. 6 ± 0.08	ND	100
8.	2,3,4-TCP	3.3 ± 0.10	0.6 ± 0.09	80.3
9.	2,3,5-TCP	2.5 ± 0.03	1.7 ± 0.43	32.1
10.	2,3,6-TCP	1.2 ± 0.01	0.8 ± 0.13	34.2
11.	2,4,5-TCP	132.9 ± 19.69	43.6 ± 0.42	67.2
12.	2,4,6-TCP	0.4 ± 0.03	ND	100
13.	PCP	0.4 ± 0.02	ND	100
14.	4-CG	83.6 ± 19.45	20.4 ± 0.83	75.6
15.	4,5-DCG	103 ± 1.92	22.6 ± 0.3	78.1
16.	4,6-DCG	2.6 ± 0.52	1.4 ± 0.3	47.4
17.	3,4,5-TCG	0.6 ± 0.11	0.15 ± 0.05	77.2
18.	3,4,6-TCG	0.5 ± 0.19	ND	100
19.	4,5,6-TCG	0.7 ± 0.10	0.2 ± 0.08	76.6
20.	2,3,5,6-TeCG	1.8 ± 0.22	0.3 ± 0.07	84.3
21.	3,5-DCC	2.9 ± 0.21	2.4 ± 1.02	17.4
22.	3,6-DCC	8.5 ± 0.05	7 ± 2.0	17.5
23.	5,6-DCV	0.3 ± 0.09	0.2 ± 0.05	14.5
24.	TCS	5.9 ± 0.89	0.4 ± 0.13	93.5
25.	2,6-DCSA	0.09 ± 0.02	ND	100
	Total	**485**	**164**	**66**

*ND- Not Detected

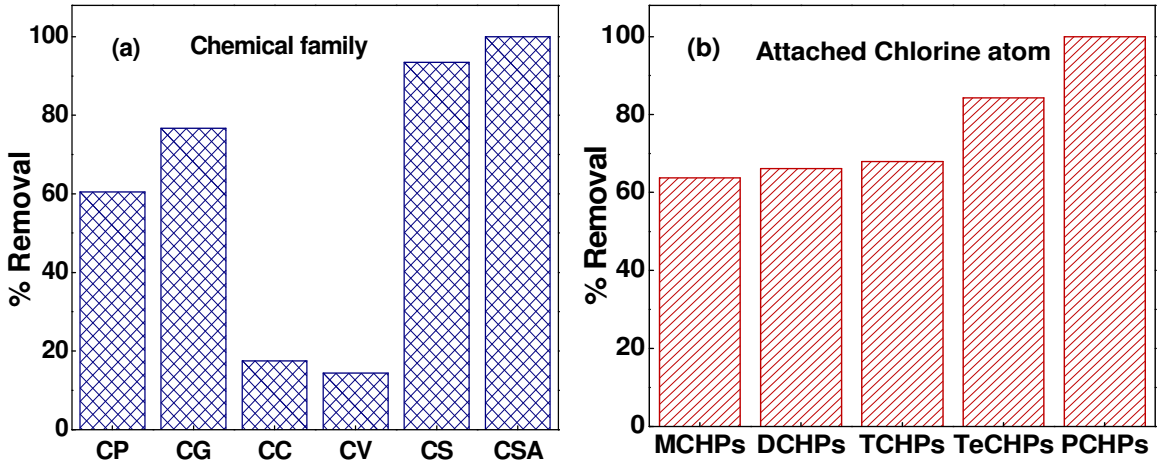

Fig.5.11. Percent removal of CHPs

5.3. Reusability and leaching studies

The reusability of $Ce_{40}Cu_{60}$ nanocatalyst was studied up to 4 treatment cycles. Catalytic run over the used catalyst (calcined) indicated that after two cycles the COD and color removal was still satisfactory i.e., 64% and 77%, respectively **(Figure 5.12)**.

The Ce IV (418.6 nm) concentrations in treated wastewater ranged from 0.104 to 0.133 ppm and Cu II (324.7 nm) concentrations ranged from 0.346-0.636 ppm. The leaching value of metals was comparably lower than the previous reports, [21,22] indicating the stability of catalyst.

5.4. Kinetic studies

The kinetic study on time-dependent COD removal indicated the first order kinetics as straight line with R^2 values of 0.972 was obtained in the plot constructed between $\ln[COD]_o/[COD]$ and time (t) **(Figure 5.13)**.

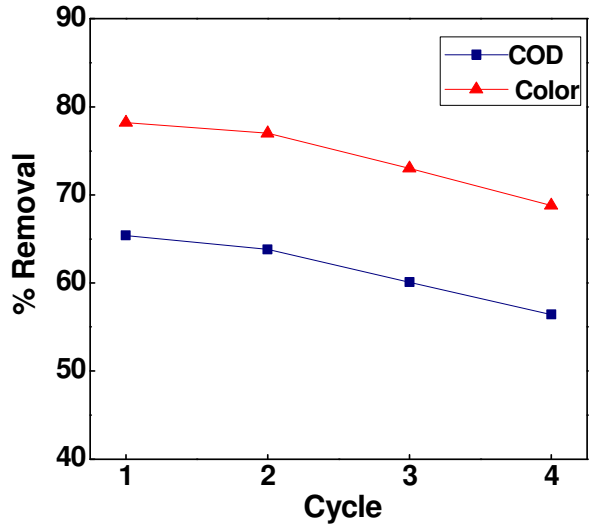

Fig.5.12. COD and color removal during reuse cycles

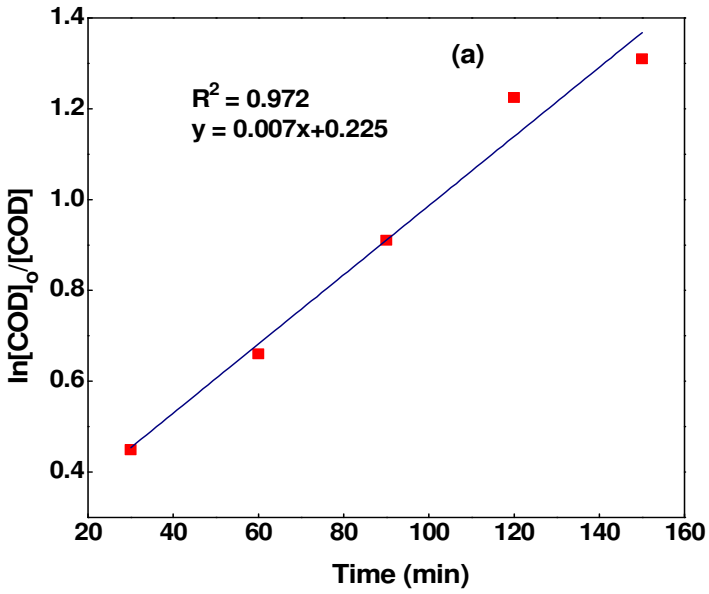

Fig.5.13. The linear fitting of $\ln[\mathrm{COD}]_o/[\mathrm{COD}]$ as a function of reaction time

5.5. SUMMARY

1. Addition of Cu resulted in positive modifications on structural, textural and catalytic properties of CeO_2 nanocatalyst.
2. $Ce_{40}Cu_{60}$ nanocatalyst presented high surface area of 143 m^2g^{-1} and pore volume of 0.386 ccg^{-1}. The pore size was found to be 3-7 nm.
3. Raman analysis also confirmed the presence of O-vacancies in mixed oxide.
4. XPS analysis indicated the presence of high and low oxidation states for Ce (4+, 3+) and Cu (2+, 1+) metal ions in $Ce_{40}Cu_{60}$ nanocatalyst. Ce^{3+} concentration was found to be 27%.
5. $Ce_{40}Cu_{60}$ nanocatalyst exhibited maximum COD (67%), color (81%), TOC (64%), AOX (61%) and CHPs (66%) removal.
6. Biodegradability index increased from 0.27 to 0.45 after treatment.
7. CWAO was found to follow the first order kinetics with R^2 values of 0.972.
8. The catalyst exhibited low leaching values for Ce (0.104 to 0.133 ppm) and Cu (0.346-0.636 ppm) metals.

References

[1] Tanasoi, S., Tanchoux, N., Urdă, A., Tichit, D., Săndulescu, I., Fajula, F. and Marcu, I.C., 2009. New Cu-based mixed oxides obtained from LDH precursors, catalysts for methane total oxidation. *Applied Catalysis A: General*, *363*(1), pp.135-142.

[2] Tidahy, H.L., Siffert, S., Wyrwalski, F., Lamonier, J.F. and Aboukaïs, A., 2007. Catalytic activity of copper and palladium based catalysts for toluene total oxidation. *Catalysis Today*, *119*(1), pp.317-320.

[3] Pan, W., Zhang, G., Zheng, T. and Wang, P., 2015. Degradation of p-nitrophenol using CuO/Al_2O_3 as a Fenton-like catalyst under microwave irradiation. *RSC Advances*, *5*(34), pp.27043-27051.

[4] Ma, H., Zhuo, Q. and Wang, B., 2007. Characteristics of $CuO\text{-}MoO_3\text{-}P_2O_5$ catalyst and its catalytic wet oxidation (CWO) of dye wastewater under extremely mild conditions. *Environmental science & technology*, *41*(21), pp.7491-7496.

[5] Zaman, S., Zainelabdin, A., Amin, G., Nur, O. and Willander, M., 2012. Efficient catalytic effect of CuO nanostructures on the degradation of organic dyes. *Journal of Physics and Chemistry of Solids*, *73*(11), pp.1320-1325.

[6] Tanaka, Y., Utaka, T., Kikuchi, R., Sasaki, K. and Eguchi, K., 2003. Water gas shift reaction over Cu-based mixed oxides for CO removal from the reformed fuels. *Applied Catalysis A: General*, *242*(2), pp.287-295.

[7] Sedmak, G., Hočevar, S. and Levec, J., 2003. Kinetics of selective CO oxidation in excess of H_2 over the nanostructured $Cu_{0.1}Ce_{0.9}O_{2-y}$ catalyst. *Journal of Catalysis*, *213*(2), pp.135-150.

[8] Qin, R., Chen, J., Gao, X., Zhu, X., Yu, X. and Cen, K., 2014. Catalytic oxidation of acetone over $CuCeO_x$ nanofibers prepared by an electrospinning method. *RSC Advances*, *4*(83), pp.43874-43881.

[9] Ethiraj, A.S. and Kang, D.J., 2012. Synthesis and characterization of CuO nanowires by a simple wet chemical method. *Nanoscale research letters*, *7*(1), pp.1-5.

[10] Zhao, B., Liu, P., Zhuang, H., Jiao, Z., Fang, T., Xu, W., Lu, B. and Jiang, Y., 2013. Hierarchical self-assembly of microscale leaf-like CuO on graphene sheets for high-performance electrochemical capacitors. *Journal of Materials Chemistry A*, *1*(2), pp.367-373.

[11] Debbichi, L., Marco de Lucas, M.C., Pierson, J.F. and Kruger, P., 2012. Vibrational properties of CuO and Cu_4O_3 from first-principles calculations, and Raman and infrared spectroscopy. *The Journal of Physical Chemistry C*, *116*(18), pp.10232-10237.

[12] Guha, S., Peebles, D. and Wieting, T.J., 1991. Zone-center (q=0) optical phonons in CuO studied by Raman and infrared spectroscopy. *Physical Review B*, *43*(16), pp.13092-13101.

[13] Chusuei, C.C., Brookshier, M.A. and Goodman, D.W., 1999. Correlation of relative X-ray photoelectron spectroscopy shake-up intensity with CuO particle size. *Langmuir*, *15*(8), pp.2806-2808.

[14] Huang, M., Zhang, Y., Li, F., Wang, Z., Hu, N., Wen, Z. and Liu, Q., 2014. Merging of Kirkendall growth and Ostwald ripening: CuO@MnO_2 core-shell architectures for asymmetric supercapacitors. *Scientific reports*, *4*. DOI: 10.1038/srep04518.

[15] Shan, W., Feng, Z., Li, Z., Zhang, J., Shen, W. and Li, C., 2004. Oxidative steam reforming of methanol on $Ce_{0.9}Cu_{0.1}O_y$ catalysts prepared by deposition-precipitation, coprecipitation, and complexation-combustion methods. *Journal of catalysis*, *228*(1), pp.206-217.

[16] Rao, G.R., Sahu, H.R. and Mishra, B.G., 2003. Surface and catalytic properties of Cu-Ce-O composite oxides prepared by combustion method.*Colloids and Surfaces A: Physicochemical and Engineering Aspects*, *220*(1), pp.261-269.

[17] Sun, S., Mao, D., Yu, J., Yang, Z., Lu, G. and Ma, Z., 2015. Low-temperature CO oxidation on CuO/CeO_2 catalysts: the significant effect of copper precursor and calcination temperature. *Catalysis Science & Technology*, *5*(6), pp.3166-3181.

[18] Pokrovski, K.A. and Bell, A.T., 2006. An investigation of the factors influencing the activity of Cu/$Ce_xZr_{1-x}O_2$ for methanol synthesis via CO hydrogenation. *Journal of Catalysis*, *241*(2), pp.276-286.

[19] He, C., Yu, Y., Chen, C., Yue, L., Qiao, N., Shen, Q., Chen, J. and Hao, Z., 2013. Facile preparation of 3D ordered mesoporous CuO_x-CeO_2 with notably enhanced efficiency for the low temperature oxidation of heteroatom-containing volatile organic compounds. *RSC Advances*, *3*(42), pp.19639-19656.

[20] Wang, X., Wen, W., Su, Y. and Wang, R., 2015. Influence of transition metals (M= Co, Fe and Mn) on ordered mesoporous CuM/CeO_2 catalysts and applications in selective catalytic reduction of NO_x with H_2. *RSC Advances*, *5*(77), pp.63135-63141.

[21] Arena, F., Giovenco, R., Torre, T., Venuto, A. and Parmaliana, A., 2003. Activity and resistance to leaching of Cu-based catalysts in the wet oxidation of phenol. *Applied Catalysis B: Environmental*, *45*(1), pp.51-62.

[22] Huang, K., Xu, Y., Wang, L. and Wu, D., 2015. Heterogeneous catalytic wet peroxide oxidation of simulated phenol wastewater by copper metal–organic frameworks. *RSC Advances*, *5*(41), pp.32795-32803.

Chapter 6

Ni-Ce Nanocatalysts: Characterization and application in CWAO

NiO based materials have been investigated in oxidation catalysis [1-3]. Ni/MgAlO catalyst achieved 98% degradation with 71.4% TOC conversion in CWAO of Crystal Violet [4]. NiO supported on mesoporous silica monoliths (NiO/HOM-9) presented complete oxidation of o-aminophenols in heterogeneous oxidation reaction [5]. Different $Ce_{1-x}Ni_xO_2$ mixed oxides have been studied in complete oxidation of CO [6-8].

Therefore, NiO was selected for the formation of mixed oxides with CeO_2. This chapter describes the results and discussion pertaining to the structural and textural characteristics of nanosized NiO-CeO_2 oxides, followed by their activity in CWAO of wastewater.

6.1. Characterization of NiO-CeO_2 mixed oxides

6.1.1. XRD analysis

The diffraction pattern of NiO-CeO_2 nanocatalysts are shown in **Figure 6.1(a)**. CeO_2 diffraction pattern was consistent with JCPDS file 81-0792, as discussed in **Chapter 3**. NiO exhibited reflections at 2θ = 37.3°, 43.3° and 62.9° corresponding to (111), (200) and (220) crystal planes (JCPDS 75-0197. Absence of NiO peaks in $Ce_{80}Ni_{20}$ manifested that Ni species entered into the lattice of ceria. Other mixed oxides displayed the diffraction peaks for both CeO_2 and NiO. This indicated that with increasing NiO content, a part of Ni^{+2} was incorporated into ceria lattice and a part of Ni^{+2} was crystallized onto its surface. The diffraction peaks for mixed phases were broadened **Figure 6.1(b)**, indicating smaller crystallite size than pure CeO_2 [9]. The crystallite size and lattice parameter of samples are listed in **Table 6.1**. Results indicated that the crystallite size decreased significantly with increasing Ni content. The lattice parameter of CeO_2 was decreased from 5.416Å to 5.401Å which was in accordance with the previous studies [6,8].

6.1.2. FTIR analysis

The FTIR spectra of CeO_2, $Ce_{40}Ni_{60}$ and NiO catalysts are presented in **Figure 6.2**. CeO_2 exhibited the characteristic band at 560 cm^{-1}. NiO showed a strong absorption band at 413 cm^{-1}, attributable to Ni-O bond vibration [10]. The characteristic Ni-O band in $Ce_{40}Ni_{60}$ catalyst was

shifted from 413 to 395 cm^{-1}which could be related to increase in lattice parameter from NiO (4.176 Å) to $Ce_{40}Ni_{60}$ (4.184 Å). Decreased intensity of bands for $Ce_{40}Ni_{60}$ catalyst supported the interaction between CeO_2 and NiO in mixed phase.

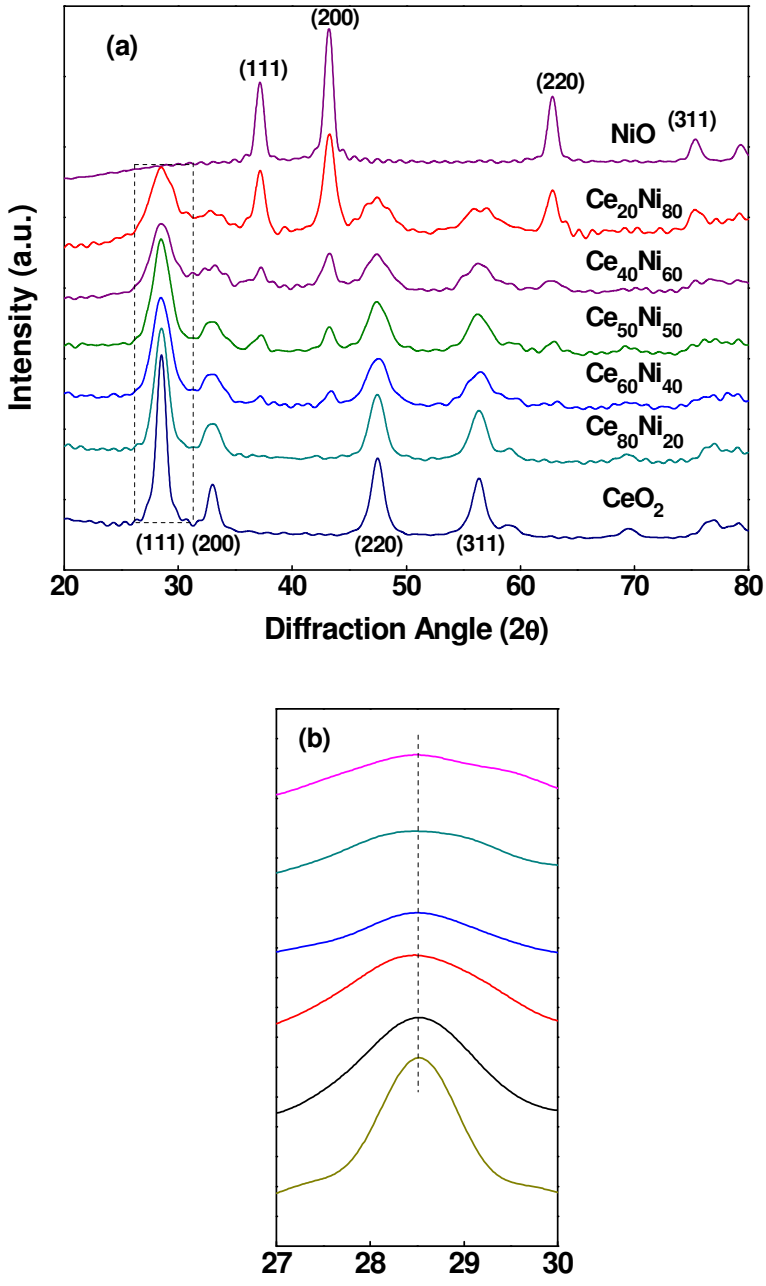

Fig.6.1. (a) XRD pattern of samples (b) low angle region from 27-30°

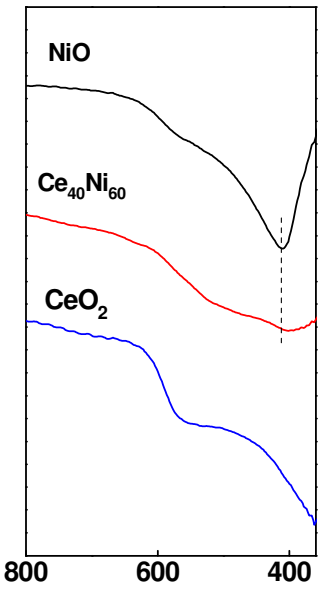

Fig.6.2. FT-IR of catalysts

6.1.3. N_2 adsorption-desorption

N_2 adsorption-desorption isotherms for CeO_2, $Ce_{40}Ni_{60}$ and NiO are presented in **Figure 6.3(a)**. The inflection at higher relative pressure indicated the presence of secondary pores. The desorption isotherms gave rise to the narrow hysteresis, corresponding to the complex shape of pores. Pore size distribution (PSD) confirmed the presence of pores with wide distribution for CeO_2 and NiO (**Figure 3.5 (b)**. $Ce_{40}Ni_{60}$ mixed oxide presented relatively uniform pores of 3-11 nm. The specific surface areas and pore volume of catalysts are summarized in **Table 6.1**. Pure CeO_2 and NiO exhibited the low surface area (CeO_2, 20 $m^2\,g^{-1}$; NiO, 17 $m^2\,g^{-1}$) and pore volume (CeO_2, 0.0897 cc g^{-1}; NiO, 0.092 cc g^{-1}). For mixed oxides, the surface area and pore volume were augmented with increasing Ni content and reached a maximum of 90 $m^2\,g^{-1}$ and 0.275 cc g^{-1} for $Ce_{40}Ni_{60}$ nanocatalyst. The surface area was larger than the previous report by Sun et al. [10] (29m^2 g^{-1}) and Liu et al. [14] (69.3 m^2 g^{-1}), where hydrothermal method was employed for the synthesis. The surface area values were comparable to the study by Solsona et al. [11].

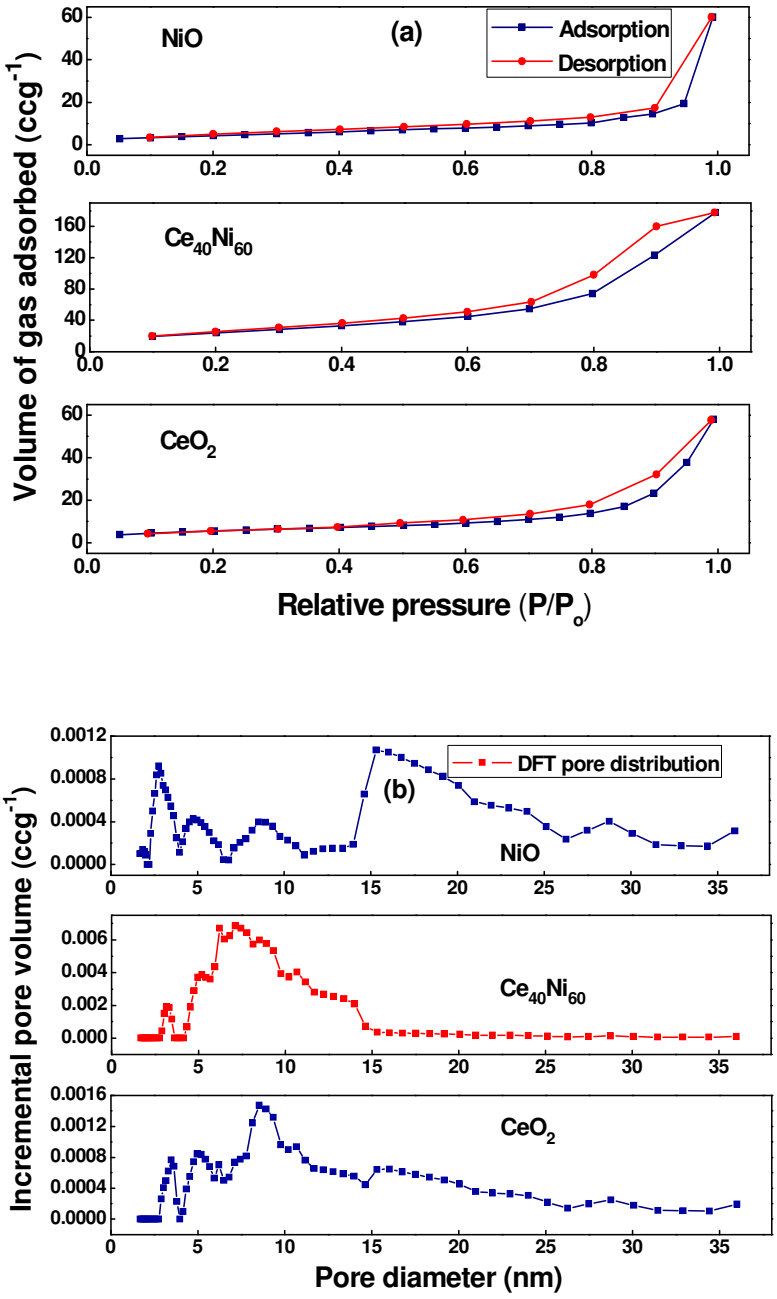

Fig.6.3. (a) N_2 adsorption-desorption isotherms (b) pore size distribution

Table.6.1. Structural and textural parameters of CeO_2-NiO nanocatalysts

Sample	[a]Crystallite size (nm)		[a]Lattice parameter (Å)	[b]Average particle size (nm)	[c]Surface area (m^2/g)	[c]Total pore volume (cc/g)
	CeO_2	NiO				
CeO_2	10.6	--	5.416	44-46	20	0.089
$Ce_{80}Ni_{20}$	6.3	--	5.415	39-43	50	0.148
$Ce_{60}Ni_{40}$	5.6	7.8	5.412	24-26	75	0.242
$Ce_{50}Ni_{50}$	4.7	8.5	5.407	21-24	81	0.255
$Ce_{40}Ni_{60}$	4.1	8.2	5.401	16-17	90	0.275
$Ce_{20}Ni_{80}$	3.2	6.7	5.413	14-17	57	0.261
NiO	--	8.6	--	17-19	17	0.092

[a]Calculated from XRD, [b]FE-SEM micrographs, [c] N_2-sorption isotherms

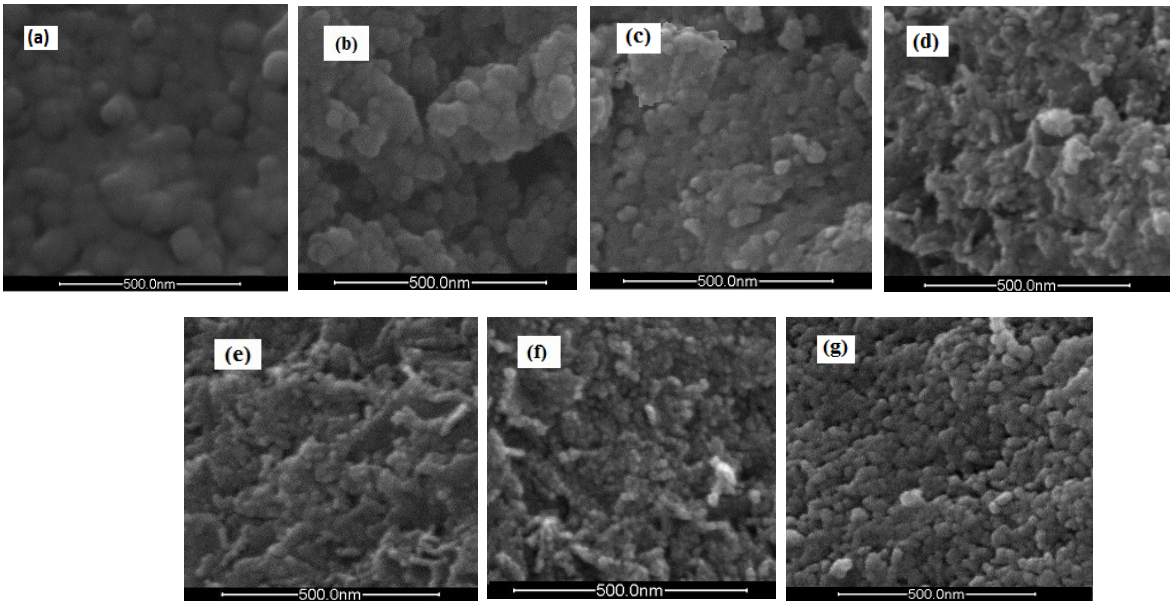

Fig.6.4. FE-SEM (a-g) micrographs of catalysts: (a) CeO_2 (b) $Ce_{80}Ni_{20}$ (c) $Ce_{60}Ni_{40}$ (d) $Ce_{50}Ni_{50}$ (e) $Ce_{40}Ni_{60}$ (f) $Ce_{20}Ni_{80}$ (g) NiO

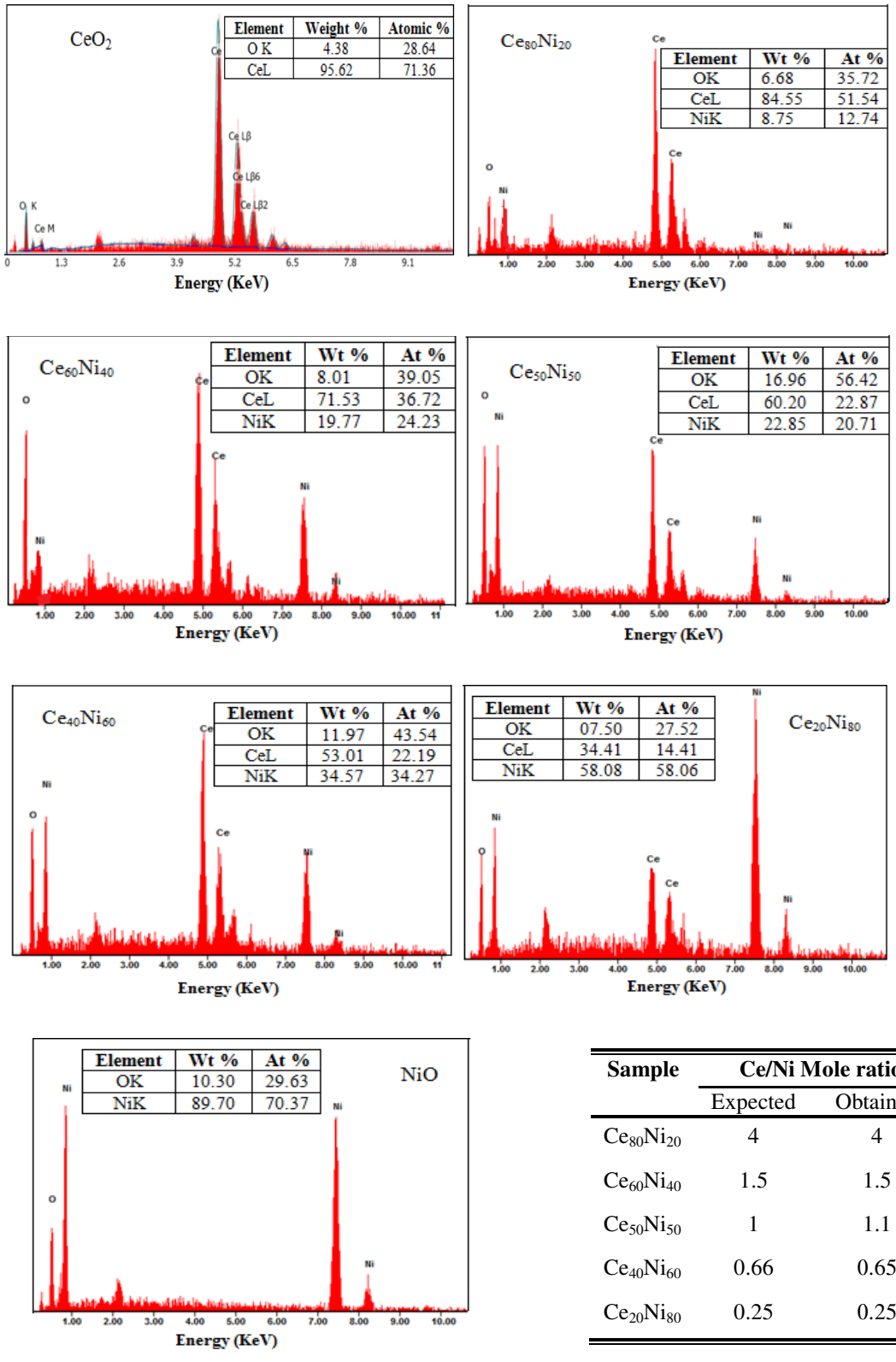

Fig.6.5. EDX spectra of catalysts

Sample	Ce/Ni Mole ratio	
	Expected	Obtained
$Ce_{80}Ni_{20}$	4	4
$Ce_{60}Ni_{40}$	1.5	1.5
$Ce_{50}Ni_{50}$	1	1.1
$Ce_{40}Ni_{60}$	0.66	0.65
$Ce_{20}Ni_{80}$	0.25	0.25

Table 6.2. Ce/Ni mole ratio from EDX

6.1.4. FE-SEM and TEM analysis

FE-SEM micrographs of catalysts are presented in **Figure 6.4**. Statistical analysis of micrographs displayed the decrease in particle size with increasing NiO content **(Table 6.1)**. These observations are consistent with XRD results. EDX spectra of mixed oxides are presented in **Figure 6.5**, and the expected as well as obtained values of Ce/Ni mole ratio are provided in **Table 6.2**. EDX analysis confirmed that the obtained mole ratio values were close to the expected values, confirming the presence of Ce and Ni with required mole ratio. **Figure 6.6** represents the TEM micrographs together with SAED pattern of CeO_2, $Ce_{40}Ni_{60}$ and NiO catalysts. Average particle sizes of these catalysts were found to be 16, 13 and 11 nm, respectively. SAED patterns of $Ce_{40}Ni_{60}$ confirmed its polycrystalline nature as the diffraction rings were attributable to (200), (220), (311), (422) planes of cubic CeO_2 and (111), (200), (220), (311) planes of NiO.

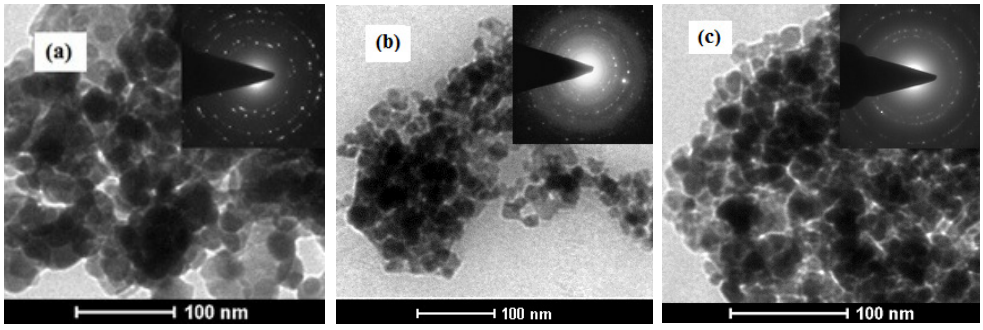

Fig.6.6. TEM image and SAED pattern of (a) CeO_2 (b) $Ce_{40}Ni_{60}$ (c) NiO

6.2. CWAO study over NiO-CeO_2 nanocatalysts

The NiO-CeO_2 nano-catalysts with different Ni contents were evaluated in order to investigate the effect of molar proportion between Ni/Ce on CWAO of wastewater. **Figure 6.7** compares the percent removal efficiency of CeO_2, Ni-Ce-O (20/80), Ni-Ce-O (40/60), Ni-Ce-O (50/50), Ni-Ce-O (60/40), Ni-Ce-O (80/20) and NiO nano-catalysts. The mixed catalysts exhibited high removal efficiency than the single oxides and it progressively increased with increasing Ni content. The catalyst with Ni/Ce ratios of 60/40 reached the maximum activity with 62% COD, 75% color, 59% TOC and 55%AOX abatement. Highest removal efficiency of $Cu_{60}Ce_{40}$ nanocatalystS was in correlation with the characterization results. The biodegradability index (BI) of wastewater was enhancement up to 0.42.

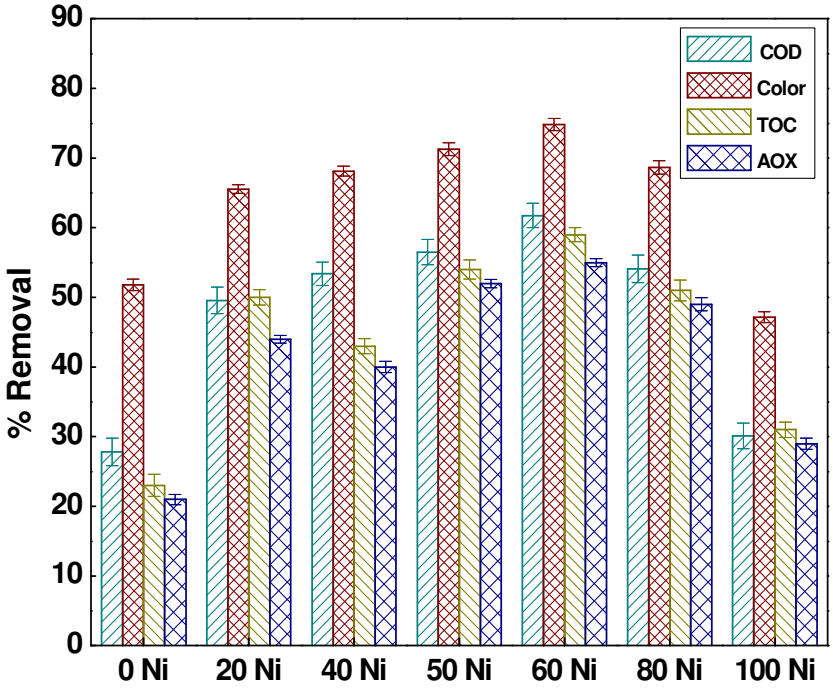

Fig.6.7. Effect of Ce/Ni mole ratio on COD, color, TOC and AOX removal

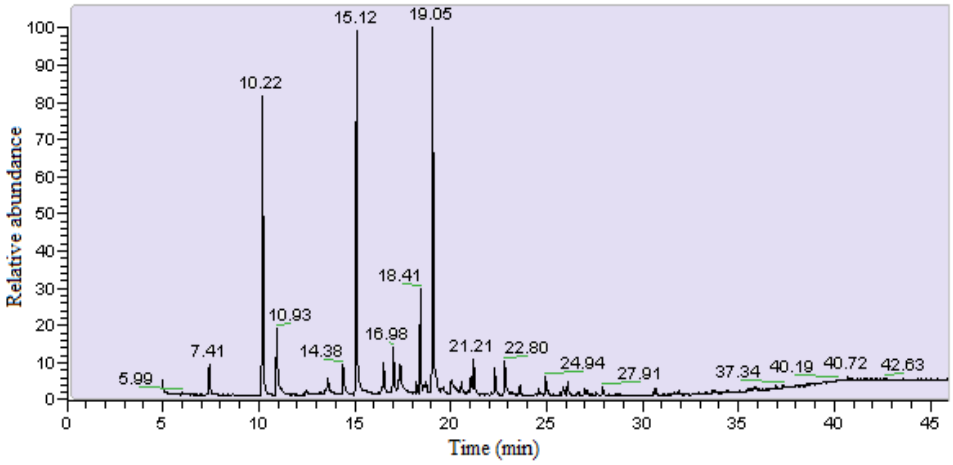

Fig. 6.8. GC-MS chromatogram of CHPs in wastewater after CWAO

Table 6.3. Concentration of CHPs with percent removal

S. No.	Compound	Initial (µg/L)	Final(µg/L)	% Removal
1.	3-CP	14.9 ±10.98	10.3 ± 0.08	31.2
2.	4-CP	6.2 ± 4.55	5.6 ± 0.25	9.4
3.	2,3-DCP	0.8 ± 0.01	ND	100
4.	2,4-DCP	26.5 ± 0.47	14.5 ± 0.60	45.3
5.	2,5-DCP	62.4 ± 0.78	34.5 ±1.23	44.7
6.	2,6-DCP	22.9 ± 4.45	7.8 ±1.87	65.9
7.	3,4- DCP	0.6 ± 0.08	ND	100
8.	2,3,4-TCP	3.3 ± 0.10	0.8 ±0.02	77.0
9.	2,3,5-TCP	2.5 ± 0.03	1.4 ±0.32	43.5
10.	2,3,6- TCP	1.2 ± 0.01	0.7 ±0.07	42.9
11.	2,4,5-TCP	132.9 ± 19.69	97.9 ±5.99	26.3
12.	2,4,6-TCP	0.4 ± 0.03	ND	100
13.	4-CG	83.6 ± 19.45	21.4 ±1.02	74.5
14.	4,5-DCG	102.9 ±1.92	20.7 ±2.03	79.9
15.	4,6-DCG	2.6 ± 0.52	1.4 ± 0.06	48.0
16.	3,4,5-TCG	0.6 ± 0.11	0.3 ± 0.10	55.5
17.	3,4,6-TCG	0.5 ± 0.19	0.2 ± 0.03	60.6
18.	4,5,6-TCG	0.7 ± 0.10	0.2 ± 0.04	75.7
19.	2,3,5,6-TCG	1.8 ± 0.22	0.3 ± 0.05	83.2
20.	3,5- DCC	2.9 ± 0.21	2.7 ± 0.13	8.9
21.	3,6- DCC	8.5 ± 0.05	2.4 ± 0.45	72.2
22.	5,6-DCV	0.3 ± 0.19	0.2 ± 0.06	32.5
23.	TCS	5.9 ± 0.89	2.2 ± 0.43	61.9
24.	2,6-DCSA	0.09 ± 0.02	ND	100
25.	PCP	0.4 ± 0.02	ND	100
	Total	485	225	54%

*ND- Not detected

Chlorophenolics removal

GC chromatogram of CHPs after CWAO in presence of $Ce_{40}Cu_{60}$ catalyst is shown in **Figure 6.8**. After CWAO treatment, total 20 CHPs (out of 25) were detected with overall removal efficiency of 54% **(Table 6.3)**. The removal of most of CHPs was from 30-100%. Compounds like 2,3-DCP, 3,4- DCP, 2,4,6-TCP, 2,6-DCSA and PCP were completely removed or concentration fall below the detection limit of the instrument. 2,3,5,6-TCG was removed up to 83.20 % followed by 4,5-DCG (79.9%), 2,3,4-TCP (77%), 4,5,6-TCG (75.7%), 4-CG (74.5%), 3,6-DCC (72.2%), 2,6-DCP (65.9%), TCS (61.9%), 3,4,6-TCG (60.6%) and 3,4,5-TCG (55.5%). The rest of the compounds were removed up to 26-48% only. 4,6-DCG, 2,4-DCP, 2,5-DCP, 2,3,5-TCP and 2,3,6-TCP were removed only 48%, 45.3%, 44.7%, 43.5% and 42.9%, respectively. 4-CPand 3,5-DCC were removed by 9.4% and 8.9%, only. According to chemical family, complete removal was achieved for CSA, followed by CG (77%), CS (61.9%), CC (55.9%), CP (36.9%) and CV (32.5%) **(Figure 6.9(a))**. According to attached Cl atom, highest degradation was achieved for PCHPs and TeCHPs with 100% and 83.2% removal, respectively. MCHPs, DCHPs and TCHPs were reduced by 64.8%, 63.6% and 29.9%, respectively **(Figure 6.9(b))**.

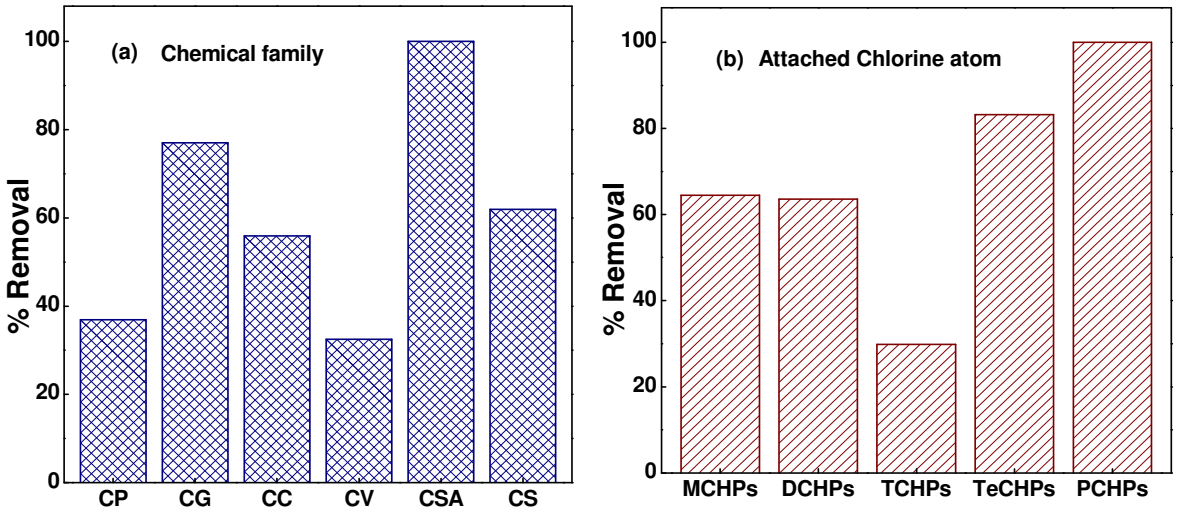

Fig. 6.9. Percent removal of CHPs

6.3. Reusability and Leaching studies

The reusability experiments of $Ce_{40}Ni_{60}$ nanocatalyst were carried out up to 4 treatment cycles (Figure 6). The activity of calcined catalyst was found to be 59% COD and 71% color after two reuse cycles, and further reuse of catalyst lead to considerably decreased activity **(Figure 6.10)**.

The dissolved Ce concentrations in treated wastewater ranged from 0.12 mg/L to 0.16 mg/L and Ni concentration ranged from 0.218-0.643 mg/L for NiO-CeO_2 nano-catalysts. The values of metal leaching was very low [12,13], indicating the negligible leaching.

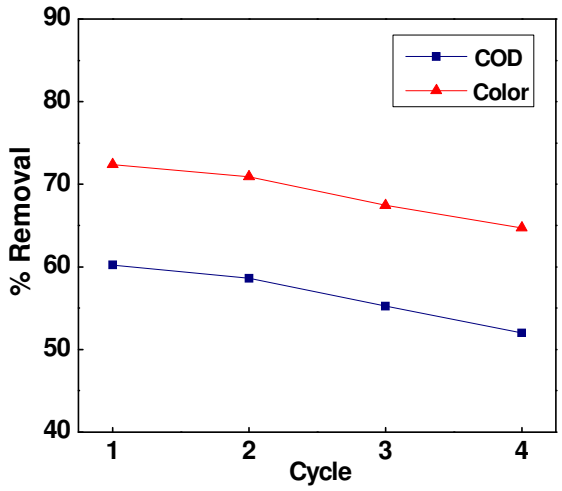

Fig.6.10. COD and color removal during reuse cycles

6.4. Kinetic studies

The first order kinetics was confirmed by the straight line with R^2 values of 0.959 obtained in the plot constructed between $\ln[COD]_o/[COD]$ on x-axis versus time (t) on y-axis **(Figure 6.11)**.

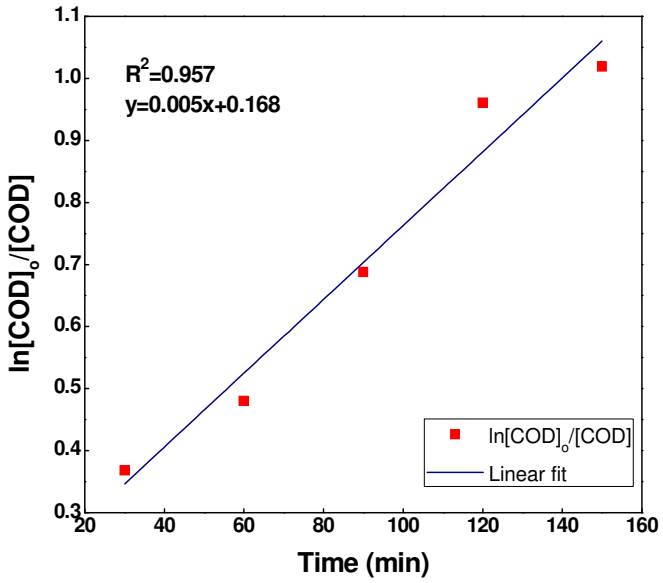

Fig.6.11. The linear fitting of $\ln[COD]_o/[COD]$ as a function of reaction time

6.5. Summary

1. $NiO\text{-}CeO_2$ resulted in improved structural, textural and catalytic property than the single metal oxides.
2. $Ce_{40}Ni_{60}$ mixed oxide presented the surface area of 90 m^2g^{-1} and pore volume of 0.275 ccg^{-1}. The pore size was found to be 3-11 nm.
3. $Ce_{40}Zn_{60}$ mixed oxide exhibited maximum COD (62%), color (75%), AOX (55%), TOC (59%) and CHPs (54%) removal.
4. Biodegradability index increased from 0.27 to 0.42.
5. The first order kinetics was ascertained with R^2 values of 0.957.
6. The low leaching values of Ce (0.12- 0.16 ppm) and Ni (0.218-0.64 ppm) metals was obtained.

References

[1] Yisup, N., Cao, Y., Feng, W.L., Dai, W.L. and Fan, K.N., 2005. Catalytic oxidation of methane over novel Ce-Ni-O mixed oxide catalysts prepared by oxalate gel-coprecipitation. *Catalysis letters*, *99*(3-4), pp.207-213.

[2] Dong, D., Shao, X., Wang, Z., Lievens, C., Yao, J., Wang, H. and Li, C.Z., 2013. Fibrous NiO/CeO_2 nanocatalysts for the partial oxidation of methane at microsecond contact times. *RSC Advances*, *3*(5), pp.1341-1345.

[3] Pantaleo, G., La Parola, V., Deganello, F., Singha, R.K., Bal, R. and Venezia, A.M., 2016. Ni/CeO_2 catalysts for methane partial oxidation: Synthesis driven structural and catalytic effects. *Applied Catalysis B: Environmental*, *189*, pp.233-241.

[4] Ovejero, G., Rodríguez, A., Vallet, A. and García, J., 2012. Intermediary products in the catalytic wet air oxidation of crystal violet with Ni/MgAlO as catalyst. *Industrial & Engineering Chemistry Research*, *51*(35), pp.11367-11372.

[5] El-Safty, S.A., Kiyozumi, Y., Hanaoka, T. and Mizukami, F., 2008. Heterogeneous catalytic activity of NiO-silica composites designated with cubic Pm3n cage nanostructures. *Applied Catalysis B: Environmental*, *82*(3), pp.169-179.

[6] Liu, X., Zuo, Y., Li, L., Huang, X. and Li, G., 2014. Heterosturcture $NiO/Ce_{1-x}Ni_xO_2$: synthesis and synergistic effect of simultaneous surface modification and internal doping for superior catalytic performance. *RSC Advances*, *4*(13), pp.6397-6406.

[7] Liu, W., Wang, W., Tang, K., Guo, J., Ren, Y., Wang, S., Feng, L. and Yang, Y., 2016. The promoting influence of nickel species in the controllable synthesis and catalytic properties of nickel-ceria catalysts. *Catalysis Science & Technology*. *6*, pp. 2427-2434.

[8] Sun, S., Zhao, X., Lu, H., Zhang, Z., Wei, J. and Yang, Y., 2013. Unusual properties of nanostructured $Ce_{1-x}Co_xO_{2-y}$, $Ce_{1-x}Ni_xO_{2-y}$ and $Ce_{1-(x+\ y)}Co_xNi_yO_{2-z}$: structural studies and catalytic activity. *CrystEngComm*, *15*(7), pp.1370-1376.

[9] Shaaban, E.R., Kaid, M.A. and Ali, M.G.S., 2014. X-ray analysis and optical properties of nickel oxide thin films. *Journal of Alloys and Compounds*, *613*, pp.324-329.

[10] Korošec, R.C. and Bukovec, P., 2006. Sol-gel prepared NiO thin films for electrochromic applications. *Acta Chim. Slov*, *53*, pp.136-147.

[11] Solsona, B., Concepción, P., Hernández, S., Demicol, B. and Nieto, J.M.L., 2012. Oxidative dehydrogenation of ethane over NiO-CeO_2 mixed oxides catalysts. *Catalysis today*, *180*(1), pp.51-58.

[12] Ovejero, G., Rodríguez, A., Vallet, A. and García, J., 2012. Ni supported on Mg-Al oxides for continuous catalytic wet air oxidation of Crystal Violet. *Applied Catalysis B: Environmental*, *125*, pp.166-171.

[13] Ovejero, G., Rodríguez, A., Vallet, A. and García, J., 2013. Catalytic wet air oxidation of a non-azo dye with Ni/MgAlO catalyst. *Chemical engineering journal*, *215*, pp.168-173.

Chapter 7

Zn-Ce Nanocatalysts: Characterization and application in CWAO

ZnO is a widely studied photocatalyst [1-3], but there are relatively few reports on the oxidation application of ZnO. The acid treated ZnO catalyst was found to remove 68% Rhodamine B in wet oxidation [4]. ZnO exhibited the promotional effect in water oxidation catalyzed by Co_3O_4 [5]. CeO_2-ZnO composite hollow microspheres attained 100% oxidation of CO [6].

On the basis of these oxidation applications of ZnO based materials, ZnO was selected for the formation of mixed oxide with CeO_2. The ZnO-CeO_2 nano-catalysts (0, 20, 40, 50, 60, 80, 100 at% Zn) were prepared by the co-precipitation method (discussed in **Chapter 2**) and characterized by various techniques. This chapter deals with the discussion on the characteristics of nanosized ZnO-CeO_2 oxides and their application in CWAO of wastewater.

7.1. Characterization of ZnO-CeO_2 mixed oxides

7.1.1. XRD analysis

Figure 7.1(a) shows the XRD pattern of CeO_2-ZnO mixed oxides. The diffraction pattern for CeO_2 was consistent with JCPDS file 81-0792, as discussed in Chapter 3. ZnO exhibited the tetragonal reflections at 31.8, 34.5, 36.3, 47.6, 56.7, 63, 66.5, 68.1, 69.2, 72.8 and 77.2 corresponding to (100), (002), (101), (102), (110), (103), (200), (112), (201), (004) and (202) respectively (JCPDS 79-0205). No diffraction peaks corresponding to zinc oxide were observed up to zinc content of 20 at%, indicating the incorporation of ZnO within the ceria lattice, which was further evidenced by shifting of characteristic ceria peaks towards higher angle (27^o to 30^o; **Figure 7.1(b)**). Further augmentation in Zn content exhibited peaks for ZnO phase, suggesting the formation of solid solution. In mixed catalysts, the peaks were broad and less intense, indicating the decreased crystallite size [7]. The average crystallite size and lattice parameter

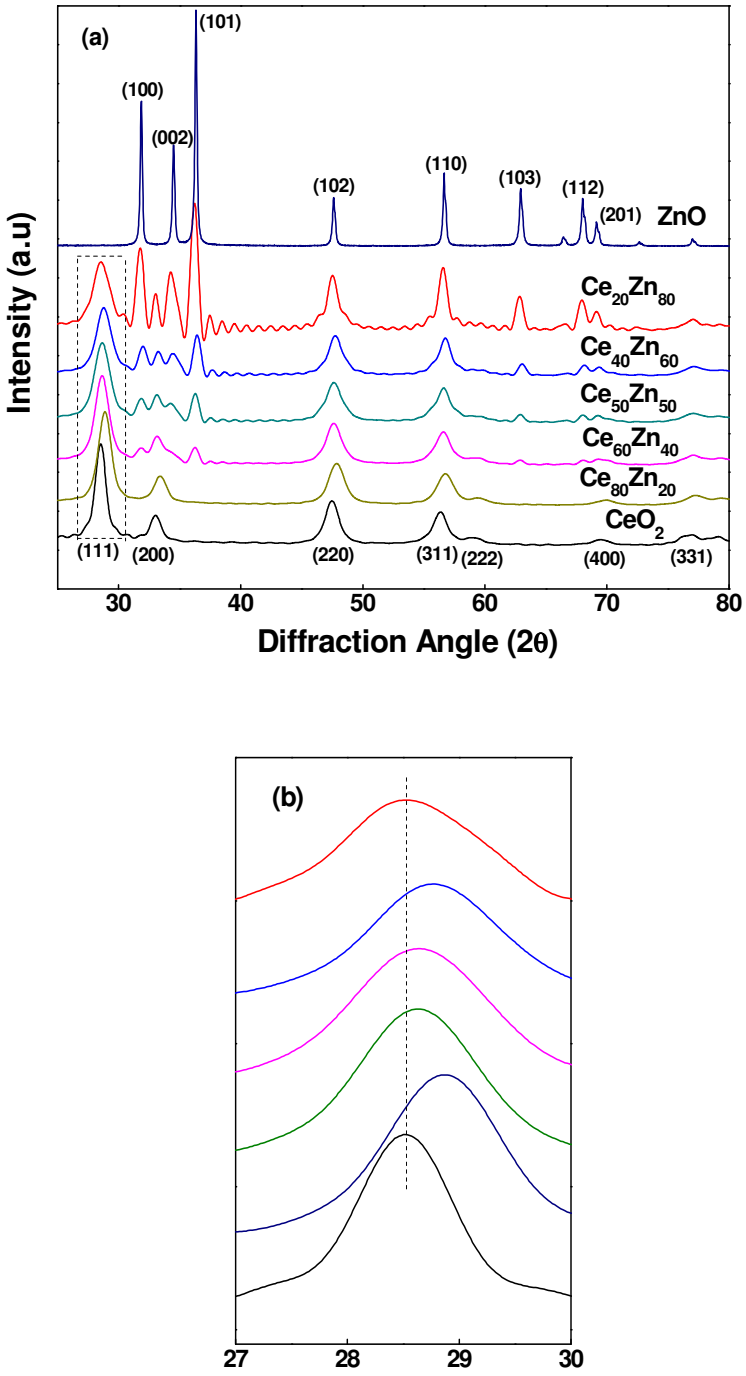

Fig.7.1. (a) XRD pattern of samples (b) low angle region from 27 to 30°

are listed in **Table 7.1**. Average crystallite size of CeO_2 was significantly decreased with increasing Zn content. The lattice parameter of CeO_2 was 5.417Å, which decreased by 0.06 (5.357

Å) for $Ce_{80}Zn_{20}$ catalyst. This decrease was in accordance with the previous theoretical study by Vanpoucke et al. [8], where a decrease of 0.07 Å was obtained for $Ce_{0.75}Zn_{0.25}O_2$ using DFT calculations. The overall trend of decrease in lattice parameter was in good correlation with the experimental study by Ramasamy et al. [9].

7.1.2. FT-IR analysis

The FT-IR spectra of CeO_2, $Ce_{40}Zn_{60}$ and ZnO catalysts are presented in **Figure 7.2**. For CeO_2, a characteristic band was observed at 560 cm^{-1}. ZnO showed strong absorption band at 438 cm^{-1} assigned to Zn-O stretching vibration [10]. For $Ce_{40}Zn_{60}$ catalyst, broadened band with decreased intensity confirmed the interaction between CeO_2 and ZnO phases in mixed oxide.

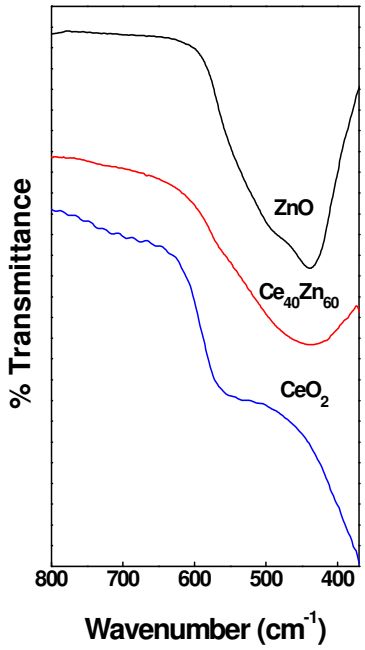

Fig.7.2. FT-IR of catalysts

7.1.3. Raman analysis

The Raman spectrum of CeO_2, $Ce_{80}Zn_{20}$ and ZnO nanocatalysts are presented in **Figure 7.3**. CeO_2 showed the characteristic peak at 462 cm^{-1}. For $Ce_{80}Zn_{20}$ mixed oxide, a characteristic band of oxygen vacancies at 600 cm^{-1} was also observed. The I_{600}/I_{462} ratio was found to be 0.07. ZnO exhibited the bands at 330 cm^{-1} (E_2 high- E_2 low), 437 cm^{-1} (E_2 high), and 658 cm^{-1} (E_2 low + B_1 high). Small peaks at 380 cm^{-1} and 583 cm^{-1} were the characteristic of high density of common

oxygen defects in ZnO [11]. Raman study concluded that the interaction of ZnO with CeO_2 introduces the oxygen vacancies.

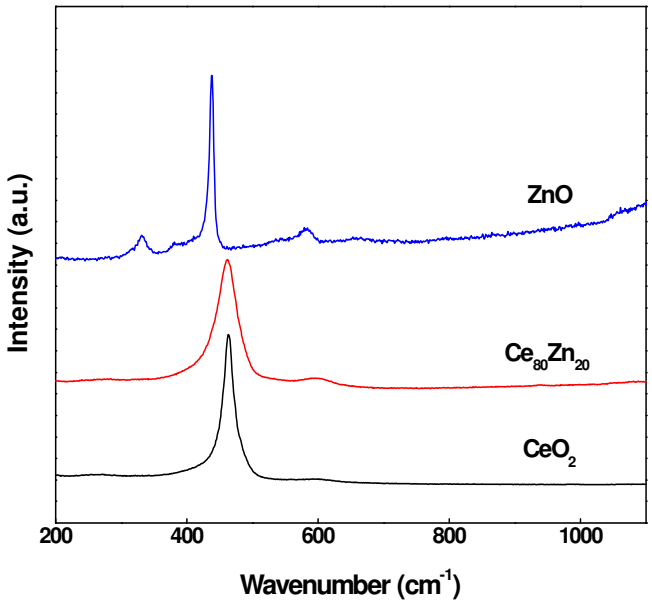

Fig.7.3. Raman spectra of catalysts

7.1.4. XPS analysis

Figure 7.4 depicts the XPS spectra of $Ce_{40}Zn_{60}$ catalyst. Ce 3d spectra exhibited six main components characteristic of Ce^{4+} at the binding energies of 880.6 eV, 887.3 eV, 896.5 eV, 899 eV, 906.7 eV and 915.7 eV corresponding to v, v″, v‴, u, u″ and u‴ respectively. Peaks for v^o (879.6 eV), v′ (884.4 eV), u^o (897 eV) and u′ (900.7 eV) components evidenced the presence of Ce^{3+}. Atomic fraction of Ce^{3+} was found to be 26%. Zn $2p_{3/2}$ spectra presented a peak at 1020.9, corresponding to the presence of Zn^{2+} in ZnO lattice [12,13]. O 1s spectra exhibited three peaks. The relative percentage of peak corresponding to structural/lattice oxygen (528.8 eV), adsorbed surface oxygen as OH ions (531.6 eV) and supercharged oxygen (O_2^-) near oxygen vacant sites (530.5 eV) was 63.9%, 12.7% and 23.3%, respectively.

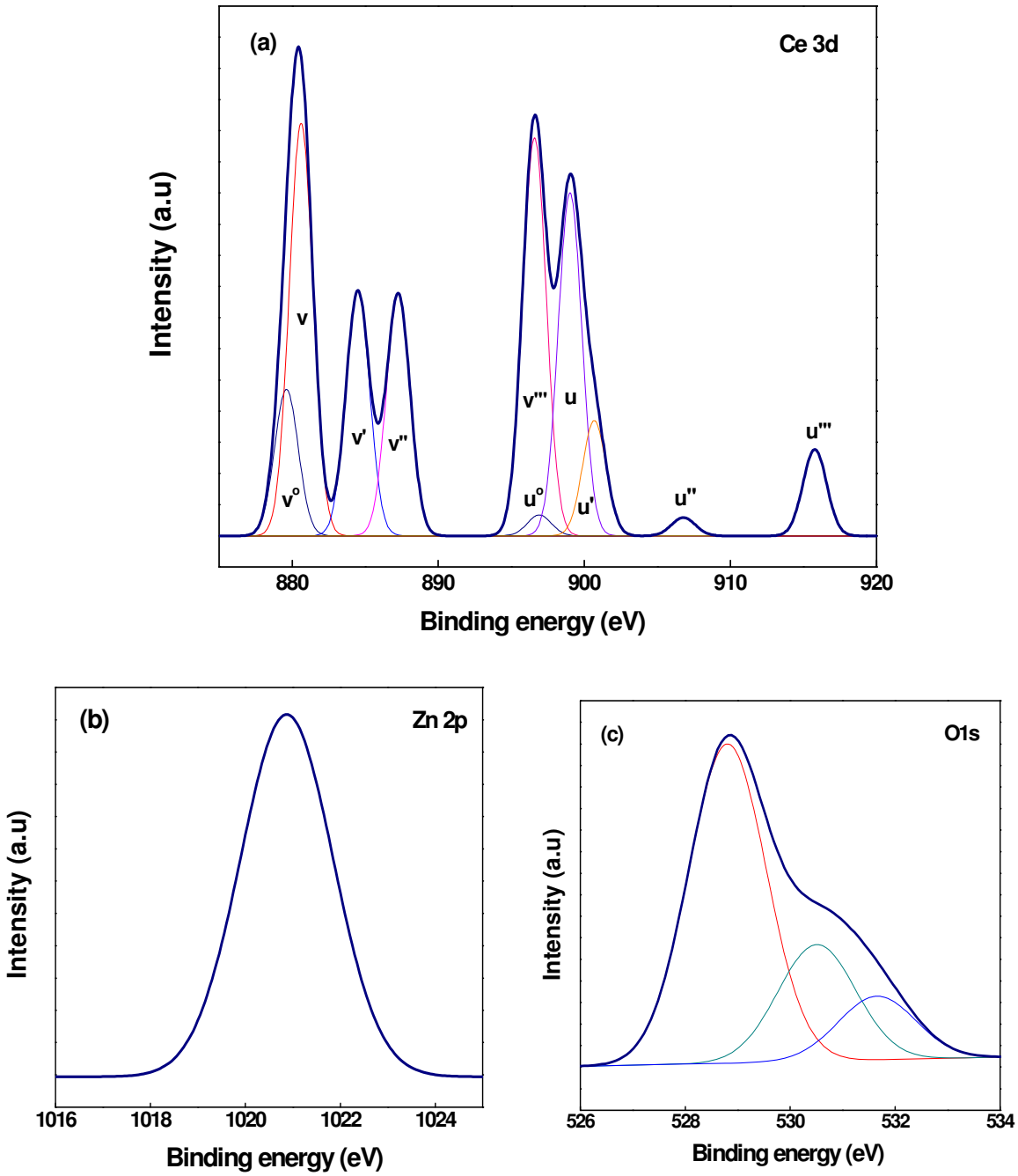

Fig.7.4. XPS spectra of $Ce_{40}Zn_{60}$ catalyst (a) Ce3d (b) Zn 2p (c) O 1s

Table 7.1. Structural and textural properties of ZnO-CeO_2 catalysts

Sample	Crystallite size (nm) [a]		Lattice parameter [a]	Average particle size (nm) [b]	Specific surface area (m^2/g) [c]	Total pore volume (m^3/g) [c]
	CeO_2	ZnO	CeO_2			
CeO_2	10.6	--	5.417	45 ± 1.4	20	0.089
$Ce_{80}Zn_{20}$	6.8	--	5.357	41± 1.7	54	0.204
$Ce_{60}Zn_{40}$	6.2	10.5	5.382	30 ± 5.4	65	0.105
$Ce_{50}Zn_{50}$	6.1	10.7	5.387	18 ± 2.3	90	0.110
$Ce_{40}Zn_{60}$	5.6	9.9	5.373	16 ± 2.1	104	0.247
$Ce_{20}Zn_{80}$	5.3	10.4	5.393	18 ± 0.9	106	0.202
ZnO	--	11.1	--	40 ± 1.9	35	0.164

[a] XRD, [b] FE-SEM micrographs, [c] N_2-sorption

7.1.5. N_2-adsorption/desorption analysis

Figure 7.5(a) presents the adsorption-desorption curve for CeO_2, $Ce_{40}Zn_{60}$ and ZnO catalysts. Adsorption isotherm of all samples showed an inflection at relative high pressure, indicating the presence of secondary pores. A narrow hysteresis due to desorption was the characteristic of irregular pore structure. PSD **(Figure 7.5(b))** confirmed the presence of disordered pores with wide pore size of 3-12 nm for CeO_2 and 3-7 nm for $Ce_{40}Zn_{60}$ and ZnO catalyst. The textural properties (BET surface areas and pore volume) of all samples are summarized in **Table 1**. From the table, it was observed that the mixed catalysts possessed high BET surface area (54-106 m^2/g) and pore volume (0.105-0.247 cc g^{-1}). Surface area was higher than the previous reports by Lin et al. [14] (63 $m^2\ g^{-1}$) and Anandan et al. [15] (80 $m^2\ g^{-1}$), where the catalysts were prepared by co-precipitation and hydrothermal methods, respectively.

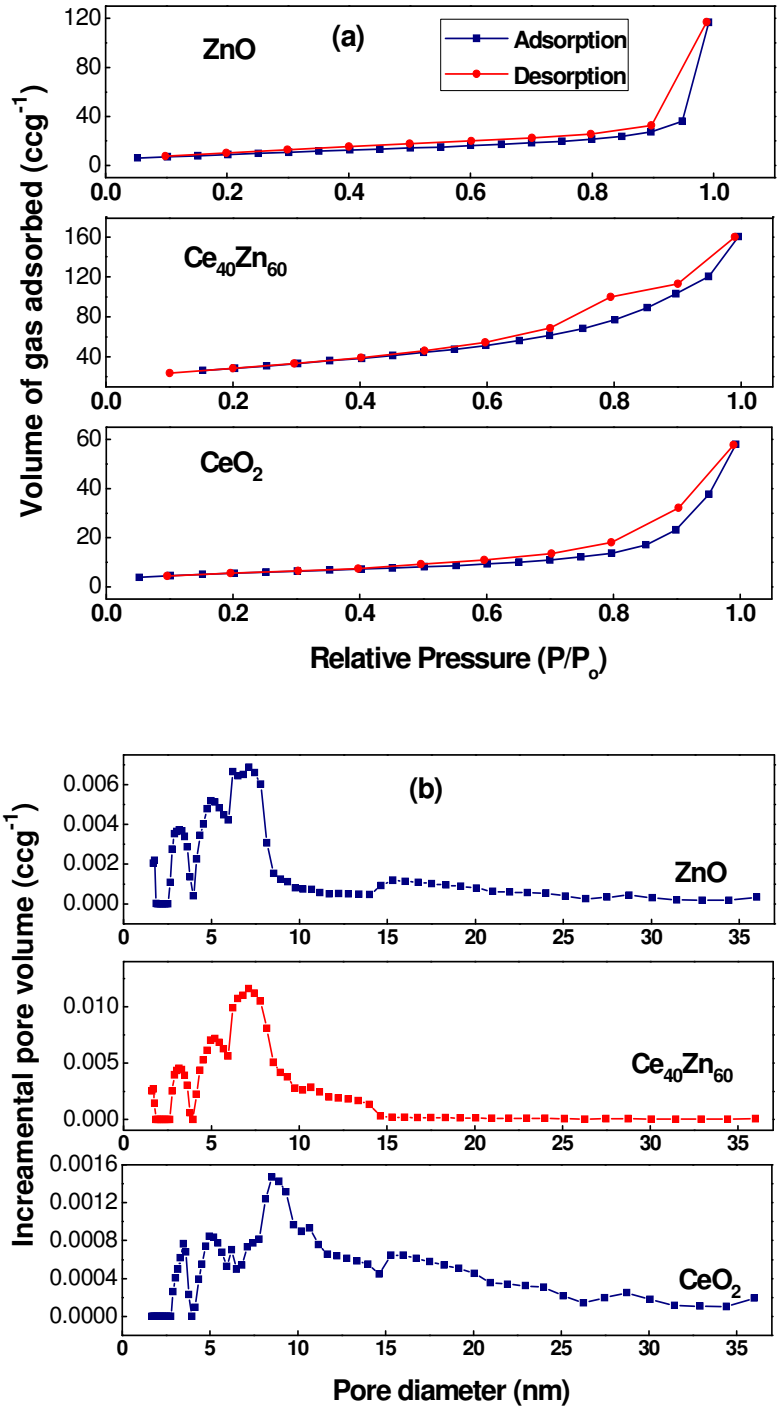

Fig.7.5. (a) N_2-adsorption-desorption isotherms (b) Pore size distribution

7.1.6. FE-SEM and TEM analysis

Figure 7.6 shows the detailed view of FE-SEM micrographs of all samples and correspondingly their particle size ranges are mentioned in **Table 7.1**. The average particle size of CeO_2 was 45 nm which decreased to 41 nm for sample with 20 at% Zn. Further increase in Zn content resulted in considerable decrease in average particle size. EDX spectra of mixed oxides are presented in **Figure 7.7**, and the expected as well as obtained values of Ce/Zn mole ratio are provided in **Table 7.2**. EDX analysis confirmed that the obtained mole ratio values were close to the expected values, confirming the presence of Ce and Zn with required mole ratio. The TEM micrographs of CeO_2, $Ce_{40}Zn_{60}$ and ZnO catalysts along with their SAED patterns are presented in **Figure 7.8**. TEM micrographs confirmed the presence of disordered pores. The mean diameter of CeO_2, $Ce_{40}Zn_{60}$ and ZnO particles was 16, 9 and 14 nm, respectively. SAED pattern of $Ce_{40}Zn_{60}$ confirmed its polycrystalline nature as the diffraction rings were attributable to (111), (220), (311) planes of cubic CeO_2 and (100), (002), (102), (110) planes of ZnO.

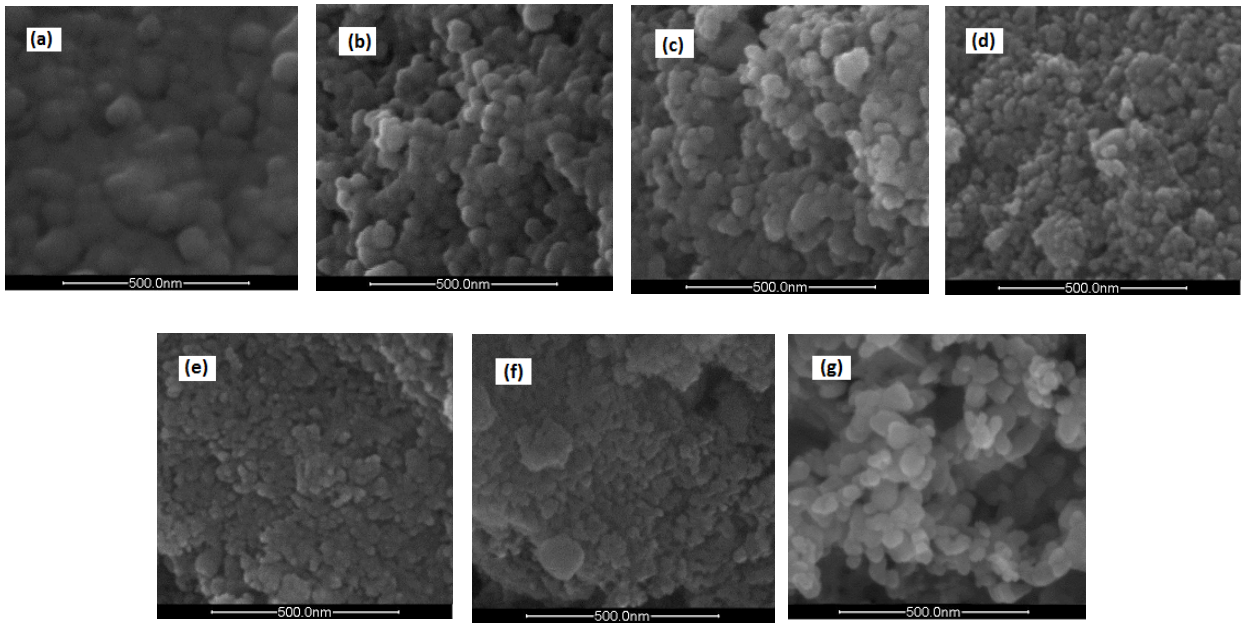

Fig.7.6. FE-SEM micrographs of (a) CeO_2 (b) $Ce_{80}Zn_{20}$ (c) $Ce_{60}Zn_{40}$ (d) $Ce_{50}Zn_{50}$ (e) $Ce_{40}Zn_{60}$ (f) $Ce_{20}Zn_{80}$ (g) ZnO

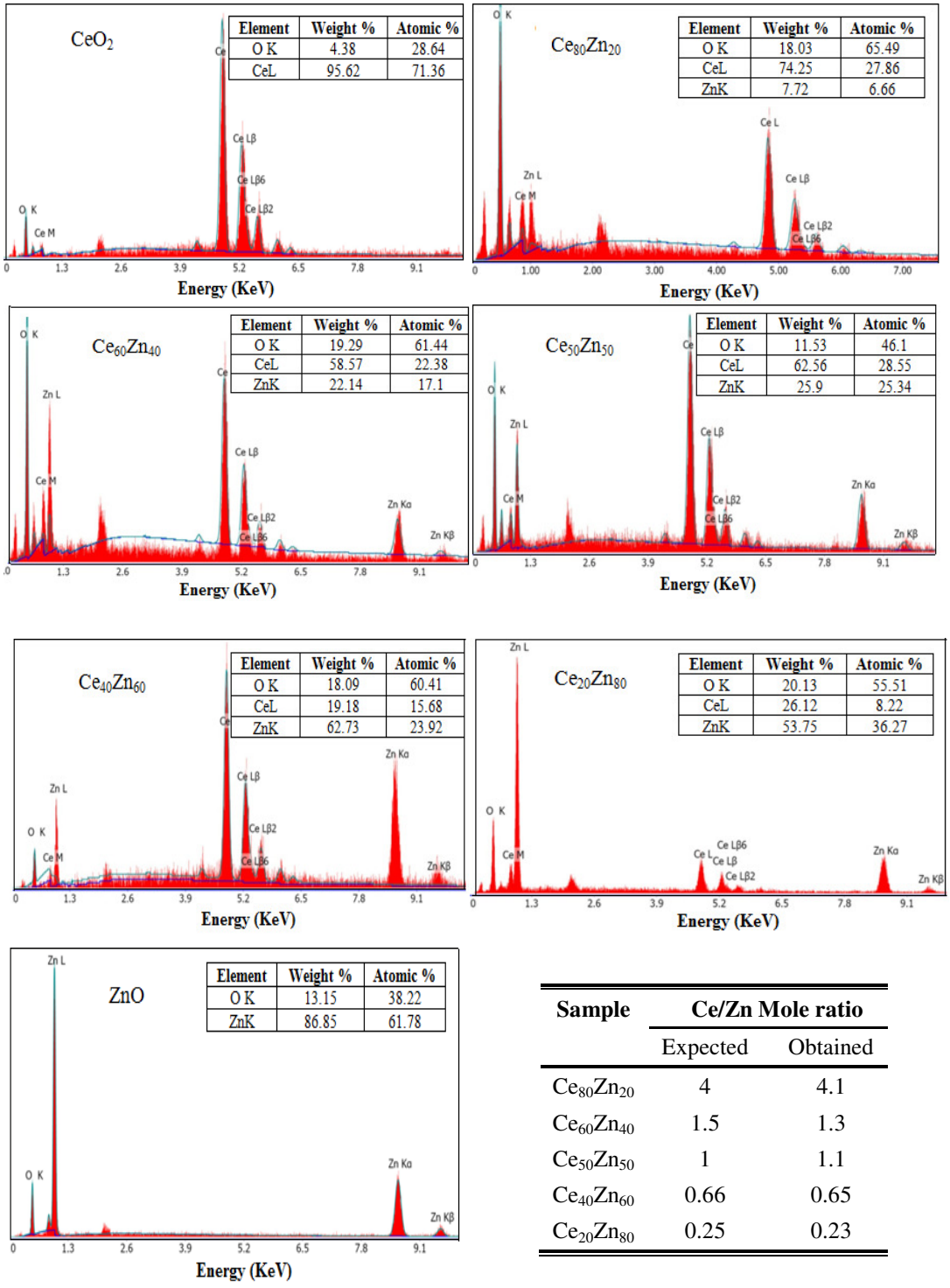

Fig.7.7. EDX spectra of catalysts

Sample	Ce/Zn Mole ratio	
	Expected	Obtained
$Ce_{80}Zn_{20}$	4	4.1
$Ce_{60}Zn_{40}$	1.5	1.3
$Ce_{50}Zn_{50}$	1	1.1
$Ce_{40}Zn_{60}$	0.66	0.65
$Ce_{20}Zn_{80}$	0.25	0.23

Table 7.2. Ce/Zn mole ratio from EDX

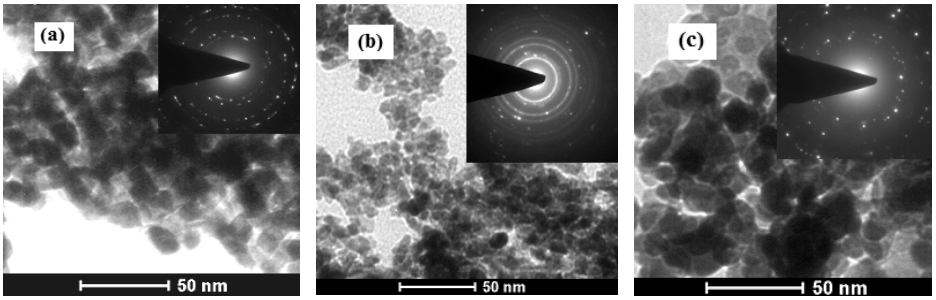

Fig.7.8. TEM micrographs of (a) CeO_2 (b) $Ce_{40}Zn_{60}$ (c) ZnO

7.2. CWAO study over ZnO-CeO_2 nanocatalysts

The physicochemical parameters of paper industry wastewater are presented in **Table 7.3**. The efficiency of ZnO-CeO_2 nanocatalysts in terms of percent abatement of COD, color, AOX and TOC is presented in **Figure 7.9**. As the figure depicts, ZnO exhibited the low abatement profile with 26% COD, 44% color, 32% AOX and 27% TOC abatement. CeO_2 was also found to be less active with 28% COD, 48% color, 21% AOX and 23% TOC abatement. Introduction of Zn ions was found to improve the catalytic efficiency with highest being achieved for $Ce_{40}Zn_{60}$ catalyst (i.e., 64% COD, 72% color, 55% AOX and 63% TOC). The initial BI of wastewater was 0.264, which enhanced up to 0.423 after CWAO.

Table 7.3. Average value of environmental parameters of wastewater

Parameter	Value
Color (mg Pt-Co L^{-1})	3004 ± 76.85
COD (mg L^{-1})	914 ± 29.38
TOC (mg L^{-1})	188.3 ± 3.97
AOX(mg L^{-1})	17.4 ± 0.57
CHPs(µg L^{-1})	472 ± 5.64
BOD_5 (mg L^{-1})	242 ± 9.47
BOD_5/COD	0.264

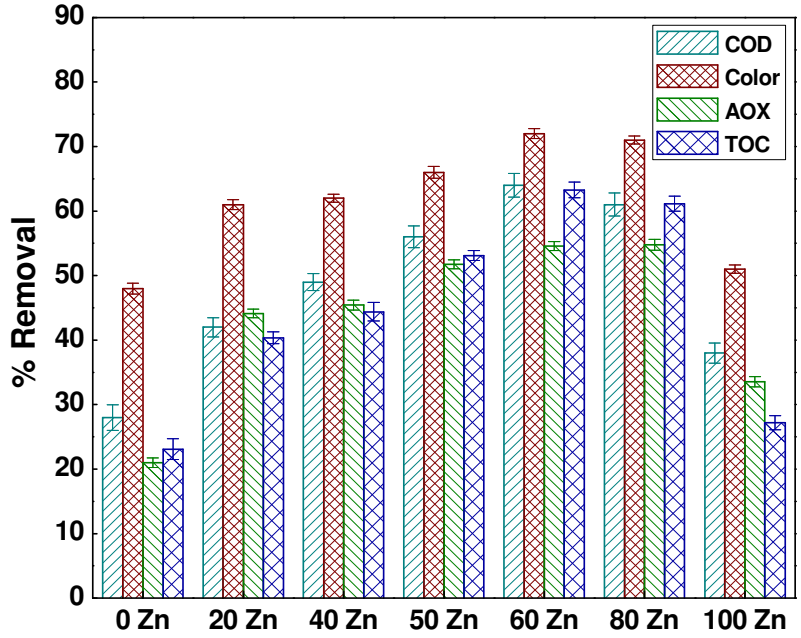

Fig.7.9. Effect of mole ratio of catalyst on COD, color, AOX and TOC removal

Chlorophenolics removal

Figure 7.10 presents the GC chromatogram of CHPs in paper industry wastewater before and after CWAO. GC-MS analysis of wastewater revealed the presence of total 25 CHPs **(Table 7.4)**. According to chemical family CP contributed to the highest share of 80.75%, followed by CG (18.03%), CC (0.77%), CS (0.25%) and CSA (0.21%) **(Figure 7.11(a))**. On the basis of chlorine atom substitution TCHPs presented the highest share of 46.54%, followed by DCHPs (40.21%), MCHPs (13.21%), PCHPs (0.05%) and TeCHPs (0.01%) **(Figure 7.11(b))**. Among all the CHPs, 2,4,5-TCP contributed maximum share of 45.06%.

After CWAO treatment, total of 21 CHPs were detected with overall removal efficiency of 59%. The removal of most of CHPs was from 30-100%. The compounds like PCP, 2,4,6-TCP, 2,3-DCP and 2,6-DCSA were completely removed or their concentration fallen below the detection limit of instrument. 2,4,5-TCP was removed up to 74%, followed by 4,5,6-TCG (58.2%), 2,3,5-TCP (57.6%), 2,5-DCP (56.4%), 2,4-DCP (56.3%) and TCS (54.1%). The rest of compounds were removed up to 15-47%, whereas 4,6-DCG was reduced only by 3%. Treatment data reveals 62.7%, 43.9%, 22.1%, 54.1% and 100% removal of CP, CG, CC, CS and CSA, respectively **(Figure**

7.12(a)). The removal of MCHPs, DCHPs, TCHPs, TeCHPs and PCHPs was up to 33.2%, 38%, 73.3%, 32.3% and 100%, respectively **(Figure 7.12(b))**.

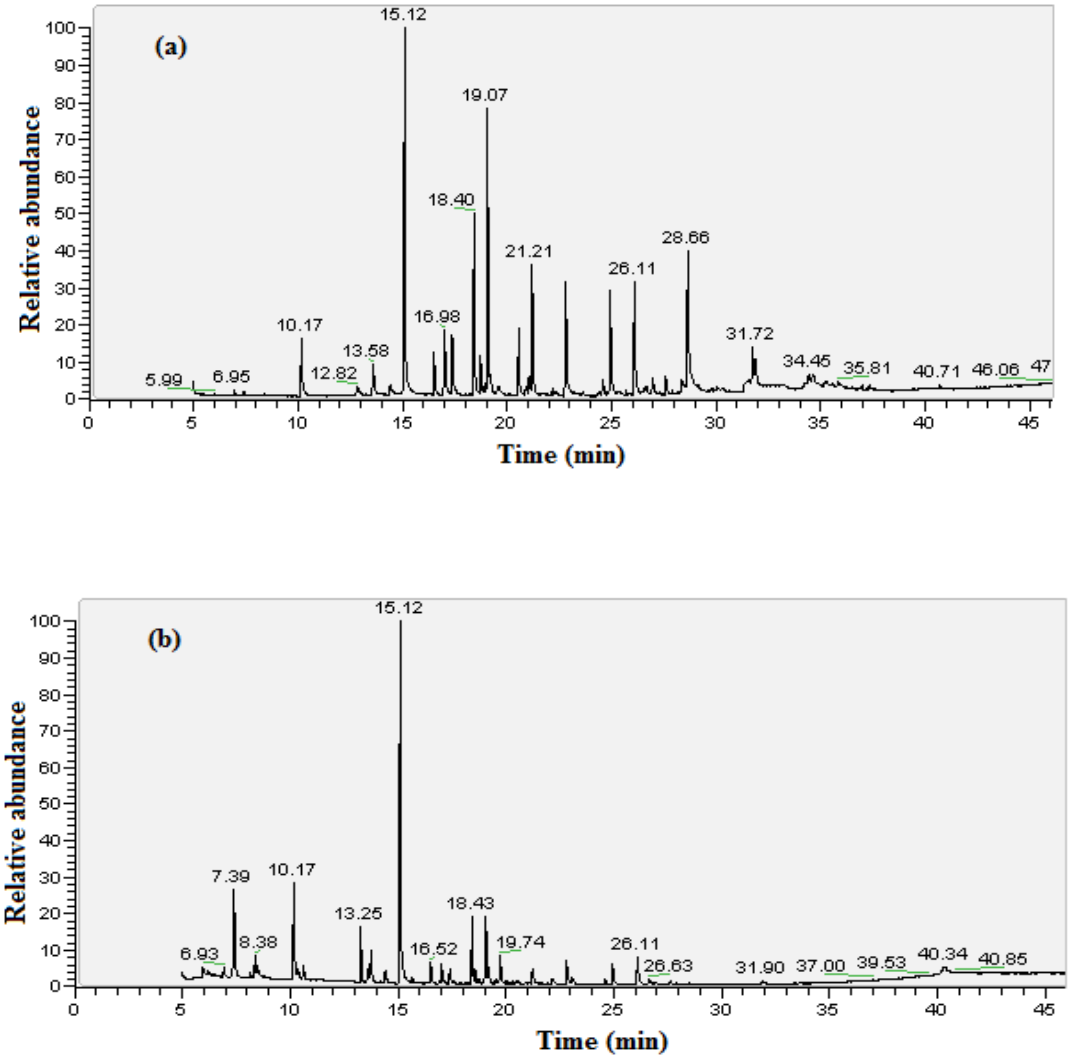

Fig.7.10. GC chromatogram of CHPs (a) before (b) after CWAO

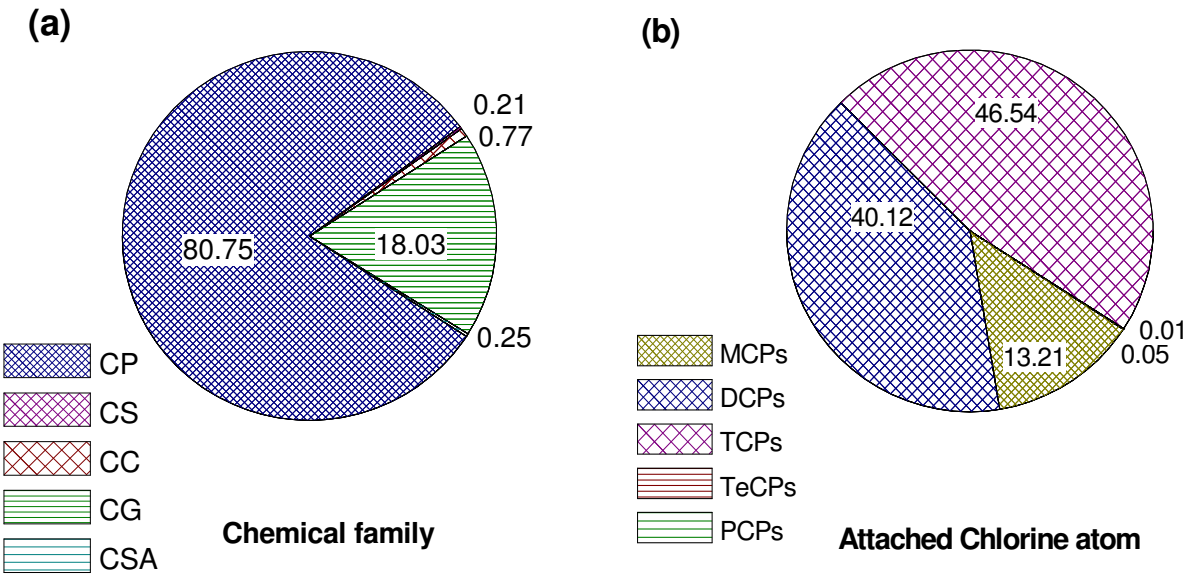

Fig.7.11. Percentage of CHPs

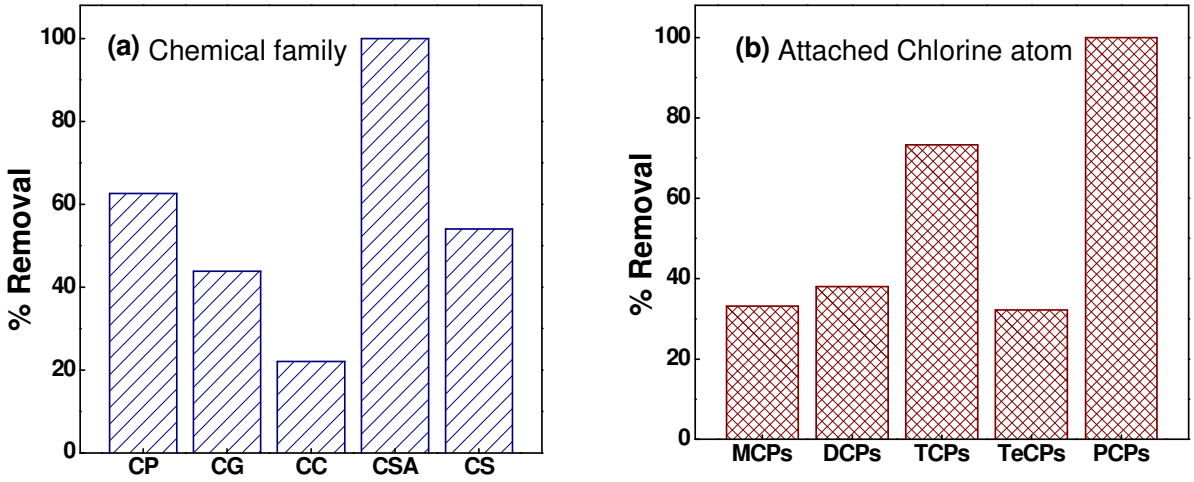

Fig.7.12. Percent removal of CHPs

Table 7.4. Concentration of CHPs with percent removal

S. No	Name of compound	Initial (µg/L)	Final (µg/L)	% Removal
1.	3-CP	14.5 ± 3.85	11.9 ± 2.1	17.2
2.	4-CP	5.9 ± 0.34	5.1 ± 0.09	15.1
3.	2,6-DCP	29.9 ± 1.01	18.3 ± 0.52	39.0
4.	2,5-DCP	78.8 ± 2.25	34.4 ±1.17	56.4
5.	2,4-DCP	33.4 ± 1.54	14.6 ± 1.02	56.3
6.	3,4-DCP	0.3 ± 0.03	0.2± 0.04	29.8
7.	2,3-DCP	0.2 ± 0.08	ND	100
8.	2,4,5-TCP	212.7 ± 17.48	55.3 ± 7.83	73.9
10.	2,3,5-TCP	3.6 ± 0.23	1.5 ± 0.12	57.6
11.	2,4,6-TCP	0.08 ± 0.01	ND	100
12.	2,3,4-TCP	1.4 ± 0.22	0.8 ± 0.07	39.7
13.	PCP	0.2 ± 0.10	ND	100
14.	4-CG	41. 9 ± 3.61	24.6 ± 0.5	41.3
15.	4,5-DCG	41.6± 4.37	22.1 ± 1.04	47.0
16.	4,6-DCG	0.5 ± 0.09	0.5 ± 0.06	3.2
17.	3,4,6-TCG	0.3 ± 0.02	0.8 ± 0.05	35.9
18.	3,4,5-TCG	0.1 ± 0.01	0.06 ± 0.02	31.1
19.	4,5,6-TCG	0.3± 0.05	0.1 ± 0.03	58.2
20.	TeCG	0.4 ± 0.02	0.3 ± 0.04	32.3
22.	3,5-DCC	3.6 ± 0.39	2.8 ± 0.13	22.1
24.	TCS	1.2 ± 0.06	0.5 ± 0.07	54.1
25.	2,6-DCSA	1.0 ± 0.02	ND	100
	Total	471.9	193.3	59

*ND- Not detected

7.3. Recycling and leaching studies

The recycling study over used catalyst indicated that after two recycles, the $Ce_{40}Zn_{60}$ mixed oxide retained satisfactory catalytic activity with 59% COD and 68% color removal **(Figure 7.13)**. The dissolved Ce IV (418.6 nm) concentrations in supernatant ranged from 0.102 to 0.133 ppm and Zn II (213.8 nm) concentration ranged from 0.396 to 0.773 ppm. The metal leaching value was comparably low to the previous reports [16,17], indicating the negligible leaching.

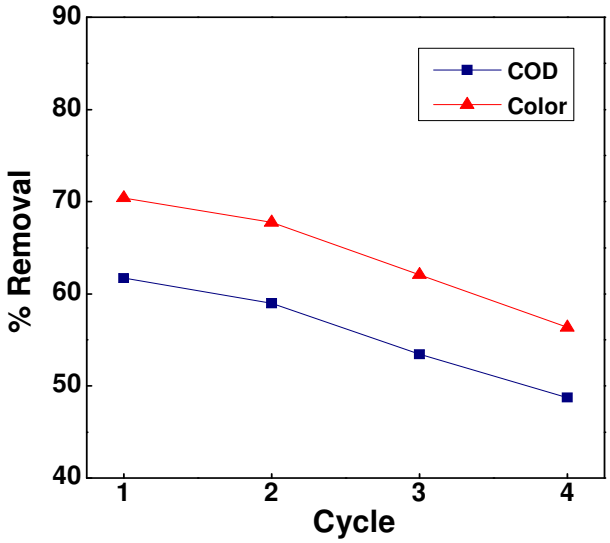

Fig.7.13. Effect of catalyst recycling on COD and color removal

7.4. Kinetic study

The kinetic study on time-dependent COD removal confirmed the first order kinetics as straight line with R^2 values of 0.959 was obtained in the plot constructed between $\ln[COD]_o/[COD]$ and time (t) **(Figure 7.14)**.

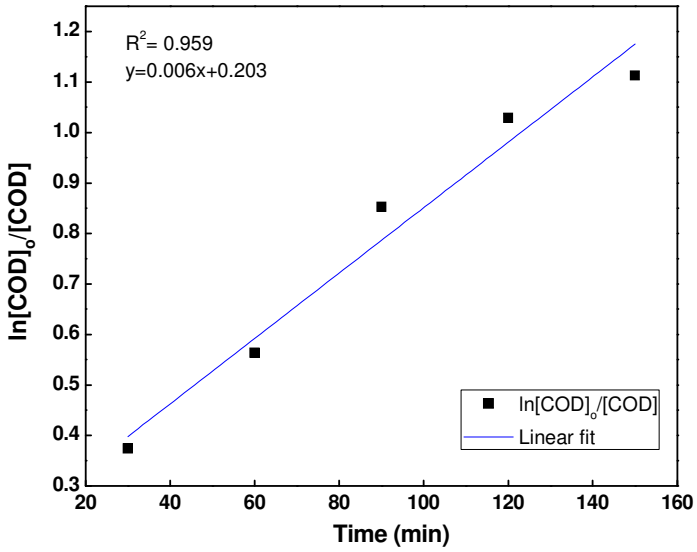

Fig.7.14. Linear fitting of $\ln[\mathrm{COD}]_o/[\mathrm{COD}]$ as a function of reaction time

7.5. Summary

1. The ZnO-CeO_2 mixed oxides exhibited improved structural, textural and catalytic property than the single metal oxides.
2. $Ce_{40}Zn_{60}$ mixed oxide presented the surface area of 104 m^2g^{-1} and pore volume of 0.247 ccg^{-1}. The pore size was found to be 3-7 nm.
3. Raman analysis confirmed the presence of O-vacancies in mixed oxides.
4. XPS analysis indicated the presence of 4+, 3+ oxidation states for Ce and 2+ for Zn metal ions. Ce^{3+} concentration was found to be 26%.
5. $Ce_{40}Zn_{60}$ mixed oxide exhibited maximum COD (64%), color (72%), AOX (55%), TOC (63%) and CHPs (59%) removal.
6. Biodegradability index increased from 0.27 to 0.42.
7. The first order kinetics was ascertained with R^2 values of 0.959.
8. The low leaching values of Ce (0.102-0.133 ppm) and Zn (0.396-0.773 ppm) metals was obtained.

References

[1] Georgekutty, R., Seery, M.K. and Pillai, S.C., 2008. A highly efficient Ag-ZnO photocatalyst: synthesis, properties, and mechanism. *The Journal of Physical Chemistry C*, *112*(35), pp.13563-13570.

[2] Behnajady, M.A., Modirshahla, N. and Hamzavi, R., 2006. Kinetic study on photocatalytic degradation of CI Acid Yellow 23 by ZnO photocatalyst. *Journal of hazardous materials*, *133*(1), pp.226-232.

[3] Ren, S., Wang, B., Zhang, H., Ding, P. and Wang, Q., 2015. Sandwiched ZnO@ Au@Cu_2O Nanorod Films as Efficient Visible-Light-Driven Plasmonic Photocatalysts. *ACS applied materials & interfaces*, *7*(7), pp.4066-4074.

[4] Das, M. and Bhattacharyya, K.G., 2014. Oxidation of Rhodamine B in aqueous medium in ambient conditions with raw and acid-activated MnO_2, NiO, ZnO as catalysts. *Journal of Molecular Catalysis A: Chemical*, *391*, pp.121-129.

[5] Rong, F., Zhao, J., Su, P., Yao, Y., Li, M., Yang, Q. and Li, C., 2015. Zinc-cobalt oxides as efficient water oxidation catalysts: the promotion effect of ZnO. *Journal of Materials Chemistry A*, *3*(7), pp.4010-4017.

[6] Xie, Q., Zhao, Y., Guo, H., Lu, A., Zhang, X., Wang, L., Chen, M.S. and Peng, D.L., 2013. Facile Preparation of Well-Dispersed CeO_2-ZnO Composite Hollow Microspheres with Enhanced Catalytic Activity for CO Oxidation. *ACS applied materials & interfaces*, *6*(1), pp.421-428.

[7] Ramachandran, S., Tiwari, A. and Narayan, J., 2004. $Zn_{0.9}Co_{0.1}O$-based diluted magnetic semiconducting thin films. *Applied Physics Letters*, *84*(25), pp.5255-5257.

[8] Vanpoucke, D.E., Bultinck, P., Cottenier, S., Van Speybroeck, V. and Van Driessche, I., 2014. Aliovalent doping of CeO_2: DFT study of oxidation state and vacancy effects. *Journal of Materials Chemistry A*, *2*(33), pp.13723-13737.

[9] Ramasamy, V. and Vijayalakshmi, G., 2015. Effect of Zn doping on structural, optical and thermal properties of CeO_2 nanoparticles. *Superlattices and Microstructures*, *85*, pp.510-521.

[10] Dai, Z., Liu, K., Tang, Y., Yang, X., Bao, J. and Shen, J., 2008. A novel tetragonal pyramid-shaped porous ZnO nanostructure and its application in the biosensing of horseradish peroxidase. *Journal of Materials Chemistry*, *18*(16), pp.1919-1926.

[11] Pal, M., Bera, S., Sarkar, S. and Jana, S., 2014. Influence of Al doping on microstructural, optical and photocatalytic properties of sol-gel based nanostructured zinc oxide films on glass. *RSC Advances*, *4*(23), pp.11552-11563.

[12] Das, D. and Mondal, P., 2014. Photoluminescence phenomena prevailing in c-axis oriented intrinsic ZnO thin films prepared by RF magnetron sputtering. *RSC Advances*, *4*(67), pp.35735-35743.

[13] Al-Gaashani, R., Radiman, S., Daud, A.R., Tabet, N. and Al-Douri, Y., 2013. XPS and optical studies of different morphologies of ZnO nanostructures prepared by microwave methods. *Ceramics International*, *39*(3), pp.2283-2292.

[14] Lin, F., Delmelle, R., Vinodkumar, T., Reddy, B.M., Wokaun, A. and Alxneit, I., 2015. Correlation between the structural characteristics, oxygen storage capacities and catalytic activities of dual-phase Zn-modified ceria nanocrystals. *Catalysis Science & Technology*, *5*(7), pp.3556-3567.

[15] Anandan, S. and Miyauchi, M., 2011. Ce-doped ZnO ($Ce_xZn_{1-x}O$) becomes an efficient visible-light-sensitive photocatalyst by co-catalyst (Cu^{2+}) grafting. *Physical Chemistry Chemical Physics*, *13*(33), pp.14937-14945.

[16] Xu, Y. and Sun, D., 2012. Structure and catalytic activity of MoZnAlO catalyst for degradation of cationic red GTL under room conditions. *Chemical Engineering Journal*, *183*, pp.332-338.

[17] Xu, A., Yang, M., Qiao, R., Du, H. and Sun, C., 2007. Activity and leaching features of zinc-aluminum ferrites in catalytic wet oxidation of phenol. *Journal of hazardous materials*, *147*(1), pp.449-456.

Chapter 8

Comparison of Results

This chapter presents the comparison of physicochemical properties and removal efficiency of the different catalysts. The relation between activity and properties of catalyst is also discussed.

8.1. Comparison of structural and textural properties of catalysts

8.1.1. Surface area

All mixed oxides exhibited the small crystallite size ranging from 4-6 nm. The Fe-Ce mixed oxides exhibited maximum surface area (SA) of 149 m^2g^{-1}, which was comparable to the Cu-Ce mixed oxide (143 m^2g^{-1}). A slight decrease in SA was observed for Co-Ce (109 m^2g^{-1}) and Zn-Ce (104 m^2g^{-1}) mixed oxides, while for Ni-Ce the SA was significantly lower with the value of 90 m^2g^{-1} (**Table 8.1**).

8.1.2. Pore volume and pore size distribution

Co-Ce mixed oxide exhibited the maximum pore volume of 0.416 ccg^{-1} followed by Cu-Ce mixed oxide (0.386 ccg^{-1}). Fe-Ce, Zn-Ce and Ni-Ce mixed oxides presented the pore volume of 0.283 ccg^{-1}, 0.247 ccg^{-1} and 0.275 ccg^{-1}, respectively. Fe-Ce mixed oxide exhibited the most uniform pores with pore size of 3-5 nm. Co-Ce, Cu-Ce and Zn-Ce mixed oxides were found to have relatively non-uniform and wider pores of around 3-8 nm. Ni-Ce mixed oxide presented the widest pores of 3-11 nm (**Table 8.1**).

8.1.2. Oxygen vacancies

All mixed oxides indicated the under stoichiometry of ceria due to the presence of Ce^{3+}. The atomic fraction of Ce^{3+} was found to be 28% for both Fe-Ce and Co-Ce mixed oxides. Ce^{3+} percentage was 27% and 26% for Cu-Ce and Zn-Ce mixed oxides, respectively. Highest oxygen vacancies were found for the Zn-Ce mixed oxide (23.3%). Fe-Ce mixed oxide showed 21% oxygen vacancies. Co-Ce and Cu-Ce mixed oxides presented 19.3% and17.2% oxygen vacancies, respectively (**Table 8.1**).

Table 8.1. Structural and textural properties of mixed oxides

Property	Nanocatalysts				
	Fe-Ce	**Co-Ce**	**Cu-Ce**	**Zn-Ce**	**Ni-Ce**
Crystallite size (nm)	5.5	4.7	4	5.6	4.1
Surface area (m^2g^{-1})	149	109	143	104	90
Pore volume (ccg^{-1})	0.283	0.416	0.386	0.247	0.275
Pore size (nm)	3-5	3-8	3-7	3-7	3-11
Ce^{3+} percentage (%)	28	28	27	26	--
Supercharged oxygen (%)	21	19.3	17.2	23.3	--
Total oxygen defect (%)	30.4	29	25.7	36	--

8.2. Comparison of treatment efficiency of catalysts

The efficiency of catalysts in CWAO of wastewater was studied in terms of COD, Color, TOC, AOX and CHPs removal. Out of all the studied catalysts, Fe-Ce mixed oxide presented the maximum efficiency with 74% COD, 82% color, 72% TOC, 68% AOX and 71% CHPs reduction. The efficiency towards Color, TOC and AOX removal were comparable for Co-Ce and Cu-Ce mixed oxides, but efficiency of Cu-Ce mixed oxide towards CHPs removal was higher (66%) than the Co-Ce mixed oxide (62%). For Zn-Ce and Ni-Ce mixed oxides, comparable removal of COD, color and AOX was observed, while TOC and CHPs removal was higher for Zn-Ce mixed oxide. Thus the removal efficiency of mixed oxides was observed in the order of Fe-Ce > Co-Ce ≈ Cu-Ce > Zn-Ce > Ni-Ce (**Table 8.2**).

Table 8.2. Removal efficiency of Nanocatalysts

Parameter	Percent removal over Nanocatalysts (%)				
	Fe-Ce	**Co-Ce**	**Cu-Ce**	**Zn-Ce**	**Ni-Ce**
COD	74	68	67	64	62
Color	82	79	81	72	75
TOC	72	66	64	63	59
AOX	68	59	61	55	55
CHPs	71	62	66	59	54
BOD/COD	0.47	0.45	0.45	0.42	0.42
Regression factor (R^2)	0.99	0.952	0.972	0.959	0.957
Leaching of metals (ppm)	Ce: 0.12-0.132 Fe: 0.339-0.512	Ce: 0.121-0.126 Co: 0.346-0.595	Ce: 0.104-0.133 Cu: 0.346-0.636	Ce: 0.102 -0.133 Zn: 0.396-0.773	Ce: 0.12-0.16 Ni: 0.218-0.64

8.3. Relation between activity and properties of catalyst

Highest removal efficiency of Fe-Ce mixed oxide can be attributed to its high surface area, uniform pores and high Ce^{3+} content. Oxygen vacancies play a crucial role during the oxidation process as they activate the oxygen species on catalyst surface. Thus high removal efficiency was expected from Zn-Ce mixed oxide as it presented more oxygen vacancies (23.3%) in comparison to Fe-Ce mixed oxide (21%). Low removal efficiency of Zn-Ce mixed oxide can be attributed to its low surface area, pore volume and wider pores in comparison to the Fe-Ce mixed oxide. Additionally, the presence of two oxidation states for Fe_2O_3 (3+,2+) may contribute more towards the redox reaction, in comparison to the ZnO with single oxidation state (2+). In case of other mixed oxides, the efficiency was in good agreement with their structural and textural properties. Thus, the efficiency of mixed oxides towards CWAO of wastewater is a cumulative outcome of all the physicochemical properties.

Chapter 9

Conclusion and Recommendation

9.1. Conclusion

Based on the present study, the following conclusions can be drawn:

1. Nanosized ceria based mixed oxides are efficient in CWAO of wastewater at mild conditions.
2. Appreciable removal of COD, color, TOC, AOX and CHPs, along with increased biodegradability is achieved.
3. The surface area, uniform pore size distribution and percent Ce^{3+} content, are of most significance for the catalytic property of ceria based mixed oxide systems.
4. The metal leaching is negligible and the process follows first order rate kinetics.

9.2. Recommendation and future work

1. The ordered porous materials can be tried. One can study the SBA-15, MCM-41, KIT-6 based materials.
2. Different morphologies of nanomaterials, like, nanorods, nanowire, nanoplate, nanoflower etc. can also be studied.
3. More extensive efforts are required for operation of CWAO at ambient temperature. The activated catalysts can be investigated for this purpose.
4. Operation at acidic *pH* is still a challenging issue. More efforts are required towards the investigation of catalyst able to work in the neutral pH range.